DELFT UNIVERSITY OF TECHNOLOGY
FACULTY OF AEROSPACE ENGINEERING

MASTER OF SCIENCE THESIS

Application of Lagrangian Coherent Structures to the computation and understanding of ballistic capture trajectories

A.S. Parkash

September 20, 2019

Application of Lagrangian Coherent Structures to the computation and understanding of ballistic capture trajectories

by

A.S. Parkash

For obtaining the degree of Master of Science in Aerospace Engineering
at Delft University of Technology.

To be defended publicly on September 20, 2019.

Student number:	4278356
Thesis supervisor:	Dr. F. Topputo
Thesis committee:	Dr. Ir. E.J.O. Schrama
	Ir. K.J. Cowan MBA
	Dr. Ir. W.T. van Horssen

An electronic version of this thesis is available at `http://repository.tudelft.nl/`.

Abstract

Ballistic capture is a transfer method which was first applied in 1990. It allows a spacecraft to approach a target celestial body and enter a (temporary) orbit around it without requiring manoeuvres in between. Ballistic capture is a promising concept, as it is expected to be safer, cheaper, and more flexible in terms of launch windows than a traditional Hohmann transfer. Currently, a computationally efficient method which simulateneously allows for an inisghtful description of the dynamics of the ballistic capture problem remains to be found. A potential solution lies within the field of Lagrangian Coherent Structures (LCS). LCS is defined as a separatrix of regions in a flow with distinct dynamics. It may be possible that LCS around a planet have some correspondence to results found using stable set manipulation, a classic technique for obtaining capture trajectories.

In this research three new areas within the field relating LCS to ballistic capture are explored. Firstly, it has not yet been shown what LCS can be found in an area around a planet, without making use of a priori stable set information. Furthermore, it is unclear what the effect is of changing the integration time in the procedure of extracting LCS. Finally, there has not yet been an analysis to show how the LCS relate to stable sets with different number of revolutions n.

In this work two algorithms for extracting LCS have been developed. One is based on the simple but efficient computation of the Finite Time Lyapunov Exponent (FTLE). Another is based on the more involved Variational Theory. Both algorithms are validated on a toy problem used frequently in LCS extraction studies, and are then applied to the Elliptic Restricted Three Body Problem (ERTBP).

It is shown that LCS around a planet yield resemblance with stable set results. The FTLE-based algorithm is able to quickly and efficiently identify the shape of the stable set. The Weak Stability Boundary, however, can not be extracted distinctly. The Variational Theory-based algorithm yields more distinguishable results for the Weak Stability Boundary. It is shown that large and constant integration times are beneficial. It is shown that extracted LCS form an approximation of the average resulting WSB for all stable sets.

Foreword

This work represents my Master of Science thesis at the faculty of Aerospace Engineering at Delft University of Technology. It is an attempt to explore potential synergies between the fields of ballistic capture and Lagrangian Coherent Structures.

I would like to express my gratitude to my supervisor, dr. Francesco Topputo, for introducing me to the topic of ballistic capture, and giving me the opportunity to explore synergies between two exciting fields. I would also like to thank Francesco for allowing me to dive deeper into the field of ballistic capture by means of an internship at Politecnico di Milano. Regardless of his busy schedule, he was always able to make time whether that be via in-person meetings or halfway across the world via Skype.

Special thanks also goes out to Marc Naeije, who introduced me and allowed me to work on the computing cluster of the astrodynamics research group. Without that, the results in this thesis would not have been attainable.

My gratitude also goes out to my friends, for the many great days and evenings that were spent in laughter and endless philosophical discussions. This gratitude extends far beyond the timeframe of this project, as it has made my time since the first day I set foot in Delft a great experience.

Finally and most importantly I am grateful to my parents, Atam and Shalini, for their unconditional love and support.

A.S. Parkash
Delft, September 2019

Contents

List of Figures

List of Tables

Acronyms

LCS	Lagrangian Coherent Structures
WSB	Weak Stability Boundary
RTBP	Restricted Three Body Problem
ERTBP	Planar Elliptic Restricted Three Body Problem
CRTBP	Planar Circular Restricted Three Body Problem
FTLE	Finite Time Lyapunov Exponent
RLCS	Repelling Lagrangian Coherent Structure
ALCS	Attracting Lagrangian Coherent Structure
ODE	Ordinary Differential Equation

Nomenclature

P_n	Primary n
m	Mass
μ	Mass parameter
$\mathbf{x}$	State vector
e_p	Eccentricity of primaries
e	Eccentricity of osculating ellipse
f	True anomaly
r	Distance to P_2
t	Time
C	Jacobi energy
J_c	Jacobi integral
$\mathscr{J}_c(C)$	Steady manifold for level of C
$\mathscr{H}_E(C,f)$	Pulsating Hill's regions
L_k	Equilibrium points
θ	Osculating true anomaly
ΔV	Velocity change
H	Kepler Energy
v	Velocity
$l(\theta)$	Radial segment used in stability definition
$\mathscr{W}$	Stable set
$\partial\mathscr{W}$	Weak Stability Boundary
$\mathscr{C}$	Capture set
$\mathscr{L}$	Level function
$\mathscr{S}$	State space
$\mathscr{T}$	Set of times
$\mathscr{R}$	Rule defining evolution of dynamical system
$\phi_{t_0}^t$	Flow map

Φ	State transition matrix
A	Jacobian
$\mathscr{M}$	Material surface
Γ	Evolving material curve
δ	Difference in position
Δ	Cauchy-Green deformation tensor
$\sigma_{t_0}^{t}$	Finite Time Lyapunov Exponent
λ	Eigenvalue
ξ	Eigenvector
T	Integration time
ρ	Repulsion rate
ν	Repulsion ratio
f_{final}	Final integration time
$\mathscr{F}$	Interpolation factor
γ	Neighbouring strainline
L	Length of strainline
ℓ_f	Maximum failure length
ℓ_{min}	Minimum strainline length
$\mathscr{G}_0$	Grid of initial conditions
$\mathscr{U}_0$	Subset of $\mathscr{G}_0$ satistfying condition (B) of LCS
$\mathscr{L}_0$	Subset of $\mathscr{U}_0$ intersected with straight lines
$\mathscr{H}_i$	Subset of $\mathscr{L}_0$ handled by Eudoxos core i

1 Introduction

1.1 History

Ballistic capture is a transfer method which was first developed in the 1980's by Edward Belbruno [2]. The main advantage of a ballistic capture is the fact that the hyperbolic excess velocity when arriving at the target planet can be reduced greatly when compared to a classical Hohmann transfer. This is achieved by exploiting the natural gravitational forces exerted by bodies in the solar system on the arriving spacecraft.

In 1990 the Japanese launched a space probe to the Moon. It was to be the first lunar probe launched to the Moon by a country other than the United States or the Soviet Union. The mission consisted of two mutually attached spacecraft named *Hiten* and *Hagoromo*, which would be launched into an orbit around the Earth. Hagomoro would then follow a Hohmann transfer trajectory towards the Moon, while Hiten would stay behind in Earth orbit for communication purposes ([2], p19).
During the final part of the transfer to the Moon, contact between the ground station and Hagomoro was lost, and as such it was never known if the spacecraft did in fact get into an orbit around the Moon.
Because of the national pride and publicity involved in the sucess of the mission, the Japanese decided to salvage the mission by sending Hiten to the Moon. The main problem in doing so was that Hiten did not have enough fuel on board to reach the Moon by means of conventional methods.

During these times, Edward Belbruno was working on the theory of ballistic capture and it was determined by Belbruno and Miller, an engineer working at NASA's Jet Propulsion Laboratory, that this theoretical concept could be applied for the first time to allow Hiten to reach the Moon ([2], p19). The combined gravitational effects of the Earth, the Moon, and the Sun would allow Hiten to have to spend very little fuel in order to get captured into an orbit around the Moon. Indeed, it turned out that only 3 kg out of the available 7 kg of fuel would be required to fly the trajectory. A major difference between this ballistic capture trajectory and a more conventional Hohmann tra-

jectory is that the former would take 150 days of travel time instead of the 3 days for a Hohmann transfer ([2], p59). The trajectory was flown and thus the first application of ballistic capture was a fact [3].

1.2 Context

In order to find ballistic capture orbits, two methods can be applied. The method involving *invariant manifolds* makes use of the structure of the phase space around collinear equilibrium points of the circular restricted three-body problem [11, 15]. An elegant advantage of this method is that it gives insight into the dynamics of the capture. The drawbacks of the method are that it is not possible to control for the desired orbital elements, and that the method is only applicable for the circular restricted three body problem [11].
The second method revolves around *stable sets*, which are sets of initial conditions whose orbits satisfy an algorithmic definition of orbital stability [25]. The method relies on sampling the physical space around the target planet and integrating a large number of orbits. This is an attractive method as it does not require intricate knowledge of the dynamics around the target planet. Moreover, the definition of stability used in the method can easily be extended to an n-body vector field, which allows for the inclusion of fourth-body perturbations and planetary eccentricities [11]. A drawback lies in the fact that due to the brute-force nature of this approach, it becomes computationally intensive when compared to the method of invariant manifolds [11].

It is evident that the methods described both have their advantanges and disadvantages, but a computationally efficient method which simultaneously allows for an insightful description of the dynamics of the problem is yet to be found.
A novel method to aid in the finding and understanding of ballistic capture trajectories may be found within the field of fluid mechanics, from which the concept of Lagrangian Coherent Structures (LCS) originates. LCS is defined as being a separatrix of regions in a flow with different dynamics [20]. These differing dynamics may be found around a target planet more quickly rather than having to brute force through the computational grid, thus allowing the mission designer to more efficiently design ballistic capture trajectories. Moreover, describing the space around the target planet through LCS may allow for a more thorough and rich understanding of the dynamics around the target planet and provide new insights in capture behaviour, via the mathematical formulation of LCS.

Preliminary work on relating LCS to ballistic capture has been done in [18]. The matching with existing stable set theory was not one-to-one. Explanations for this "poor" matching may be a) due to repelling LCS being more sensitive to different particle dynamics and b) due to the fact that the

LCS are computed using a fixed integration time, whilst the integration time of each particle in the stable set varies due to the satisfaction of the "1-turn condition".

1.3 Objective

The goal of this research is to extend and improve upon previous work done in the application of LCS to the development and understanding of ballistic capture trajectories. In light of this goal, the following research objective is defined:

'The research objective of this thesis is to increase knowledge in the field of computation and understanding of ballistic capture trajectories through the application of Lagrangian Coherent Structures to the physical space around the target planet.'

Following the research objective, the main research question is defined as follows:

'How can the current body of knowledge regarding ballistic capture trajectory computation and understanding using Lagrangian Coherent Structures be extended?'

The main research question can be subdivided into sub-questions as follows:

- Without using a priori knowledge of the WSB, do LCS in the 2D search space around a planet yield WSB?
- How does the Weak Stability Boundary react to a change in integration time, corresponding to the time needed for a particle according to the stability criterion?
- How do the computed LCS for the system relate to WSB corresponding to stable points defined for different number of revolutions n?
- Can the application of LCS to the computation of Weak Stability Boundaries yield more efficient computation compared to the traditional method of stable set manipulation?

1.4 Structure

The structure of this thesis is as follows: in Chapter 2 a description of the dynamical framework used throughout this work is provided. Chapters 3 and 4 give an overview of the literature on the topics of ballistic capture and Lagrangian Coherent Structures, respectively. In Chapter 5 the methodology for computing Lagrangian Coherent Structures is explained. The algorithms used

for the procedure are presented, and validation results on a toy problem are shown. In Chapter 6 an explanation on how the developed software is applied to the astrodynamics problem is shown. Results are presented, and the proposed research questions are answered. Finally, Chapter 7 presents conclusions and recommendations for future work on the topic.

2 | Dynamical Framework

As will be shown in subsequent chapters, the classical method of developing stable sets involves forward and backward propagation of the motion of a particle from a starting point on a specified grid. In this chapter the dynamical framework under which the integrations are performed will be presented. The same framework is later used in the process of applying the developed software to answer the research questions. The content of this chapter is based largely on the content of Chapter 2 of the earlier performed literature review [16]. Parts that were not deemed necessary to carry out this work are left out of this chapter, but the reader is referred to [16] for further details.

2.1 Planar Restricted Three Body Problem

The schematic used in the planar restricted three body problem (RTBP) is shown in Figure 2.1. In this problem three bodies are considered: the large primary (P1), the smaller primary (P2), and the spacecraft (P3). The two primary bodies of masses $m_1 > m_2 > 0$, respectively, move under the mutual gravity on orbits around their common center of mass. The third body moves under the gravity of the primaries in their plane of motion. Furthermore, the third body is assumed to have zero mass, and as such it does not influence the motion of the primaries [24].

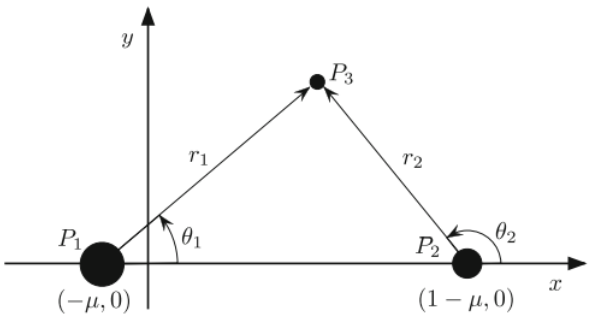

Figure 2.1: Rotating coordinate system used for RTBP [24]

If the mass ratio is defined as $\mu = m_2/(m_1 + m_2)$, the locations of P_1 and P_2 can be set to $(-\mu, 0)$

and $(1-\mu, 0)$ respectively.

Note that the coordinate frame isotropically pulsates as the $P_1 - P_2$ distance varies with the mutual position of the two primaries in their orbits. The motion of P_3 in the normalized co-rotating reference frame may be described by the following set of equations [22]:

$$\ddot{x} - 2\dot{y} = \frac{\partial \omega}{\partial x} \qquad\qquad \ddot{y} + 2\dot{x} = \frac{\partial \omega}{\partial y} \tag{2.1}$$

where ω is given by:

$$\omega(x, y, f) = \frac{\Omega(x, y)}{1 + e_p \cos f} \tag{2.2}$$

with e_p being the eccentricity of the primaries, and f the true anomaly of the system. Furthermore, the potential function is:

$$\Omega(x, y) = \frac{1}{2}(x^2 + y^2) + \frac{1-\mu}{r_1} + \frac{\mu}{r_2} + \frac{1}{2}\mu(1-\mu) \tag{2.3}$$

where parameters r_1 and r_2 represent the distances $P_3 - -P_1$ and $P_3 - -P_2$, respectively, and are given by:

$$r_1^2 = (x+\mu)^2 + y^2 \qquad\qquad r_2^2 = (x+\mu-1)^2 + y^2 \tag{2.4}$$

The dots shown in (2.1) refer to differentiation with respect to the true anomaly f which plays the role of time. If we normalize the period of P_1 and P_2 to 2π, the relation between true anomaly and time is given by:

$$\frac{\mathrm{d}f}{\mathrm{d}t} = \frac{(1 + e_p \cos f)^2}{(1 - e_p^2)^{3/2}} \tag{2.5}$$

In the circular case, we find a specific case of the dynamics provided above. We may set $e_p = 0$ which, from (2.5) yields $\frac{\mathrm{d}f}{\mathrm{d}t} = 0$ and subsequently $\frac{\mathrm{d}}{\mathrm{d}f} = \frac{\mathrm{d}}{\mathrm{d}t}$ and $\omega = \Omega$. The equations of motion are now simply given by:

$$\ddot{x} - 2\dot{y} = \frac{\partial \Omega}{\partial x} \qquad\qquad \ddot{y} + 2\dot{x} = \frac{\partial \Omega}{\partial y} \tag{2.6}$$

For both the circular case ($e_p = 0$) and elliptic case ($e_p \neq 0$) we take a closer look at the energetic considerations. For the circular case, the classic Jacobi integral may be defined:

$$J_C(x, y, \dot{x}, \dot{y}) = 2\Omega(x, y) - (\dot{x}^2 + \dot{y}^2) \tag{2.7}$$

which defines the steady manifold of the states of motion for a specified level of C:

$$\mathscr{J}_C(C) = \left\{(x, y, \dot{x}, \dot{y}) \in \mathscr{R}^2 \,|\, J_C(x, y, \dot{x}, \dot{y}) = C\right\} \tag{2.8}$$

The projection of $\mathscr{J}_C(C)$ onto the configuration space (x, y) is the so-called Hill's region, specified as:

$$\mathscr{H}_C(C) = \left\{(x, y) \in \mathscr{R}^2 \,|\, 2\Omega(x, y) \geq C\right\} \tag{2.9}$$

The motion of the particle P_3 is confined to the Hill region of the corresponding Jacobi energy C. The Hill regions are bounded by the Hill curves (also known as zero-velocity curves) for which the equal sign in (2.9) holds. The allowed regions are the regions for which the inequality in (2.9) holds. The forbidden regions are the complement of the allowed regions. A graphical representation of this phenomenon is shown in Figure 2.2.

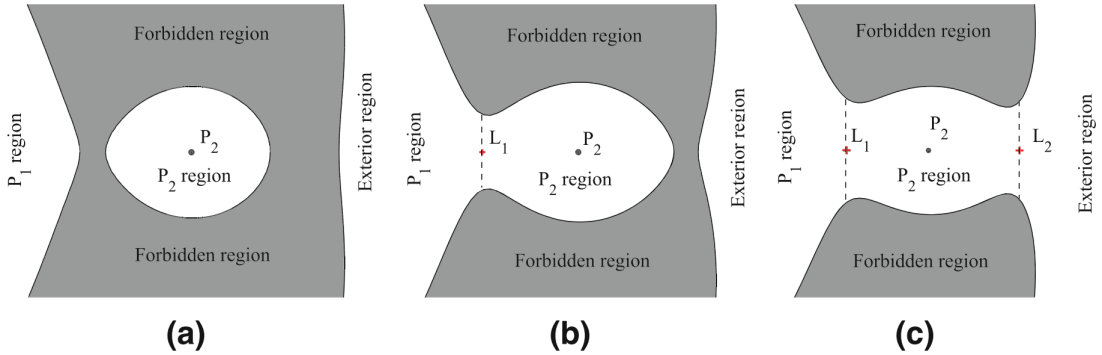

Figure 2.2: P_1, P_2, and exterior regions for three cases of interest. a) $J_c \geq C_1$, b) $C_2 \leq J_C < C_1$ c) $C_3 \leq J_C < C_2$. Forbidden regions are shown in grey [12]

For the elliptic case a similar energy analysis can be performed. An integral of motion can be achieved [22]:

$$J_E(x, y, x', y', f) = 2\omega - (x'^2 + y'^2) - 2e_p \int_{f_0}^{f} \frac{\Omega(x, y)\sin\widetilde{f}}{(1 + e_p\cos\widetilde{f})^2}\mathrm{d}\widetilde{f} \tag{2.10}$$

Similar to the circular case, a manifold can be defined given an energy C:

$$\mathscr{J}_E(C, f) = \left\{(x, y, x', y') \in \mathscr{R}^4 \,|\, J_E(x, y, x', y', f) = C\right\} \tag{2.11}$$

We may again project this onto the configuration space, which gives rise to the so-called pulsating Hill's regions:

$$\mathscr{H}_E(C, f) = \left\{(x, y) \in \mathscr{R}^2 \,|\, 2\omega(x, y, f) - 2e_p \int_{f_0}^{f} \frac{\Omega(x, y)\sin\widetilde{f}}{(1 + e_p\cos\widetilde{f})^2}\mathrm{d}\widetilde{f} \geq C\right\} \tag{2.12}$$

Note the dependency of the pulsating Hill's regions (bounded by the pulsating Hill's curves) on f. It follows that in the elliptic restricted three body problem the forbidden and allowed regions of motion vary according to the mutual motion of P_1 and P_2. This pulsating behaviour of the Hill

regions is shown in Figure 2.3.

The ERTBP possesses five so-called equilibrium points, $L_k, k = 1, ..., 5$. Three of these points (L_1, L_2, L_3) lie along the x-axis. The remaining two, L_4, L_5, lie at the vertices of two equilateral traingles with common base extending from P_1 to P_2 [25]. In the rotating, scaled frame described earlier these points have fixed location. Their actual distance from P_1 to P_2 does vary (pulsate) according to the mutual motion of the primaries.

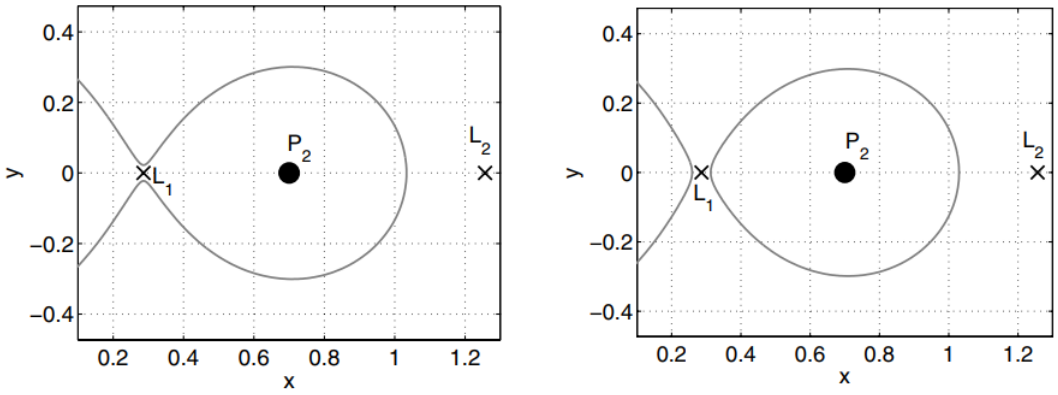

Figure 2.3: Pulsating Hill regions assuming moderate eccentricity ($e = 0.05$) for anomalies left) $f_0 = 0$ and right) $f_0 = \pi$ [11]

In [8] and [24] a further improvement on the description of the circular dynamics was provided. Some of the integrated orbits would lead to collisions of P_3 with P_1 or P_2. In this case the integration of (2.3) would collapse as parameters r_1 and r_2 would approach 0 and the equations of motion would become singular. As stated in [24] use was made of a Levi-Civita regularization, details of which can be found in [22]. A summary is given in [16]. In this work no use is made of regularized equations of motion. As will be shown later, for the purpose of this work it is not required to integrate the equations of motion in the "disk" of specified radius around P_2. Instead, intergration is simply stopped when reaching this disk.

2.2 Polar coordinates

In [24] the work in [8] was reexamined with some modifications. One of these modifications was to use polar coordinates, which would increase the efficiency of the numerical method.

Polar coordinates with respect to P_2, (r_2, θ_2) are used as shown in Figure 2.1. The relation between these P_2-centered polar coordinates and the Cartesian coordinates is given by: [24]

$$x = 1 - \mu + r_2 \cos\theta_2 \qquad y = r_2 \sin\theta_2 \tag{2.13}$$

The polar rotating reference system that is used has the first unit vector alligned with the x-axis and the second perpendicular to it, in direction of increasing θ_2. The equations of motion of P_3 may now be written as: [24]

$$\begin{aligned} \ddot{r}_2 - r_2\dot{\theta}_2^2 - 2r_2\dot{\theta}_2 &= (1-\mu)\cos\theta_2\left(1-\frac{1}{r_1^3}\right) + r_2\left(1-\frac{1-\mu}{r_1^3}\right) - \frac{\mu}{r_2^2} \\ r_2\ddot{\theta}_2 + 2\dot{r}_2\dot{\theta}_2 + 2\dot{r}_2 &= (1-\mu)\sin\theta_2\left(\frac{1}{r_1^3-1}\right) \end{aligned} \tag{2.14}$$

where r_1 represents the distance from P_3 to P_1, and is expressed as $r_1 = \sqrt{r_2^2 + 2r_2\cos\theta_2 + 1}$. A similar approach can be applied to obtain the equations of motion in the P_1-centered polar reference frame: [24]

$$\begin{aligned} \ddot{r}_1 - r_1\dot{\theta}_1^2 - 2r_1\dot{\theta}_1 &= \mu\cos\theta_1\left(\frac{1}{r_2^3}-1\right) + r_1\left(1-\frac{\mu}{r_2^3}\right) - \frac{1-\mu}{r_1^2} \\ r_1\ddot{\theta}_1 + 2\dot{r}_1\dot{\theta}_1 + 2\dot{r}_1 &= \mu\sin\theta_1\left(1-\frac{1}{r_2^3}\right) \end{aligned} \tag{2.15}$$

The integration of trigonometric functions in (2.14) and (2.15) is more computationally intensive than their non-polar counterparts. However, the reduction in integration time due to Conditions (3.6) and (3.7) (explained in Chapter 3) greatly reduces the required computation time as shown in Figure 2.4.

	CPU time (polar) (h)	CPU time (Cartesian) (h)	# Stable orbits	# Regularized orbits
$\mathcal{W}1(0.0)$	27.3	132.2	28212	3612
$\mathcal{W}1(0.2)$	27.4	132.8	24035	4119
$\mathcal{W}1(0.4)$	27.6	130.3	18816	4230
$\mathcal{W}1(0.6)$	27.8	127.0	14479	4815
$\mathcal{W}1(0.8)$	29.7	125.7	10719	4257
$\mathcal{W}1(0.95)$	29.8	122.3	9106	3180

Both codes are written in Matlab language. The CPU time is relative to a Dual Xeon 2.33 GHz platform running Linux. Integration tolerance is set to 10^{-14}

Figure 2.4: Table 1 from [24] displaying numerical efficiency of polar coordinates in comparison with Cartesian coordinates. The meaning of $\mathcal{W}$ will become clear from Chapter 3.

3 | Ballistic Capture

This chapter provides the reader with an overview of the research that has been done in the field of ballistic capture. Similar to the previous chapter, the contents are largely based on the earlier performed literature review [16].

Before the concept of ballistic capture was known, the conventional method of reaching another celestial body was based on a Hohmann transfer. In the case of a Hohmann transfer, two burns are executed at the periapsis and apoapsis of the transfer orbit. A schematic of the Hohmann transfer is given in Figure 3.1

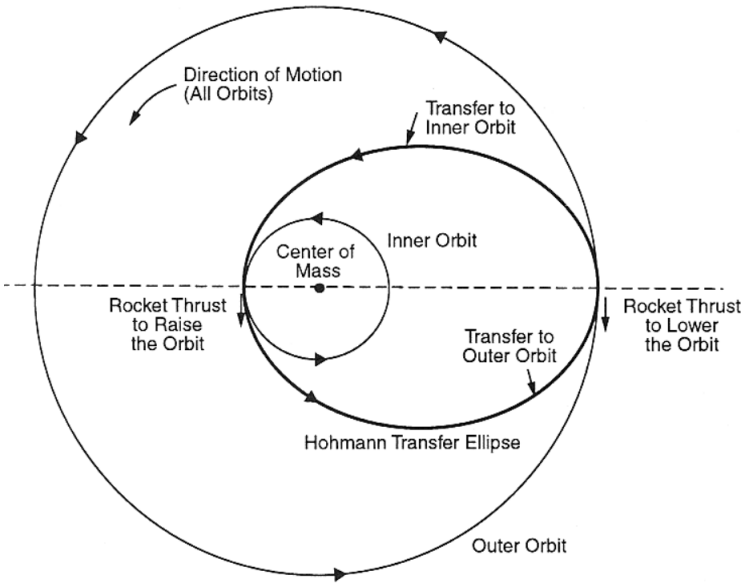

Figure 3.1: A traditional Hohmann transfer [26]

The Hohmann transfer is still considered to be the simplest method of transferring from one planet to another. A patched conics approach can be applied where the central attracting body is changed at the appropriate instance within the transfer. For example, for the Earth-Moon case the initial part of the transfer is governed by the gravitational attraction of the Earth, and only for

the very final part of the transfer the Moon is taken as attracting body. The method is simple in concept, and analytical methods exist to solve for trajectories, but the method inherently involves hyperbolic approaches upon arrival [23].
The mission goal being to get into an orbit around the target planet, the large difference in arrival and target velocity must be shed which requires large amounts of ΔV.

During a ballistic capture the spacecraft does not require a thrusting force when arriving at the target planet to be captured. Instead, the forces required to be captured into an orbit around the target planet are provided by the gravitational attraction of bodies in the solar system. This is very attractive as the high-cost maneuvre at arrival can now be omitted.

An important consideration that needs to be taken into account is the fact that this process can only occur when the spacecraft is under the influence of two bodies. In other words, it can only occur in an n-body problem with $n \geq 3$ [28]. Because no analytical solution exist for these types of problems, it implies that numerical methods must be applied.

The natural gravitational effect may allow the spacecraft to start revolving around the target planet, but the same mechanism may also pull the spacecraft out of this unstable orbit. From a practical perspective, it is therefore necessary to provide some kind of force that would allow the spacecraft to permanently be captured into a stable orbit around the target. This force may come from the spacecraft itself. For example, impulsive shots at designated points within the orbit may be used to lower the orbital altitude. Another option to achieve the same result could be to apply a continuous low-energy thrust to get into a lower, permanent orbit.
For some mission it may even be possible to make use of aerobraking, which allows for a further reduction of insertion costs. If the density of the atmosphere at the relevant altitudes is high enough, the drag force at the periapsis could be used to lower the apoapsis altitude until a desired (circular) orbit is reached.
In the case of NASA's Mars Reconaissance Orbiter, thrusters were used to lower the periapsis of the orbit to an altitude where aerobraking could be possible. From here, the apoapsis altitude of the orbit was lowered over the course of 445 Mars-centered orbits [1].

As mentioned in Chapter 1, ballistic capture trajectories can be found by looking for invariant manifolds in simplified cases, or by making use of stable sets. An elaboration on invariant manifolds is beyond the scope of this research, and as such the remainder of this chapter will focus on the advances that have been made with regards to stable sets.

In Section 3.1 the developments made in finding ballistic capture trajectories in the Circular Re-

[1] https://web.archive.org/web/20060306221449/http://mars.jpl.nasa.gov/mro/mission/tl_aerobraking.html

stricted Three Body Problem will be shown. In Section 3.2 the same is done for an extended model, namely the Elliptic Restricted Three Body Problem. Finally, in Section 3.3 the previous research in extending the theory to n-bodies and three dimensions is given.

3.1 Planar Circular Restricted Three Body Problem

The first step in the development of stable set theory was in the Planar Circular Restricted Three Body Problem (CRTBP). It is a first step, because it is a development of a theory for the minimum amount of bodies ($n = 3$) in a simplified environment (circular orbit approximation).

Firstly H_2 is defined, which is the Kepler energy of P_3 with respect to the primary P_2:

$$H_2 = \frac{v_2^2}{2} - \frac{\mu}{r_2} \tag{3.1}$$

where v_2 is the speed of P_3 relative to the P_2-centered inertial reference frame, r_2 is the distance between P_3 and P_2, and μ is the gravitational parameter. Realizing that the following expression holds for v_2 at initial time:

$$v_2 = \sqrt{\frac{\mu(1+e)}{r_2}} \tag{3.2}$$

where e is the eccentricity of the osculating ellipse. (3.1) and (3.2) may now be combined to yield the following for the Kepler energy H_2 at initial time:

$$H_2 = \frac{1}{2}\frac{\mu(e-1)}{r_2} \tag{3.3}$$

Consider a radial segment $l(\theta)$ departing from the smaller primary P_2 and making an angle θ with the P_1P_2 line defined as the x-axis. We now take trajectories for P_3 starting on $l(\theta)$ that satisfy the following conditions [24]:

- The starting location of P_3 on $l(\theta)$ is on the periapsis of an ellipse whose eccentricity (e) is fixed.
- The initial velocity of P_3 is directed perpendicular to $l(\theta)$.
- The initial Kepler energy H_2, as defined in (3.3), is negative (i.e $H_2 < 0$).

The motion of P_3 is considered to be stable if it leaves $l(\theta)$, makes a complete turn around P_2 and returns to $l(\theta)$ at a point with negative Kepler energy *without* making a complete turn around P_1. If this condition is not satisfied the motion is considered unstable [24].

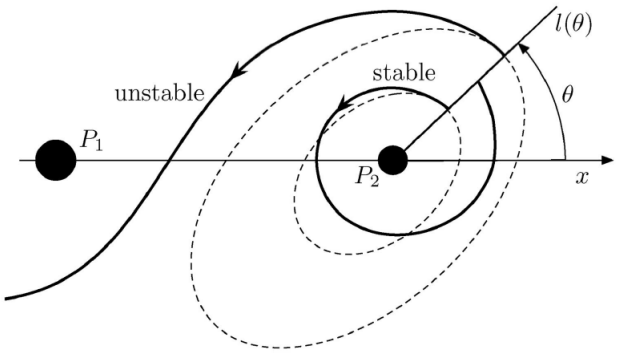

Figure 3.2: Schematic used in the definition of stability [24]

The integration of this orbit is done under the framework of the CRTBP. The motion of P_3 is studied in a rotating coordinate system with coordinates x, y. The origin of this coordinate system lies at the center of mass of P_1 and P_2 as shown in Figure 2.1.

In [1] it is then claimed that, as the initial conditions are varied along $l(\theta)$, there exists a value for the pericenter distance r^* for which the following condition holds true:

- if $r_2 < r^*$ the motion is stable.
- if $r_2 > r^*$ the motion is unstable.

This parameter $r^*(\theta, e)$ is a smooth function of θ and e, and defines the Weak Stability Boundary (WSB):

$$\mathscr{W} = \{r^*(\theta, e) \mid \theta \in [0, 2\pi], e \in [0, 1)\} \tag{3.4}$$

García and Gómez made improvements on this definition in [8], where they made the following remarks:

- It is not certain that there exists this boundary r^* which seperates stable and unstable orbits. The claim was made in [8] that several transitions from stability to instability may exist along $l(\theta)$.
- A maximum time interval must be fixed when integrating the orbits. In [8] this maximum was taken to be 80 days. If an orbit departs from l and does not return to l before this maximum time, the orbit is considered unstable.

In [8] the same methodology as [1] was applied to find transition points r^*, but for fixed values of e and θ, all possible values of r^* were sought along l for which a change in stability occurs. This then yields a finite number of points $r_1^* = 0, r_2^*, ..., r_{2n}^*$ such that if $r_2 \in [r_1^*, r_2^*] \cup [r_3^*, r_4^*] \cup ... \cup [r_{2n-1}^*, r_{2n}^*]$

the motion of P_3 is stable and otherwise unstable [8].
It is now possible to extend the definition of the WSB as the boundary $\partial\bar{\mathscr{W}}$ where:

$$\bar{\mathscr{W}} = \{[r^*_{2k-1}(\theta,e), r^*_{2k}(\theta,e)], k = 1,...,n; \theta \in [0,2\pi], e \in [0,1)\} \tag{3.5}$$

This theory was then applied to the Earth–Moon systen and yielded the results shown in Figure 3.3.

From the results in Figure 3.3 a number of conclusions may be drawn. It is clear that the structure of $\bar{\mathscr{W}}$ is different from what was claimed in [1]: for a single value of θ there exist more than one r^* at which transition from stable to unstable occurs. Furthermore, the shape of $\bar{\mathscr{W}}$ grows more complicated for larger eccentricities.

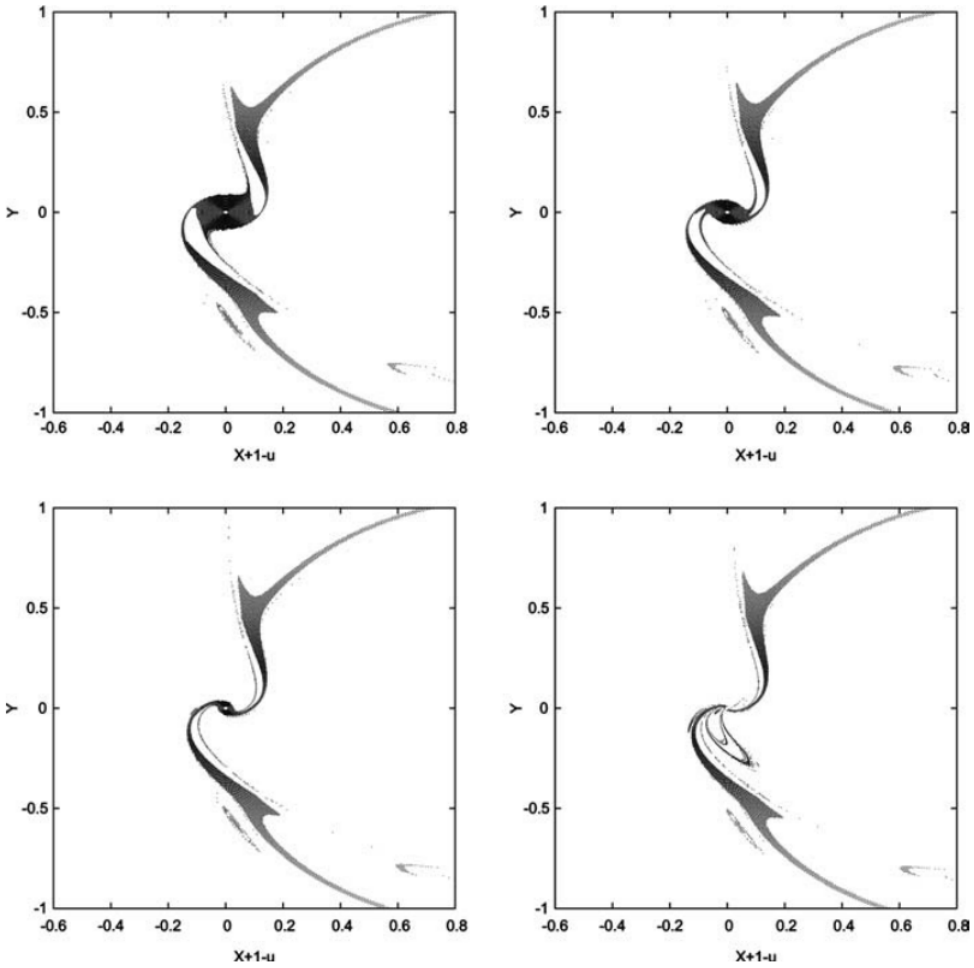

Figure 3.3: From top to bottom and left to right, stable regions for initial conditions with positive velocity (counterclockwise motion as defined in Figure 3.2) and eccentricities e = 0.00, 0.30, 0.60 and 0.90. The origin of the reference system has been set at the small primary P_2 [8]

.

Another improvement that was made in [8] was to include freedom in the number of orbits to define stability, rather than defining it as being the first intersection with l. In this way, $\bar{\mathscr{W}}_n$ can be defined, where n denotes the number of revolutions around P_2 that make the orbit n-stable. This was then applied to the Earth–Moon system again, to yield the results shown in Figure 3.4.

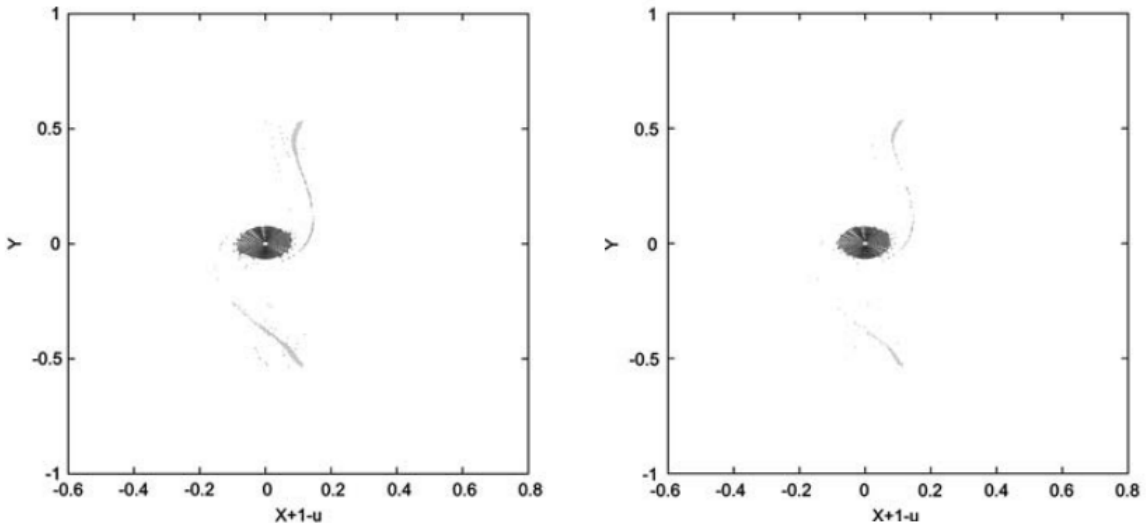

Figure 3.4: Stable regions for initial conditions with positive velocity and $e = 0$ when the number of intersections with l is equal to $n = 3$ (left) and $n = 6$ (right). The origin of the reference system has been set at the small primary P_2 [8]

Comparison between Figures 3.3 and 3.4 shows that increasing the value of n from 1 to 3 yields significantly less orbits. However, there seems to exist a natural "stable limit" in the number of orbits as the value of n is increased further from $n = 3$ to $n = 6$. As is explained in [24], for fixed eccentricities it holds true that $\mathcal{W}_n(e) \subseteq \mathcal{W}_m(e)$ for $n \geq m$. In [24] it is also evident that branches far from P_2 disappear for ever increasing values of n, whereas closer branches become thinner. An interesting phenomenon that occurs is that the core of the stable set is conserved in subsequent sets, which is attributed to the invariant tori surrounding P_2 for fixed values of the Jacobi constant C [6].

In [24], (2.1) is not integrated for a fixed, long time span. Instead, two conditions are introduced. The first of which is an expression which arises if P_3 completes a full turn around P_2 at time t^*:

$$| \theta_2(t^*) - \theta_2(t_0) | = 2\pi \tag{3.6}$$

An analogous expression can be found from the P_1-centered polar reference frame if P_3 complets a complete turn about P_1. In other words, if P_3 performs a primary interchange escape at t^*:

$$| \theta_2(t^*) - \theta_2(t_0) | = 2\pi \tag{3.7}$$

Using the above conditions the numerical integration can be terminated at $t = t^*$ if one of the conditions is satisfied. If Condition (3.6) is satisfied, and if $H_2(t^*) < 0$, the orbit is stable. If Condition (3.7) is satisfied instead, the spacecraft performs primary interchange escape and the orbit is

therefore unstable.

This integration is performed in the polar coordinate system defined in Chapter 2, which combined with the conditions above yielded more efficient computation. The integration time is now by definition $[t_0, t^*]$, and θ_1 and θ_2 are handled as smooth functions of time.

After having performed the integration and found the stable sets $\mathcal{W}$. In [24] the WSB $\partial\mathcal{W}$ is determined from $\mathcal{W}$ by means of a simple yet effective bisection method. In Figure 3.5 an example of a stable set and its weak stability boundary are provided.

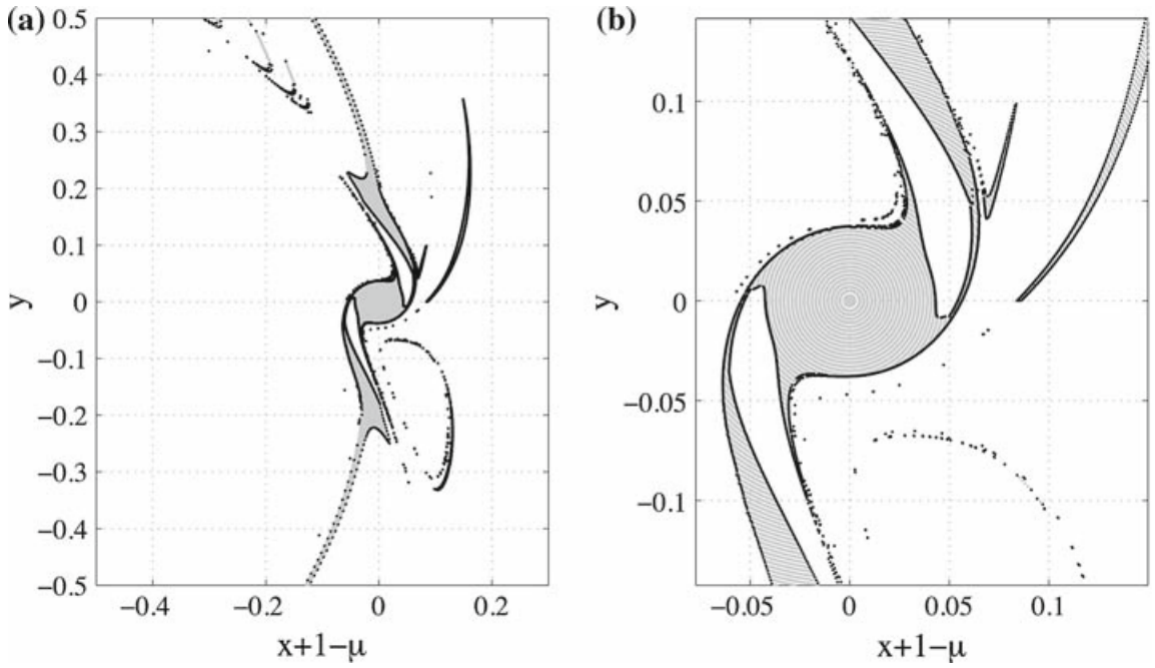

Figure 3.5: a) WSB (black) $\partial\mathcal{W}_1(0.0)$ and 1-stable set $\mathcal{W}_1(0,0)$ (gray) b) detailed version displaying grid [24]

One may wonder how the geometry of the stable set, and thus the corresponding WSB, change for different planet systems. This changing of the planet systems is just a variation of the mass parameter μ. In [24] this was studied by analyzing both the Sun–Jupiter and Earth–Moon systems. The resulting sets are shown in Figure 3.6.

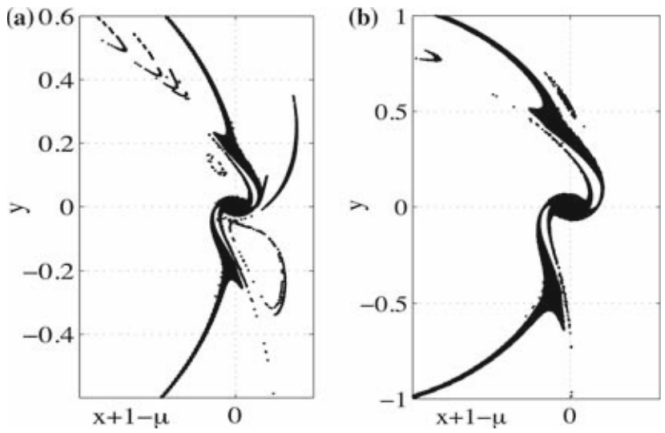

Figure 3.6: $\mathcal{W}_1(0.2)$ for a) Sun–Jupiter and b) Earth–Moon [24]

An interesting conclusion that can be drawn is that the shape of both sets are remarkably similar. However, the relative size is different as the mass ratio of the Earth–Moon system is about 12 times larger than that of the Sun–Jupiter system. Finally, there does seem to be some evidence that a smaller mass ratio leads to a richer trivial set, but this can not be assessed directly [24].

In later work, [21] proposed that backward integrations need be performed in order to find suitable solutions. This is due to the fact that the initial conditions found from the stable sets need to be approached in a natural manner.

In [11] the computation of ballistic trajectories indeed took into account the fact that suitable solutions need to depart from P_2 when integrated backward in time, and must be stable when integrated forward in time. This was achieved by introducing a complementary set to the stable set $\mathcal{W}_n$, namely $\bar{\mathcal{W}}_n$, which is the set corresponding to all unstable orbits. Then, the capture set $\mathcal{C}^n_{-1}$ is defined as follows:

$$\mathcal{C}^n_{-1} = \mathcal{W}_n \cap \bar{\mathcal{W}}_{-1} \tag{3.8}$$

In words: the capture set contains all trajectories which are n-stable when integrated forward in time, and -1-unstable when integrated backwards in time. They approach P_2 and are then stable after n revolutions around P_2. This simple solution allows us to find orbits which do not require any maneuvring, and their motion is completely determined by natural effects.
An additional benefit of the method of [11] is that the set $\bar{\mathcal{W}}_{-1}$ can be filtered to find mission-specific desired arrival trajectories. For example, orbits with oscillating energy values may be filtered out to ensure that strictly unstable orbits are taken. Furthermore, the set can be filtered based on desired arrival paths that are taken. For example, one may want to approach P_2 from a particular area for scientific purposes, or one may want to avoid certain areas that prove danger-

ous for the spacecraft.

3.2 Planar Elliptic Restricted Three Body Problem

As mentioned, the CRTBP assumed circular planetary orbits. The next step in the development of ballistic capture theory was the extension of the theory to the elliptic case, where the assumption of circular orbits is relaxed. This problem is also known as the Elliptic Restricted Three Body Problem (ERTBP). All work carried out in this research is done under the setting of the ERTBP.

As was mentioned in Chapter 2, the allowed regions for the spacecraft vary with the true anomaly due to the pulsating behavior of the Hill regions with time. For that reason, it is important to take a closer look at the true anomaly of P_2 and its role in ballistic capture trajectories. This analysis of relating anomaly to capture behaviour was done in [12], and is summarized below.

A so-called level-function $\mathscr{L}(f_0, f)$ was defined, which is a measure of the present energetic level of the curves of zero velocity (seperating regions) associated to the present position and velocity [12]. Due to the pulsating nature in the elliptic case this level-function varies along the trajectory. After defining the level function at the ith Lagrange point (i.e: $\mathscr{L}_i = \mathscr{L}_i(f_0, f)$) the following was proposed for i = 1,2:

In the ERTBP, for a given true anomaly f, cases (a), (b), and (c) take place when the following conditions are verified

(a) $\mathscr{L}(f_0, f) \geq \mathscr{L}_1$

(b) $\mathscr{L}_2 \leq \mathscr{L}(f_0, f) < \mathscr{L}_1$

(c) $\mathscr{L}_3 \leq \mathscr{L}(f_0, f) < \mathscr{L}_2$

where verification of case (c) also implies verification of case (b). After defining that $f = f_0$ is taken to be the periapsis point of the osculating ellipse, it is then stated in [12] that an ideal ballistic capture orbit is one where cases (b) and (c) are verified for $f \leq f_0$ and case (a) is verified for $f > f_0$.
In this way, the spacecraft approaches P_2 when the inner region is accessible, and it is trapped from f_0 onwards inside the region. This attractive feature may be exploited in order to increase the chances of capture. One must note that these conditions are not necessary nor sufficient to ensure ballistic capture trajectories. Rather they only provide us with necessary conditions for ideal orbits.

Using the signs of the first and second derivatives of the level function, it is then found that choosing an initial true anomaly in the first quadrant, i.e: $f_0 \in [0, \pi/2]$, is a good choice to generate ideal

ballistic capture orbits. In this domain, the duration of the backward integration will decrease the region P_2 more quickly than that the P_2 region contracts in the forward integration. This allows having a quick ballistic approach and a long term capture [12].

One must note that it is possible to find orbits which satisfy the condition that case (a) and (b) are verified before f_0, and case (c) is verified after f_0, but which do not satisfy the condition $f_0 \in [0, \pi/2]$. In fact, it may even be possible that quantitatively *more* orbits are found outisde the proposed optimal f_0 domain. This does, however, not indicate a qualitatively better solution, as is indicated by Figure 3.7.

It is evident from Figure 3.7 that orbit (a) is much more regular than orbit (b), which even undergoes a sign change of the angular momentum [12]. In this analysis it was the case that quantitatively more orbits were generated outside the optimal domain, but it is clear that the quality of the solutions inside the optimal f_0 domain is superior. It may be noted that in [4] similar results were obtained, where the preferential region of capture was found to be around perihelion of the target planet.

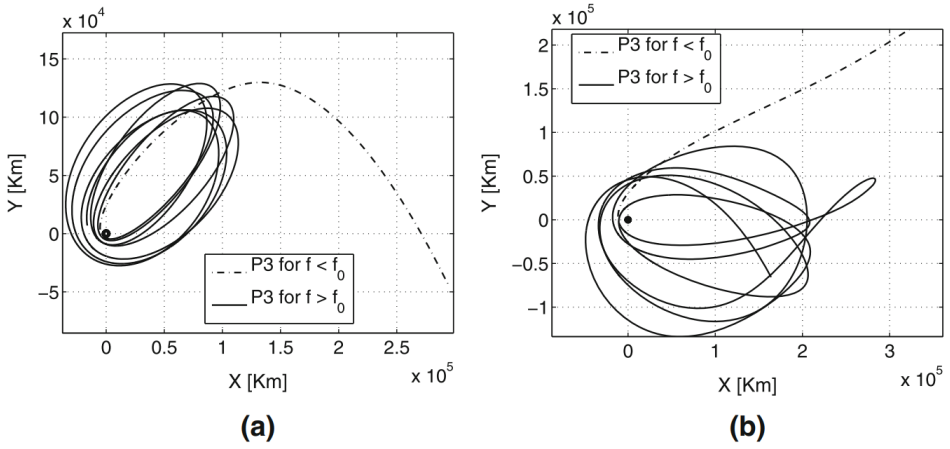

Figure 3.7: Two obtained ballistic capture orbits around Jupiter for a) $f_0 = 0.25\pi$ b) $f_0 = 1.25\pi$ [12]

3.3 Extension to n-bodies and three dimensions

The aforementioned work done had proven to be insightful, as it provided qualitative information about ballistic capture trajectories. There was, however, still a lack of practical solutions that would be applicable in the real solar system model where out-of-plane behaviour and fourth body perturbations are a factor.

In this research work is carried out in the framework of the ERTBP, because the state of the art research linking Lagrangian Coherent Structures to ballistic capture is still in its infancy. When further developments in the field are made for three dimensions and n-bodies, the work done

within the field of three dimensional study of ballistic capture (see for example [19], [28], and [27]) will be more relevant. For a summary of ballistic capture research in n-bodies and three dimensions, the reader is referred to Section 3.3 of [16].

4 | Lagrangian Coherent Structures

This chapter forms the final part of the literature synthesis, and is again based largely on the contents of [16].

The study of flowing fluids has always been an important field of study in engineering. It allows for analysis of an air flow around an aircraft wing, the prediction of motion of gases in the air and oil spills in oceans. As such it not only has value in a theoretical framework, but the real-life applications range widely.

The complex dynamics of these flowing fluids are completely described by the Navier-Stokes equations. These equations, however, prove to be analytically unsolvable. In fact, they require numerical analysis which may give rise to a whole new set of complications [13]. Another option for analysis of these fluids is to simplify the problem to a state which allows us to approximate the scenario with a reasonable accuracy whilst keeping the degrees of freedom to a minimum.
Attempts have been made to simplify this problem, and an appealing solution is to decompose the fluid flow into *coherent structures*, which are "skeletons" within the fluid that seperate regions with different dynamics.
When the structures are defined in a fixed coordinate system, they are referred to as Eulerian Coherent Structures. When they are defined relative to the motion of individual fluid elements, they are called Lagrangian Coherent Structures.

In this chapter the developments made in the field of Lagrangian Coherent Structures will be studied. In Section 4.1 some definitions regarding dynamical systems will be given, as these prove to be essential in understanding Lagrangian Coherent Structures. In Section 4.2 a classification of Lagrangian Coherent Structures is given. Sections 4.3 and 4.4 serve as a summary of the two methods with which Lagrangian Coherent Structures can be computed, namely Finite-Time Lyapunov Exponent and Variational theory, respectively. Finally, Section 4.5 shows how Lagrangian Coherent Structures have been linked to ballistic capture and stable sets in previous studies.

4.1 Dynamical Systems

A dynamical system is traditionally defined as a system in which the dependence of a point in geometrical space on time is given through a function. It is essentially a model which descibes the evolution of a system with time. Dynamical systems have a wide range of applicability such as in engineering, biology, physics, and economics.

A fundamental problem in the theory of dynamical systems is to find a solution of a differential equation for which initial data is provided. This problem is referred to as a *Cauchy problem,* and may be defined mathematically as finding the solution x for the differential equation that satisfies the so-called system equation:

$$\begin{cases} \dot{\mathbf{x}} = \mathbf{f}(\mathbf{x}) & \text{for } \mathbf{x} \in \mathscr{S} \\ \mathbf{x}(t_0) = \mathbf{x}_0 & \text{for } \mathbf{x} \in \mathscr{S} \end{cases} \tag{4.1}$$

Following this notation, we may also define the flow map $\phi_{t_0}^t$, which maps the initial position $\mathbf{x}_0$ of the trajectory onto its position at time t:

$$\mathbf{x}_0 \mapsto \phi_{t_0}^t(\mathbf{x}_0) = x(t; t_0, \mathbf{x}_0) \tag{4.2}$$

Using the definition of the flow map, we may now define the variational equation. The variational equation gives us a mathematical representation of how the behaviour of the state changes if we were to perturb $\mathbf{x}_0$ in some way. It therefore presents us with additional information to the evolving behaviour of the state given by the state equation.

We define:

$$\Phi := \Phi(t; t_0, \mathbf{x}_0) = D_{\mathbf{x}_0}\phi_{t_0}^t(x_0) \qquad \mathbf{A}(\mathbf{x}, t) = D_x\mathbf{f}(\mathbf{x}, t) \tag{4.3}$$

where $\Phi(t; t_0, \mathbf{x}_0)$ is the state transition matrix, which allows us to carry over the state from time t_0 to t, and $\mathbf{A}(\mathbf{x}, t)$ is the Jacobian of the vector field. The variational equation is then defined as:

$$\begin{cases} \dot{\Phi} = \mathbf{A}(\mathbf{x}, t)\Phi & \text{for } \mathbf{x} \in \mathscr{S} \\ \Phi(t_0; t_0, \mathbf{x}_0) = \mathbf{I}_n & \text{for } \mathbf{x} \in \mathscr{S} \end{cases} \tag{4.4}$$

where I_n is the n-dimensional identity matrix.

It is required to solve both sets of equations (variational equation and system equation) simultaneously as the variations react to the differential slopes at each point in the trajectory. Since (4.1) is n-dimensional, and (4.4) is n^2-dimensional, the total system is described by $n^2 + n$ equations.

4.2 Classification of Lagrangian Coherent Structures

As mentioned in the introduction of this chapter, Lagrangian Coherent Structures are defined as core surfaces around which trajectory patterns form. As had already been defined in [10], three types of LCSs may be defined:

- Repelling LCS: core structures generating stretching.
- Attracting LCS: centerpieces of folding.
- Shear LCS: outline swirling and jet-type tracer patterns.

Furthermore, it was claimed in [10] that an LCS must always possess the following two properties:

- An LCS should be a *material surface*. If we define a curve of initial conditions on the **x** plane as Γ_0, then we may define a deforming material line Γ_t as later images of Γ_0 at time t. This line spans a two-dimensional surface $\mathscr{M}(t)$ in the $(\mathbf{x}, t)$ space, and is called a material surface. This is displayed graphically in Figure 4.1. The reason that an LCS should be a material surface is because (a) its dimension should be high enough such that it has visible impact and may act as a transport barrier and (b) it must move with the flow to allow for an observable evolution of LCS patterns.

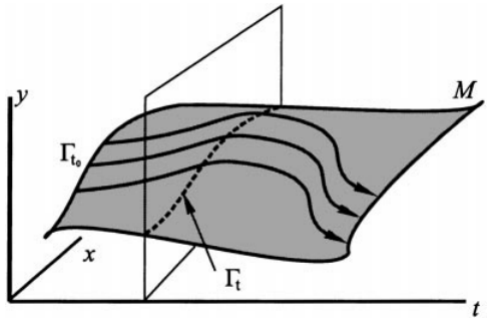

Figure 4.1: Γ_t, which is an evolving material curve, spans out the material surface $\mathscr{M}(t)$ [10]

- An LCS should locally display the strongest attraction, repulsion, or shear in a flow.

For the purpose of this work, only LCSs which are local attractors or repellors are of concern. These are classicaly defined as *Hyperbolic LCS*. The geometry behind this definition is shown in Figure 4.2.

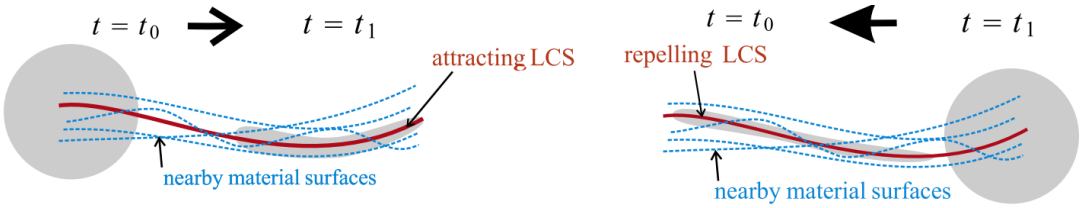

Figure 4.2: Geometrical representation of attracting and repelling LCS, more generally defined as hyperbolic LCS [9]

4.3 Finite Time Lyapunov Exponent

In this section the method involving Finite Time Lyapunov Exponents (FTLE) will be explained. FTLE was the first theory developed to compute Lagrangian Coherent Structures.
In order to ensure consistency in notation, the following dynamical system is used throughout this section, as used in [9]:

$$\dot{\mathbf{x}} = \mathbf{v}(\mathbf{x}, t) \qquad \mathbf{x} \in U \qquad t \in [\alpha, \beta] \tag{4.5}$$

where $\mathbf{v}(\mathbf{x}, t)$ is a smooth vector field defined on the n-dimensional, bounded, open domain U over a time interval $[\alpha, \beta]$. The dot indicates differentiation with respect to time t.

According to the definition given of hyperbolic LCS which involves repulsion and attraction, it is intuitive to explore the maximum local separation rate in (4.5) to define the LCS. This seperation rate is called the finite-time Lyapunov Exponent.

We now consider a neighboring point close to $\mathbf{x}$, denoted as $\mathbf{y} = \mathbf{x} + \delta\mathbf{x}(t_0)$ where δ indicates a difference in position. After a time T this difference in position in the flow becomes:

$$\delta\mathbf{x}(t_0+T) = \phi_{t_0}^{t_0+T}(\mathbf{y}) - \phi_{t_0}^{t_0+T}(\mathbf{x}) = \frac{d\phi_{t_0}^{t_0+T}(\mathbf{x})}{d\mathbf{x}}\delta\mathbf{x}(t_0) + \mathcal{O}(\|\delta\mathbf{x}(t_0)\|^2) = \Phi\cdot\delta\mathbf{x}_0 + \mathcal{O}(\|\delta\mathbf{x}(t_0)\|^2) \tag{4.6}$$

which follows from a Taylor series expansion of the flow about point $\mathbf{x}$, and Φ is the earlier defined state transition matrix. If we neglect the $\mathcal{O}(\|\delta\mathbf{x}(t_0)\|^2)$ term due to $\delta\mathbf{x}(t_0)$ being infinitesimal, we may write the magnitude of the difference in position as:

$$\|\delta\mathbf{x}(t_0+T)\| = \sqrt{\langle\Phi\cdot\delta\mathbf{x}(t_0), \Phi\cdot\delta\mathbf{x}(t_0)\rangle} = \sqrt{\delta\mathbf{x}(t_0)^T\cdot\Phi^T\Phi\cdot\delta\mathbf{x}(t_0)} \tag{4.7}$$

We now define $\Phi^T\Phi$ as the *Cauchy-Green deformation tensor* Δ, which is a function of t_0, T, and $\mathbf{x}$.

Recall that the LCS was related to maximum local separation rate. As such, we are interested in the maximum deformation that occurs between $\mathbf{x}$ and $\mathbf{y}$. This occurs when $\delta\mathbf{x}(t_0)$ is chosen such

that it aligns with the eigenvector associated to the maximum eigenvalue of Δ.

The average logarithmic expansion rate (Finite Time Lyapunov Exponent) $\sigma_{t_0}^{T}(\mathbf{x})$ is now obtained by taking the natural logarithm of the coefficient of expansion (which is the square root of the maximum eigenvalue) and dividing by the integration time:

$$\sigma_{t_0}^{T}(\mathbf{x}) = \frac{1}{T}\ln\sqrt{\lambda_n(\Delta)} = \frac{1}{2T}\ln\lambda_n(\Delta) \tag{4.8}$$

where λ_n is the maximum eigenvalue of Δ and T is the integration time. The ridges of the obtained FTLE field then corresponding to the hyperbolic LCSs.

In [9] it was found that this definition can not readily be used to find LCSs. The following remarks were made:

- Observable LCS are not necessarily ridges of the FTLE field, as shown in Figure 4.3.

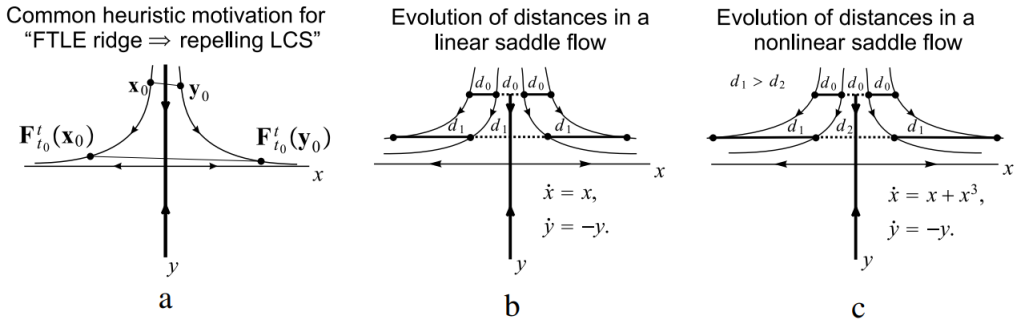

Figure 4.3: a) Common motivation for the claim that FTLE ridges mark repelling LCS. b) Example of system with observable repelling LCS at x = 0 but no FTLE ridge c) Example of system with observable repelling LCS and trough at x = 0 [9]

- Ridges of the FTLE are not necessarily observable LCSs. In fact, these ridges may be indicators of shear or local large stretching where no underlying structure is present. In some cases the FTLE ridges are in fact very far from any Lagrangian structure.

In order to resolve these inconsistencies, a new theory needed to be developed. This theory is explained in Section 4.4.

4.4 Variational Theory

In [9] a new theory was proposed that would solve the inconsistencies that arise in the FTLE method, namely the variational theory.

Consider an arbitrary point $\mathbf{x}_0 \in \mathscr{M}(t_0)$. At this point, we define the $n-1$ dimensional tangent space $T_{\mathbf{x}_0}\mathscr{M}(t_0)$ of $\mathscr{M}(t_0)$ and a 1-dimensional normal space $N_{\mathbf{x}_0}\mathscr{M}(t_0)$ as shown in Figure 4.4.

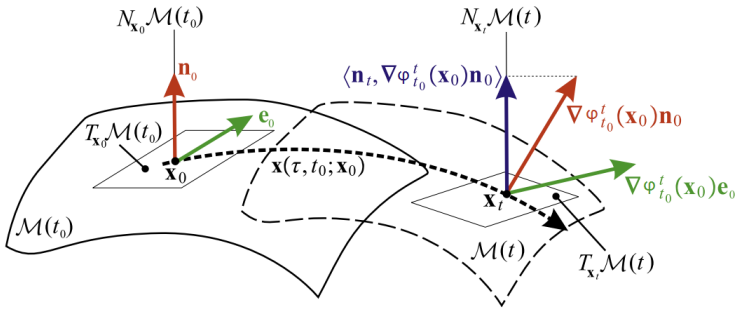

Figure 4.4: Geometry used in the formulation of variational theory [9]

The earlier defined flow map can be used to propagate the tangent space $T_{\mathbf{x}_0}\mathscr{M}(t_0)$ along the trajectory as follows (where $\mathbf{x}_0 = \mathbf{x}(t_0)$):

$$T_{\mathbf{x}_t}\mathscr{M}(t) = \nabla\phi^t_{t_0}(\mathbf{x}_0)\, T_{\mathbf{x}_0}\mathscr{M}(t) \tag{4.9}$$

where $\nabla\phi^t_{t_0}(\mathbf{x}_0)$ represents the linearized flow map.
The unit vector $\mathbf{e}_0 \in T_{\mathbf{x}_0}\mathscr{M}(t_0)$ is also mapped to the point $\mathbf{x}_t$ in a similar fashion into $\nabla\phi^t_{t_0}(\mathbf{x}_0)\mathbf{e}_0$. As it turns out, this mapped vector is contained within the space tangent to $\mathscr{M}_t$. However, it is shown that $\nabla\phi^t_{t_0} N_{\mathbf{x}_0}\mathscr{M}(t)$ is not necessarily contained in the normal space $N_{\mathbf{x}_t}\mathscr{M}(t)$. As such, the vector $\nabla\phi^t_{t_0}(\mathbf{x}_0)\mathbf{e}_0$ will be a vector of general orientation as is shown in Figure 4.4.

We define the projection of $\nabla\phi^t_{t_0}(\mathbf{x}_0)\mathbf{e}_0$ onto $\mathbf{n}_t$ (where $\mathbf{n}_t \in N_{\mathbf{x}_t}\mathscr{M}_t$) as the *repulsion rate*:

$$\rho^t_{t_0}(\mathbf{x}_0, \mathbf{n}_0) = \langle \mathbf{n}_t, \nabla\phi^t_{t_0}(\mathbf{x}_0)\mathbf{n}_0\rangle \tag{4.10}$$

If the value of this projection $\rho^t_{t_0}(\mathbf{x}_0, \mathbf{n}_0) > 1$, the normal component grows from t_0 to t. Conversely, a value $\rho^t_{t_0}(\mathbf{x}_0, \mathbf{n}_0) < 1$ indicates that the normal component has decreased.

Furthermore, a *repulsion ratio* is defined, which gives a measure of the ratio between normal and tangential growth along $\mathscr{M}(t)$ over $[t_0, t]$:

$$\nu^t_{t_0}(\mathbf{x}_0, \mathbf{n}_0) = \min_{\substack{\|\mathbf{e}_0\|=1 \\ \mathbf{e}_0 \in T_{\mathbf{x}_0}\mathscr{M}(t_0)}} \frac{\langle \mathbf{n}_t, \nabla\phi^t_{t_0}(\mathbf{x}_0)\mathbf{n}_0\rangle}{\left\|\nabla\phi^t_{t_0}(\mathbf{x}_0)\mathbf{e}_0\right\|} \tag{4.11}$$

If $\nu^t_{t_0}(\mathbf{x}_0, \mathbf{n}_0) > 1$, the normal growth along $\mathscr{M}(t)$ dominates the largest tangential growth over the time interval $[t_0, t]$. In such a case $\mathscr{M}(t)$ is a locally dominant repelling structure.

In a practical application these quantities $\rho_{t_0}^{t}$ and $\nu_{t_0}^{t}$ can be computed and estimated as shown in (4.12) and (4.13) respectively.

$$\begin{aligned}\rho_{t_0}^{t}(\mathbf{x}_0,\mathbf{n}_0) &= \frac{1}{\sqrt{\langle \mathbf{n}_0, \left[\Delta_{t_0}^{t}(\mathbf{x}_0)\right]^{-1}\mathbf{n}_0\rangle}} \\ \nu_{t_0}^{t}(\mathbf{x}_0,\mathbf{n}_0) &= \min_{\substack{\|\mathbf{e}_0\|=1 \\ \mathbf{e}_0\in T_{\mathbf{x}_0}\mathscr{M}(t_0)}} \frac{\rho_{t_0}^{t}(\mathbf{x}_0,\mathbf{n}_0)}{\sqrt{\langle \mathbf{e}_0, \Delta_{t_0}^{t}(\mathbf{x}_0)\mathbf{e}_0\rangle}}\end{aligned} \tag{4.12}$$

$$\begin{aligned}\sqrt{\lambda_1(\mathbf{x}_0,t_0,T)} \le \rho_{t_0}^{t_0+T}(\mathbf{x}_0,\mathbf{n}_0) \le \sqrt{\lambda_n(\mathbf{x}_0,t_0,T}} \\ \frac{\sqrt{\lambda_1(\mathbf{x}_0,t_0,T)}}{\sqrt{\lambda_n(\mathbf{x}_0,t_0,T}} \le \nu_{t_0}^{t_0+T}(\mathbf{x}_0,\mathbf{n}_0) \le \frac{\sqrt{\lambda_n(\mathbf{x}_0,t_0,T}}{\sqrt{\lambda_1(\mathbf{x}_0,t_0,T}}\end{aligned} \tag{4.13}$$

The repulsion rate and repulsion ratio may now be used to give a formal definition of a finite-time hyperbolic material surface: A material surface $\mathscr{M}(t) \in U$ is normally repelling over $[t_0, t_0+T]$ if there exist constants $a, b > 0$ such that for all points $\mathbf{x}_0 \in \mathscr{M}(t_0)$ and unit normals $\mathbf{n}_0 \in N_{\mathbf{x}_0}\mathscr{M}(t_0)$ we have:

$$\begin{aligned}\rho_{t}^{t_0+T}(\mathbf{x}_0,\mathbf{n}_0) > 1 \\ \nu_{t}^{t_0+T}(\mathbf{x}_0,\mathbf{n}_0) > 1\end{aligned} \tag{4.14}$$

In a similar fashion the material surface is normally attracting if it is normally repelling over $[t_0, t_0+T]$ in backward time. If the surface is either repelling or attracting it can be said to be a hyperbolic material surface.

In order to further define a material surface as an LCS, firstly a definition of a *Weak LCS WLCS* is given. For a material surface to be a WLCS it is required that if $\mathscr{M}(t)$ is a repelling WLCS, it must be pointwise more repelling over $[t_0, t_0+T]$ than any other nearby material surface. In mathematical terms: at any point $\mathbf{x}_0 \in \mathscr{M}(t_0)$, if we were to perturb $\mathscr{M}(t_0)$ along its normal $\mathbf{n}_0 \in N_{\mathbf{x}_0}\mathscr{M}(t_0)$, the obtained values of $\rho_{t_0}^{t_0+T}(\hat{\mathbf{x}}_0,\hat{\mathbf{n}}_0)$ at the perturbed states must be smaller than $\rho_{t_0}^{t_0+T}(\mathbf{x}_0,\mathbf{n}_0)$. If the material surface is a repelling WLCS in backward time, the material surface is defined as an attracting WLCS. The methodology is shown graphically in Figure 4.5.

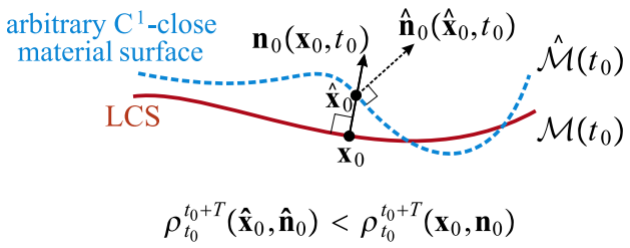

Figure 4.5: Geometry used in defining a normally repelling material surface as a repelling WLCS [9]

In specific terms we require the derivative of the repulsion rate field $\rho_t^{t_0+T}(\hat{\mathbf{x}}_0,\hat{\mathbf{n}}_0)$ to be zero in the direction of $\mathbf{n}_0(\mathbf{x}_0,t_0)$. This does, however, not guarantee a unique core of a coherent trajectory pattern. To further strengthen the definition in order to obtain hyperbolic LCS, we require a nondegenerate maximum in the normal repulsion rate. A nondegenerate maximum is a local maximum for $\rho_{t_0}^{t_0+T}(\mathbf{x}_0,\mathbf{n}_0)$ with a nondegenerate second derivative with respect to changes normal to $\mathcal{M}(t_0)$.

At this point, in [9] the sufficient and necessary conditions for weak LCS and LCS are given: consider a compact material surface $\mathcal{M}(t) \subset U$ over the interval $[t_0, t_0+T]$. Then $\mathcal{M}(t)$ is a repelling WLCS over $[t_0, t_0+T]$ if and only if the following three conditions hold for all $\mathbf{x}_0 \in \mathcal{M}(t_0)$:

- $\lambda_{n-1}(\mathbf{x}_0,t_0,T) \neq \lambda_n(\mathbf{x}_0,t_0,T) > 1$
- $\xi_n(\mathbf{x}_0,t_0,T) \perp T_{\mathbf{x}_0}\mathcal{M}(t_0)$
- $\langle \nabla\lambda_n(\mathbf{x}_0,t_0,T), \xi_n(\mathbf{x}_0,t_0,T)\rangle = 0$

Furthermore, $\mathcal{M}(t)$ is a repelling LCS over $[t_0, t_0+T]$ if and only if the following two conditions hold:

- $\mathcal{M}(t)$ is a repelling WLCS over $[t_0, t_0+T]$
- The matrix $\mathbf{L}(\mathbf{x}_0,t_0,T)$ is positive definite for all $\mathbf{x}_0 \in \mathcal{M}(t_0)$

where ξ_n is the eigenvector corresponding to the largest eigenvalue of $\Delta(\mathbf{x}_0)$, λ is an eigenvalue of Δ, and the matrix $\mathbf{L}$ is given by:

$$\mathbf{L} = \begin{pmatrix} \nabla^2\Delta^{-1}[\xi_n,\xi_n,\xi_n,\xi_n] & 2\frac{\lambda_n-\lambda_1}{\lambda_1\lambda_n}\langle\xi_1,\nabla\xi_n\xi_n\rangle & \dots & 2\frac{\lambda_n-\lambda_{n-1}}{\lambda_{n-1}\lambda_n}\langle\xi_{n-1},\nabla\xi_n\xi_n\rangle \\ 2\frac{\lambda_n-\lambda_1}{\lambda_1\lambda_n}\langle\xi_1,\nabla\xi_n\xi_n\rangle & \frac{2\lambda_n-\lambda_1}{\lambda_1\lambda_n} & \dots & 0 \\ \vdots & \vdots & \ddots & \vdots \\ 2\frac{\lambda_n-\lambda_{n-1}}{\lambda_{n-1}\lambda_n}\langle\xi_{n-1},\nabla\xi_n\xi_n\rangle & 0 & \dots & \frac{2\lambda_n-\lambda_{n-1}}{\lambda_{n-1}\lambda_n} \end{pmatrix} \tag{4.15}$$

where the first term of the diagonal is given by:

$$\nabla^2\Delta^{-1}[\xi_n,\xi_n,\xi_n,\xi_n] = -\frac{1}{\lambda_n^2}\langle\xi_n,\nabla^2\lambda_n\xi_n\rangle + 2\sum_{q=1}^{n-1}\frac{\lambda_n-\lambda_q}{\lambda_q\lambda_n}\langle\xi_q,\nabla\xi_n\xi_n\rangle^2 \tag{4.16}$$

One may note that this matrix **L** does not have any meaning. It only functions as a tool to aid in the definition of an LCS.

4.5 Relevance to Ballistic Capture

The aim of this section is to provide some information on the applicability of Lagrangian Coherent Structures to the main topic studied for the thesis, which is ballistic capture. In [18] a fruitful effort was made to combine the two fields and to use Lagrangian Coherent Structures to compute the boundaries of the stable sets.

In order to do so, the 2D equations of motion of particle P_3 in the ERTBP were rewritten:

$$\begin{cases} \dot{x} = v_x \\ \dot{y} = v_y \\ \dot{v}_x = 2v_y + \frac{\partial\omega}{\partial x} \\ \dot{v}_y = -2v_x + \frac{\partial\omega}{\partial y} \end{cases} \tag{4.17}$$

As per Section 4.1, the set of variational equations constitutes of $n + n^2 = 4 + 4^2 = 20$ equations.

To formalize the computation procedure, a composition of functions was defined, as shown in Figure 4.6.

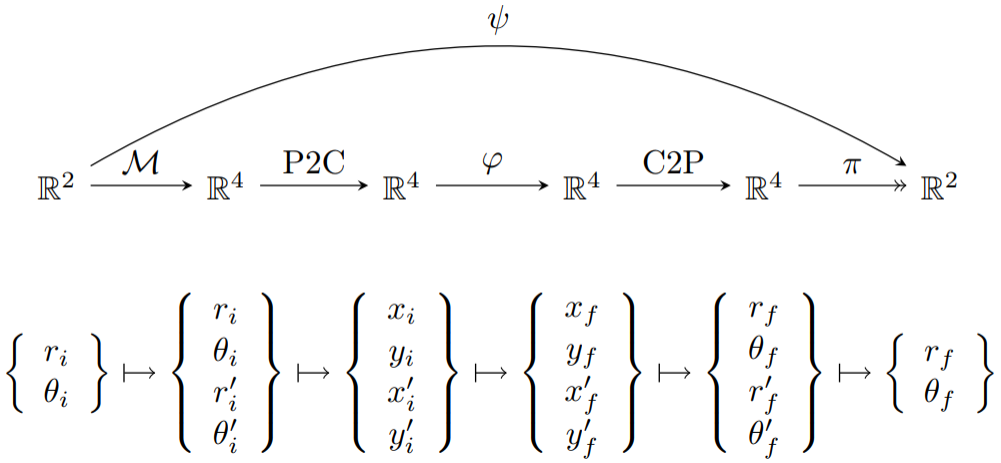

Figure 4.6: Composition of functions used in problem [18]

In Figure 4.6 subscripts i and f represent initial and final states, respectively. The functions used are described as follows:

- $\mathscr{M}$ is the map which allows us to convert the two-dimensional phase space to a four-dimensional one. It is given by:

$$\mathscr{M}(r_i,\theta_i) = \begin{cases} r_i = r_i \\ \theta_i = \theta_i \\ \dot{r}_i = \frac{r_i e_p \sin f_0}{1+e_p \cos f_0} \\ \dot{\theta}_i = \sqrt{\frac{\mu(1+e)}{r_i^3(1+e_p \cos f_0)}} - 1 \end{cases} \tag{4.18}$$

- P2C changes the polar form of the initial state to a Cartesian form according to:

$$P2C(r_i,\theta_i,\dot{r}_i,\dot{\theta}_i) = \begin{cases} x_i = 1-\mu+r_i\cos\theta_i \\ y_i = r_i \sin\theta_i \\ \dot{x}_i = \dot{r}_i\cos\theta_i - r_i\dot{\theta}_i\sin\theta_i \\ \dot{y}_i = \dot{r}_i\sin\theta_i + r_i\dot{\theta}_i\cos\theta_i \end{cases} \tag{4.19}$$

- ϕ propagates the orbit according to the equations of motion given in (4.17), repeated below:

$$\begin{cases} \dot{x} = v_x \\ \dot{y} = v_y \\ \dot{v}_x = 2v_y + \frac{\partial\omega}{\partial x} \\ \dot{v}_y = -2v_x + \frac{\partial\omega}{\partial y} \end{cases} \tag{4.20}$$

- C2P is the inverse of P2C, and as such converts the Cartesian reference system back to a polar one.

$$C2P(x_f,y_f,\dot{x}_f,\dot{y}_f) = \begin{cases} r_f = \sqrt{(x_f-1+\mu)^2+y_f^2} \\ \theta_f = \mathrm{atan2}(\mathrm{y_f},(\mathrm{x_f}-1+\mu)) \\ \dot{r}_f = \frac{(x_f-1+\mu)\dot{x}_f + y_f\dot{y}_f}{r_f} \\ \dot{\theta}_f = \dot{r}_i\sin\theta_i + r_i\dot{\theta}_i\cos\theta_i \end{cases} \tag{4.21}$$

- π converts the four-dimensional final polar state to a two-dimensional one.

$$\pi(r_f,\theta_f,\dot{r}_f,\dot{\theta}_f) = \begin{cases} r_f = r_f \\ \theta_f = \theta_f \end{cases} \tag{4.22}$$

As shown, ψ is the flow of the complete 2-dimensional dynamical system. This flow may be computed using the chain rule considering each of the individual functions, and its Cauchy-Green strain tensor is given by $\Delta = \Psi^T \Psi$ where $\Psi = \frac{D\psi}{\partial r \partial \theta}(r_i, \theta_i)$ is the Jacobian of the flow.
The Jacobian of the flow is computed numerically when integrating the variational equations. All other Jacobians (i.e: Jacobians for each transformation mentioned above) are computed by hand. For efficiency sake the analytical expressions for the Jacobians are not mentioned here. Instead, they are provided in Appendix B as accompanying code.
In [18] the necessary and sufficient conditions for an LCS given according to variational theory given earlier were reformulated for two-dimensional flows according to [7]. The results as shown in Figure 4.7 were obtained:

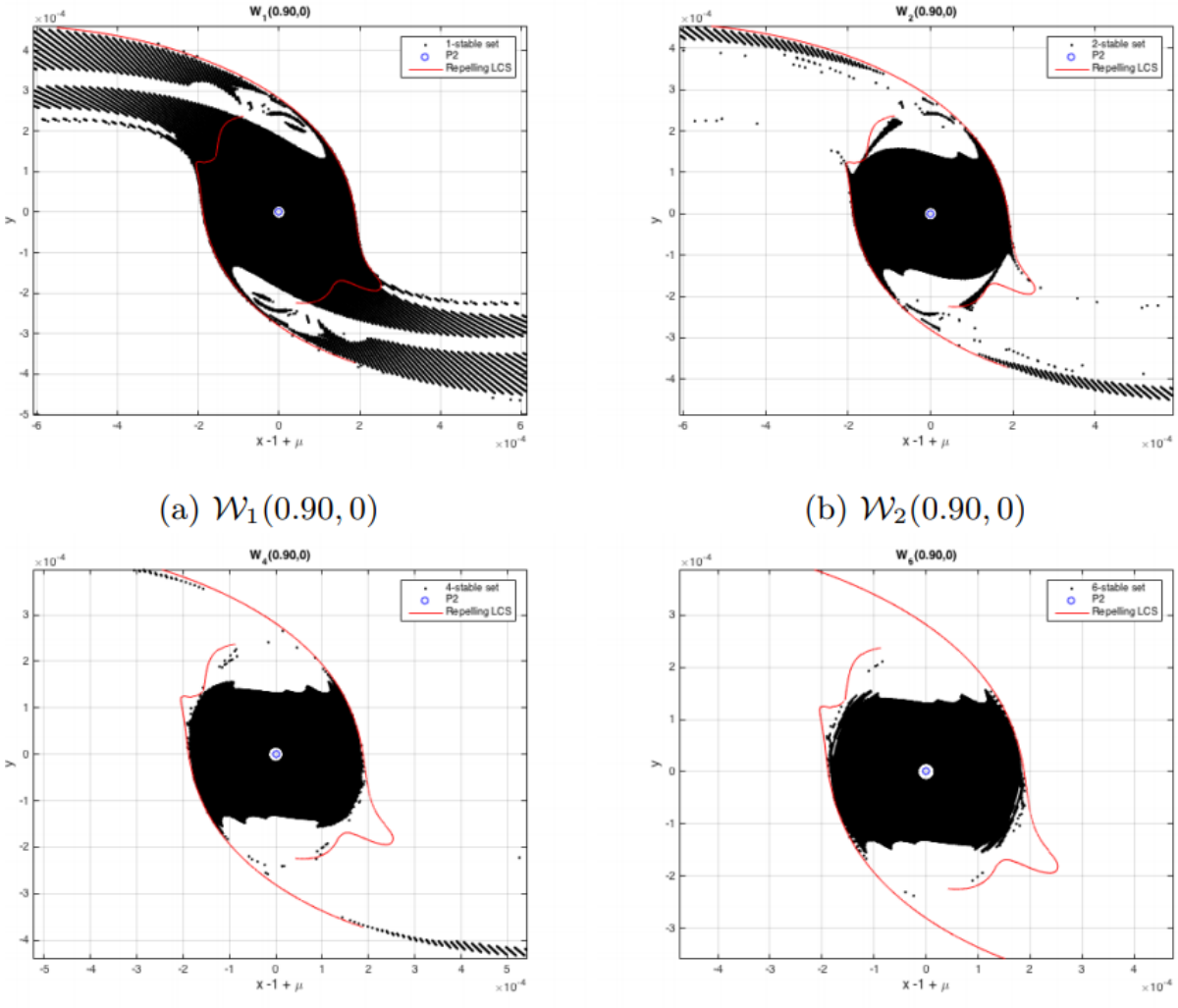

(a) $\mathcal{W}_1(0.90, 0)$ (b) $\mathcal{W}_2(0.90, 0)$

(c) $\mathcal{W}_4(0.90, 0)$ (d) $\mathcal{W}_6(0.90, 0)$

Figure 4.7: n-stable sets for the Sun-Mars system [18]

The plots in Figure 4.7 show the stable sets and the corresponding repelling LCS. It can be seen that the LCS corresponds to the boundary in the right and left wings, but for the upper and bottom parts the lines do not match. It was concluded that repelling LCS are more sensitive to the different dynamics of the particles. Another explanation for the "poor" matching is due to the fact that the LCS are computed using a fixed integration time, whilst the integration time of each particle in the stable set varies due to the satisfaction of the "1-turn condition".

One may note that in obtaining the results of Figure 4.7 use was made of a priori knowledge of the WSB. The goal was not necessarily to find LCS in the 2D search space, but rather to see if the WSB computing using stable sets corresponds to an LCS of the system. This may be seen as a first step in better understanding the problem, but in order to have practical effect, it is more interesting to look at which LCS are found in the 2D search space around the planet.

5 | Computation of Lagrangian Coherent Structures

In the previous chapter, a theoretical background on Lagrangian Coherent Structures was given. The aim of this chapter is to give an explanation on the methodology used for numerically computing the LCS. Along with the explanations of the procedure, intermediate validation results are provided for the Double Gyre: a two-dimensional non-linear system often used as a toy problem in LCS extraction studies.
In Section 5.1 the method for extracting LCS, a description of the algorithm used, and validation results are provided for the FTLE based method. In Section 5.2 the same is done for the Variational Theory based method.

5.1 Finite Time Lyapunov Exponent

In this section the methodology for algorithmically computing LCS from the FTLE method, as well as validation results on the Double Gyre are presented.
The method for computing the Finite Time Lyapunov Exponent (FTLE) directly follows from the theoretical definition given in Chapter 4. The method relies on first obtaining the Cauchy Green Strain Tensor Δ which follows from the Jacobian. The Jacobian can be computed by solving the set of variational equations:

$$\begin{cases} \dot{\mathbf{x}} = \mathbf{f}(\mathbf{x}) & \text{for } \mathbf{x} \in \mathscr{S} \\ \mathbf{x}(t_0) = \mathbf{x}_0 & \text{for } \mathbf{x} \in \mathscr{S} \\ \dot{\Phi} = \mathbf{A}(\mathbf{x}, t)\Phi & \text{for } \mathbf{x} \in \mathscr{S} \\ \Phi(t_0; t_0, \mathbf{x}_0) = \mathbf{I}_n & \text{for } \mathbf{x} \in \mathscr{S} \end{cases} \tag{5.1}$$

The eigenvalues (λ_1, λ_2, with $\lambda_2 > \lambda_1$) and associated eigenvectors (ξ_1, ξ_2) of Φ are computed numerically. As was described in Chapter 4, the FTLE field values are computed using the largest of the eigenvalues, λ_2. In order to increase computational power, use was made of TU Delft's "Eudoxos" machine. This machine allows for the usage of 14 cores. Since the nature of the method relies on computing the FTLE value for each point in the specified grid, independent of other grid

points, the problem is naturally parallelizable. Each point of the grid is sent to one of the cores and the FTLE value is computed.

The pseudo-algorithm explaning the methodology is given as follows:

Algorithm 1: Pseudo algorithm for computing FTLE Field

$\mathscr{G}_0$ is the grid of initial conditions;
$\mathscr{H}_i$ is the subset of $\mathscr{G}_0$ handled by Eudoxos core i;
t_0 and $t_0 + T$ are the initial and final integration time, respectively;
for $\boldsymbol{x}_0 \in H_i$ **do**
    Compute Φ by solving (5.1) on domain $[t_0, t_0 + T]$;
    Compute Cauchy Green Strain Tensor: $\Delta = \Phi^T \Phi$;
    Compute eigenvalues λ_1, λ_2 and eigenvectors ξ_1, ξ_2 of Δ ;
    Compute FTLE value $\sigma_{t_0}^T(\mathbf{x}_0) = \frac{1}{2T} \ln \lambda_2(\Delta)$;
end
Plot $\sigma_{t_0}^T(\mathbf{x}_0)$ for all $\mathbf{x}_0 \in \mathscr{G}_0$;

For validation purposes, Algorithm 1 was executed for the Double Gyre. The Double Gyre system is given by the following equations [7]:

$$\begin{cases} \dot{x} = -A\pi \sin(\pi f(x,t)) \cos(\pi y) \\ \dot{y} = A\pi \cos(\pi f(x,t)) \sin(\pi y) \dfrac{\partial f}{\partial x}(x,t) \end{cases} \tag{5.2}$$

with

$$f(x,t) = a(t)x^2 + b(t)x$$
$$a(t) = \varepsilon \sin(\omega t) \quad b(t) = 1 - 2a(t)$$

To allow for validation, the same parameters were used as in [7]: $A = 0.1$, $\epsilon = 0.1$, $\omega = 2\pi/10$, $t_0 = 0$, $T = 20$, with the phase space being $[0,2] \times [0,1]$. The Python implementation of the variational equations is provided in Appendix A.

The resulting FTLE field for the Double Gyre, as well as a reference result from [7] are shown in Figure 5.1

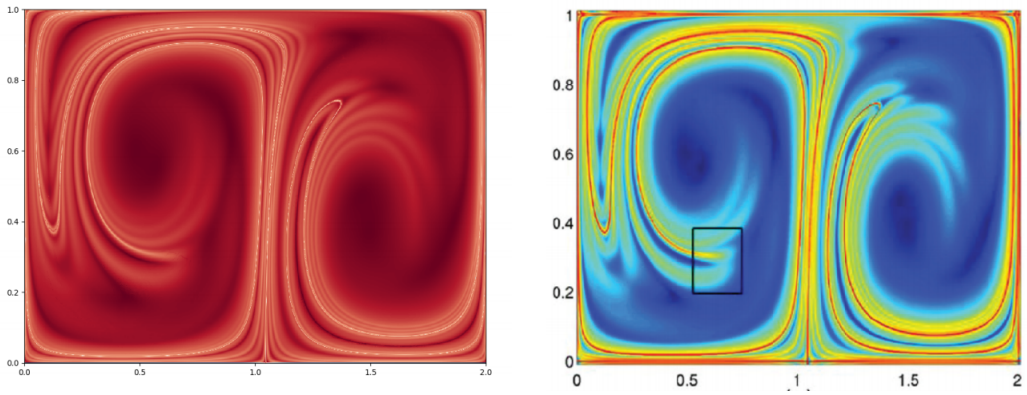

Figure 5.1: FTLE field comparison for Double Gyre. Left: computed with software. Right: Taken from [7]

It is evident from Figure 5.1 that Algorithm 1 works as intented. The resulting FTLE presents a good match to the results found in [7]. Note the presence of the black rectangle in the validation results. This represents a region of degenerate points of the variational theory, and will become clear in the next section. To visually strengthen the intuition that the LCS defined from the FTLE theory can be seen as ridges of the FTLE field, a 3D plot is shown in Figure 5.2.

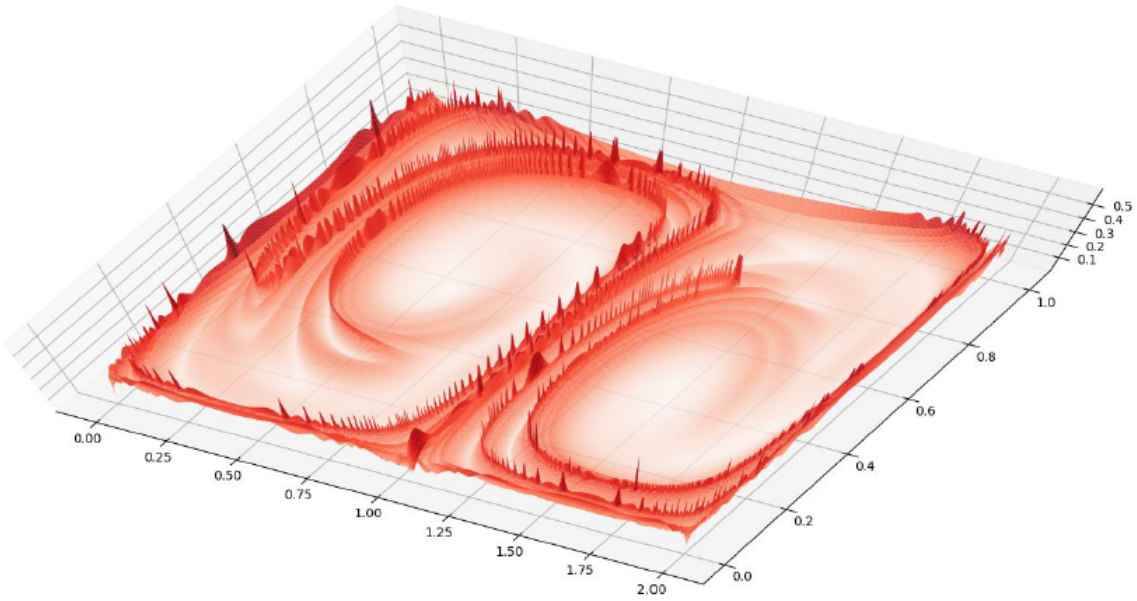

Figure 5.2: 3D view of Double Gyre FTLE field

Following the FTLE field theory, the light parts of the self-computed FTLE Field shown in (a) of Figure 5.1 correspond to the ridges of the field, and therefore the repelling LCS. As was mentioned earlier, research has shown that FTLE fields do not always yield LCS of the overall system. Re-

gardless of this fact, the computation of the field is fast and efficient, and can be used as a first approximation and to provide intuition before proceeding with more complex method. It may also be noted that computing the field for the 1000×500 grid using 14 cores is quite an efficient process on the Eudoxos machine, taking only 20 minutes.

5.2 Variational Theory

In this section the methodology for algorithmically extracting LCS using the variational theory is provided. Moreover, validation results for the toy problem are given.
The method for algorithmically computing LCS from the variational theory is adapted largely from [7], and is based on the theoretical background of the method explained in Chapter 4.
As mentioned earlier, a number of conditions can be formulated that define a repelling LCS within the context of the variational theory:

A material line $\mathscr{M}(t)$ evolving over the interval $[t_0,\ t_0+T]$ is a repelling LCS over this interval, if and only if all the following holds for all initial conditions $\boldsymbol{x}_0 \in \mathscr{M}(t_0)$:

1. $\lambda_1(\mathbf{x}_0) \neq \lambda_2(\mathbf{x}_0) > 1$
2. $\xi_2(\mathbf{x}_0), \nabla^2\lambda_2(\mathbf{x}_0)\,\xi_2(\mathbf{x}_0)\rangle < 0$
3. $\xi_2(\mathbf{x}_0) \perp \mathscr{M}(t_0)$;
4. $\langle \nabla\lambda_2(\mathbf{x}_0), \xi_2(\mathbf{x}_0)\rangle = 0$

where Condition 1 ensures that repulsion is larger than tangential stretch along the LCS, Conditions 3 and 4 guarantee that relative to close material lines the repulsion rate attains a local extremum, and Condition 2 ensures that this extremum is a local maximum [7].

Note that since checking of these conditions follows from many numerical procedures (numerical solving of ODE, numerical differentiation, and eigenvalue solving), it is an inherently unstable pursuit. To allow for more robust numerical implementation, the conditions are reformulated by making use of the following properties [7]:

- Condition 4 turns out to be a necessary condition with respect to locally normal translations in the direction of ξ_2. This follows from the proof of Theorem 1 in [9]. This is described mathematically as follows:

$$\frac{d}{d\varepsilon}\rho_{t_0}^{t}(\mathbf{x}_0+\varepsilon\xi_2,\xi_2)|_{\varepsilon=0} = \frac{1}{2\sqrt{\lambda_2(\mathbf{x}_0)}}\langle\nabla\lambda_2(\mathbf{x}_0), \xi_2(\mathbf{x}_0)\rangle = 0 \tag{5.3}$$

  which does indeed turn out to be the same as Condition 4. Moreover, the repulsion rate $\rho_{t_0}^{t}(\mathbf{x}_0,\xi_2(\mathbf{x}_0)) = \sqrt{\lambda_2(\mathbf{x}_0)}$, which allows the relaxation of Condition 4 to require that the average value of λ_2 along $\mathscr{M}(t_0)$ need be the largest among nearby curves normal to the vector field $\xi_2(\mathbf{x}_0)$.

- Condition 2 is altered from a strict inequality, to one that allows equality. LCS are therefore allowed to have finite thickness, but require a uniquely defined local orientation.
- Condition 3 is altered based on the geometry of ξ_1 and ξ_2. Since these eigenvectors are already computed when solving the variational equations, the fact that they are orthogonal means that they can be used to efficiently implement condition 3.

After implementing the changes mentioned above, the necessary conditions (1-4) can be reformulated as follows:

(A) $\lambda_1(\mathbf{x}_0) \neq \lambda_2(\mathbf{x}_0) > 1$
(B) $\left\langle \xi_2(\mathbf{x}_0), \nabla^2 \lambda_2(\mathbf{x}_0)\, \xi_2(\mathbf{x}_0) \right\rangle \leq 0$
(C) $\xi_1(\mathbf{x}_0) \parallel \mathscr{M}(t_0)$
(D) $\lambda_2(\gamma)$, the average of λ_2 over a curve γ, is maximal on $\mathscr{M}(t_0)$ among all nearby curves γ satisfying $\gamma \parallel \xi_1(\mathbf{x}_0)$

Reformulated Condition (C) requires that LCS be tangent to the $\xi_1(\mathbf{x}_0)$ vector field, with ξ_1 being the eigenvector corresponding to the smallest eigenvalue λ_1. Following the definition of [7], all lines tangent to the $\xi_1(\mathbf{x}_0)$ vector field are hereby defined as *strainlines*. By definition, it is therefore possible to state that strainlines are smooth trajectories of the following ODE:

$$\mathbf{r}' = \xi_1(\mathbf{r}), \qquad |\xi_1(\mathbf{r})| = 1 \tag{5.4}$$

This ODE does, however, not yield a set of globally smooth strainlines, which is a requirement for LCS. The ODE is therefore altered by reformulating the right hand side of (5.4) as follows:

$$\mathbf{r}'(s) = \mathbf{f}\big(\mathbf{r}(s), \mathbf{r}'(s-\Delta)\big) = \operatorname{sign}\left\langle \xi_1(\mathbf{r}(s)), \mathbf{r}'(s-\Delta) \right\rangle \alpha(\mathbf{r}(s)) \xi_1(\mathbf{r}(s)) \tag{5.5}$$

where Δ is the numerical step size, and the scalar field $\alpha(\mathbf{x}_0)$ is given by:

$$\alpha(\mathbf{x}_0) = \left(\frac{\lambda_2(\mathbf{x}_0) - \lambda_1(\mathbf{x}_0)}{\lambda_2(\mathbf{x}_0) + \lambda_1(\mathbf{x}_0)} \right)^2$$

This scaling factor vanishes at degenerate points where $\lambda_1 = \lambda_2$, thus immediately satisfying condition (A). The term $\operatorname{sign}\xi_1(\mathbf{r}(s))$ locally reverses the orientation of the vector field $\xi_1(\mathbf{r})$ along the strainline for smooth integration in case discontinuities are present [7]. In practice, this is achieved by rotating the vector ξ_1 to have the same direction as the solution computed in the previous timestep.

Note that solutions to the reformulated ODE (5.5) are strainlines that satisfy Conditions (A) and (C). Strainlines resulting from this ODE that also satisfy conditions (B) and (D) can therefore be classified as repelling LCS. Note that condition (B) has to be satisfied on each point along the

strainline, including the initial point specified by the user-defined grid. It is therefore computationally more efficient to first check condition (B) for each point in the grid $\mathscr{G}_0$, and initialize ODE integration only from those points in subset $\mathscr{U}_0 \in \mathscr{G}_0$ satistfying condition (B). Comparisons for this region are shown in Figure 5.3. Note that for our procedure, a similar grid with a total of 500K points is used as in the reference paper [7]. This is achievable due to the usage of 14 cores on the Eudoxos machine. This was not possible in previous reproduction studies such as [18], where a grid of (200×50) was used.

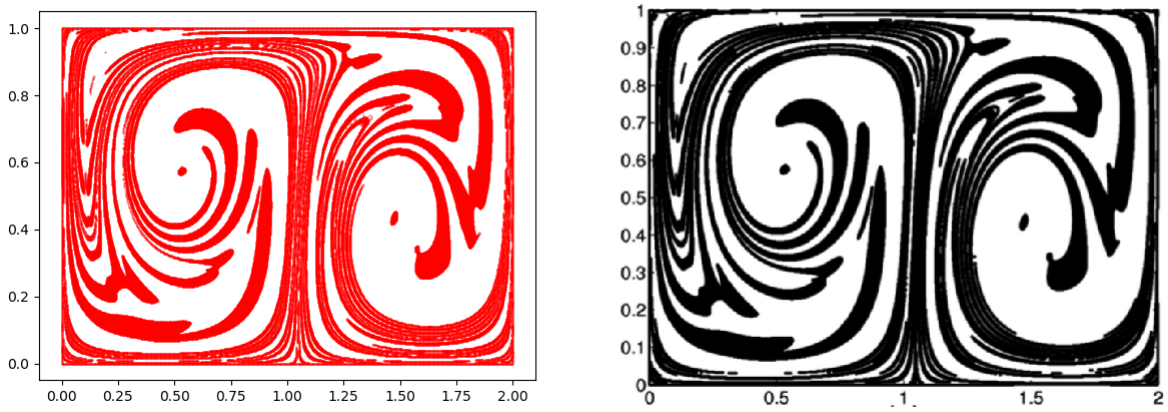

Figure 5.3: Region $\mathscr{U}_0$ comparison for Double Gyre. Left: computed with software. Right: taken from [7]. Both computations are done on a 1000×500 grid.

It is evident from Figure 5.3 that the resulting region $\mathscr{U}_0$ is very similar to the one from [7], but some minor differences still exist. This can be attributed to the many numerical approximations that are performed in the procedure. As was mentioned in [18], the region $\mathscr{U}_0$ is the result of an ODE integration for which tolerance settings and integrator choice can have an effect on the outcome. Also, the computation of the Hessian is done by central finite differencing. The off-diagonal terms are computed using (5.6). For the diagonal terms (5.7) is used. [1]

$$H_{xy}(x,y) \approx \frac{f(x+\epsilon,y+\epsilon) - f(x+\epsilon,y-\epsilon) - f(x-\epsilon,y+\epsilon) + f(x-\epsilon,y-\epsilon)}{4\epsilon^2} \tag{5.6}$$

$$H_{xx}(x,y) \approx \frac{f(x+\epsilon,y) - 2f(x,y) + f(x-\epsilon,y)}{\epsilon^2} \tag{5.7}$$

Note the dependancy of the Hessian on the perturbation parameter ϵ used. Because the step involving computation of the Hessian is crucial for LCS extraction, choosing a value of ϵ must be done carefully. This is especially the case for a highly nonlinear and sensitive problem such as the double gyre. For the result in Figure 5.3, a perturbation value of $\epsilon = 10^{-5}$ is used.
To further reduce reduntant computations within the set, the points in region $\mathscr{U}_0$ are intersected

[1] `https://v8doc.sas.com/sashtml/ormp/chap5/sect28.htm`

with four horizontal and four vertical lines, resulting in subset $\mathscr{L}_0 \in \mathscr{U}_0$. For the authors of [7], this reduces the amount of initial conditions from $\mathscr{U}_0$ to $\mathscr{L}_0$ by a factor of 96. For our grid settings, a similar factor of 95 is found. A comparison of the resulting regions $\mathscr{L}_0$ is shown in Figure 5.4.

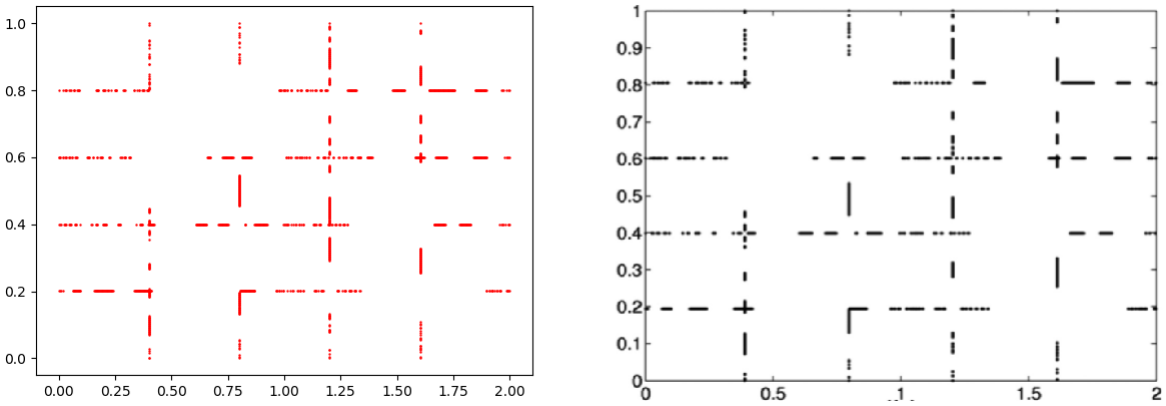

Figure 5.4: Region $\mathscr{L}_0$ comparison for Double Gyre. Left: computed with software. Right: taken from [7]

In principle, System (5.5) can be integrated (both forward and backward) from all initial conditions in $\mathscr{L}_0$ until each strainline reaches the boundary of the specified domain, or until a fixed point is found (in which case the integration will naturally stop due to the scaling factor α).
It must be noted that in most cases, strainlines will not fully be classified as LCS. Instead, merely a part of the strainline will be classified as such. This means that along each point of the strainline condition (B) needs to be verified to continue the integration process. Due to the numerical sensitivity involved in checking condition (B) (i.e: numerical estimation of the Hessian of the $\lambda_2(\mathbf{x}_0)$ scalar field), it may be possible that along the strainline, points are erroneously considered not to satisfy condition (B). To prevent the algorithm from prematurely terminating the integration, a pre-set length ℓ_f is defined. This is a distance over which a strainline is allowed to repeatedly fail in satisfying condition (B), without terminating the integration. In the reference work, as well as in this work, a value of $\ell_f = 0.2$ is used.

Having identified strainlines segments that satisfy conditions (A), (B), and (C), all that remains is to filter on condition (D), and find the segments that are local maximizers of λ_2. Before doing so, segments are filtered on a minimum length parameter ℓ_{min}, to ensure LCS to have sufficient length.
As was mentioned earlier, the original Condition 4 was reformulated to condition (D) based on the fact that locally normal translations in the direction of ξ_2 can be used in the process of checking for local λ_2 maximizers. Based on this notion, two curves tangent to the strainline segment γ consisting of $\mathbf{x}$ (γ^+ and γ^-) are constructed as follows, based on [18]:

$$\begin{aligned}\gamma^+(t_0) &:= \left\{\mathbf{x}_0^+, \cdots, \mathbf{x}_{\text{final}}^+\right\}, \quad \text{where } \mathbf{x}_i^+ = \mathbf{x}_i + \delta\boldsymbol{\xi}_2 \\ \gamma^-(t_0) &:= \left\{\mathbf{x}_0^-, \cdots, \mathbf{x}_{\text{final}}^-\right\}, \quad \text{where } \mathbf{x}_i^- = \mathbf{x}_i - \delta\boldsymbol{\xi}_2\end{aligned} \tag{5.8}$$

Note that the value of δ is an arbitrary choice, and may require tuning for the problem at hand. For the Double Gyre example, a value of $\delta = 0.02$ is used. Note that in the reference works no mention of this value is given. As was done in [18], for each of the three curves the average values of the λ_2 field are calculated as follows:

$$\bar{\lambda}_2(\gamma) \approx \frac{\sum_{i=1}^{i=\text{final}} \lambda_2(\mathbf{x}_i) \cdot \|\mathbf{x}_{i-1} - \mathbf{x}_i\|}{\sum_{i=1}^{i=\text{final}} \|\mathbf{x}_{i-1} - \mathbf{x}_i\|} \tag{5.9}$$

which serves as a numerical approximation for the average of the field over a curve.

It is of importance to note that the computation of the λ_2 parameter following (5.9) has to be done with caution. The quality of the approximation used to compute the average λ_2 value using (5.9) is highly dependent on the variation in the λ_2-field. If the λ_2-field is highly sensitive to small perturbations in evaluation points, the resulting average value computed by the approxomation may not be accurate. More specifically: the difference between $\lambda_2(\mathbf{x}_i)$ and $\lambda_2(\mathbf{x}_{i-1})$ may be so large that the numerator in (5.9) is no longer an accurate approximation for the "weighted" value of λ_2 on point $\mathbf{x}_i$. This will have an effect on the final filtering of LCS candidates to LCS, and therefore lead to wrong results. This problem is countered by introducing an interpolation method to increase the resolution of the strainline. The method is highlighted as follows:

1. Between each pair $(\mathbf{x}_i, \lambda_i)$ and $(\mathbf{x}_{i+1}, \lambda_{i+1})$, perform linear interpolation on a grid consisting of $\mathscr{F}$ evenly spaced points between $\mathbf{x}_i$ and $\mathbf{x}_{i+1}$.

2. Feed new strainline resulting from interpolation, with $\mathscr{F}$ more points than the original strainline, into the procedure for calculating local λ_2 maximizers according to (5.9).

In this method of increasing the resolution of the strainline, the factor $\mathscr{F}$ has to be chosen. A higher value is desirable in terms of accuracy of (5.9), but comes at a considerable cost in terms of computational time because for each point in the new strainline, consisting of $\mathscr{F}$ more points, the λ_2 field is evaluated. This is a time consuming process in which the inner ODE of the variational equations is solved.
In order to find a suitable value of $\mathscr{F}$ a parameter β is defined, which represents the mean percentage deviation between the λ_2 values of two consecutive points $\mathbf{x}_i$ and $\mathbf{x}_{i+1}$ on a strainline. This value β can be seen as a measure for the point-wise sensitivity of a strainline in a λ_2 field. For the Double Gyre, the value of β is plotted against varying values of $\mathscr{F}$. This is done for the 4 strainlines in the Double Gyre system, as shown in Figure 5.5.

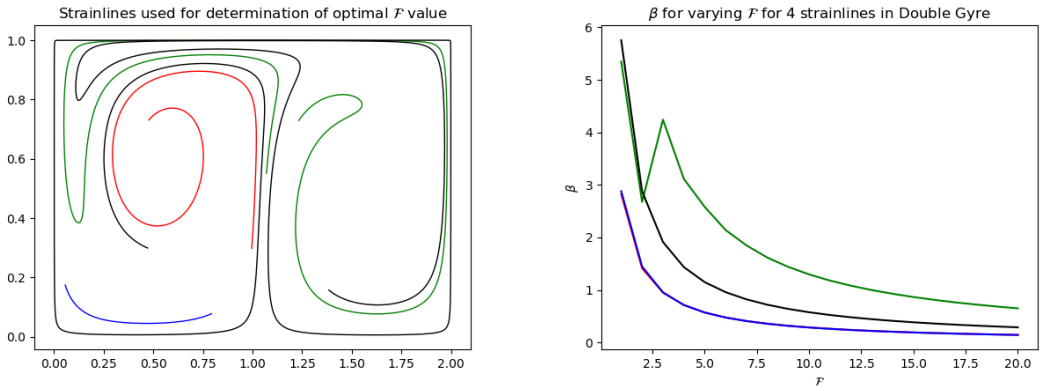

Figure 5.5: Determination of optimal $\mathscr{F}$ value for Double Gyre. Left: strainlines used for comparison. Right: $\beta - \mathscr{F}$ plot

Note that the 4 lines shown in Figure 5.5 are chosen carefully to ensure that they span a sufficient area of the domain on which the Double Gyre is defined. This is done to make sure that the final value chosen for $\mathscr{F}$ is yields sufficient β values for every strainline, rather than satisfying results for a small region in the domain.

From Figure 5.5 it can be seen that as expected, increasing values of $\mathscr{F}$ in general lead to smaller values in β. By looking at the curve, it seems that a value of $\mathscr{F} = 10$ seems optimal. This is where the curves tend to become more flat, and further gains seem marginal. However, when taking computation time into account, a value of $\mathscr{F} = 5$ is chosen, as it seems to give β values close to 1% and does not make computing times too excessive. For reference, going from strainlines to LCS with $\mathscr{F} = 1$ on the 1000×500 grid takes around 1 hour on 14 Eudoxos cores. For a value of $\mathscr{F} = 5$ this computation takes 7 hours. Selecting higher values of $\mathscr{F}$ is infeasible for this work. In future work it may be desirable to look into results for very high values of $\mathscr{F}$, if computational time is less of a constraint.

Having computed the average value of λ_2 for the segment, condition (D) is deemed satisfied if the average value $\bar{\lambda}_2(\gamma)$ is larger that of its neighbours $\bar{\lambda}_2(\gamma^+)$ and $\bar{\lambda}_2(\gamma^-)$, and resulting strainlines are classified as repelling LCS of the system. Resulting longest repelling LCS and the comparison with [7] for the Double Gyre are shown in Figure 5.6.

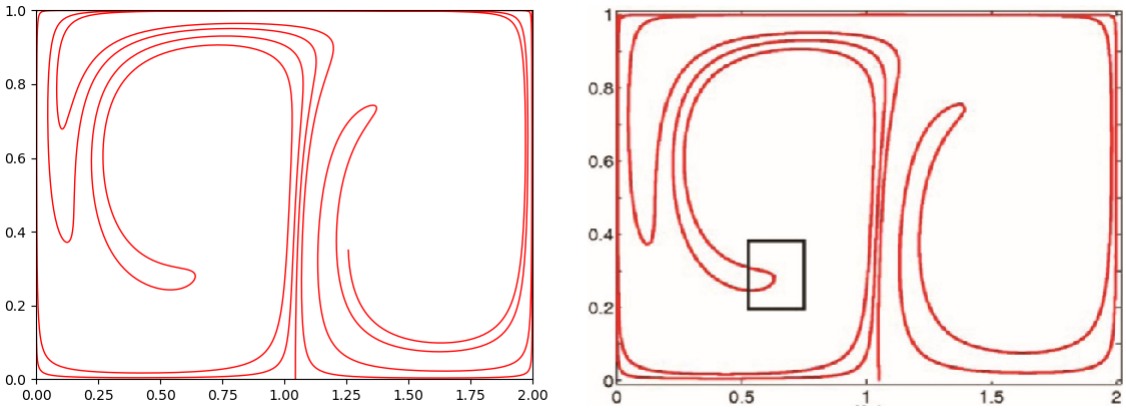

Figure 5.6: Resulting LCS comparison for Double Gyre. Left: Longest LCS computed with software. Right: taken from [7]

Note that in Figure 5.6 the *longest* LCS is plotted and compared with the result from [7]. For completeness sake, a comparison of *all* LCS is given with the result from [18] in Figure 5.7.

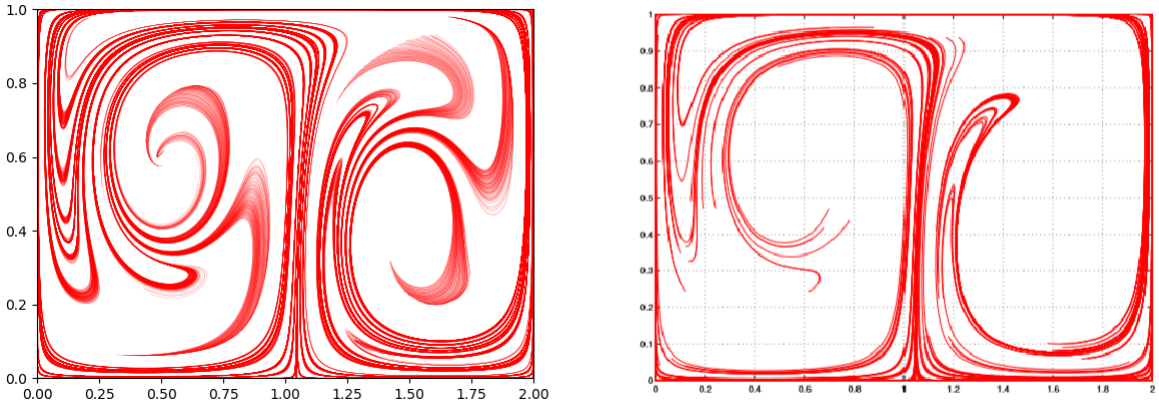

Figure 5.7: Resulting LCS comparison for Double Gyre. Left: All LCS computed with software, 500K initial conditions. Right: LCS taken from [18], 10K initial conditions

From Figures 5.6 and 5.7 the following can be noted:

- The usage of a finer grid (500K points versus 10K points) leads to more lines being classified as LCS, which is as expected. It also shows that grid choice is an important parameter in performing this analysis, as LCS of the system may be missed if insufficient number of initial conditions are used. This further strengthens the argument for making use of parallel processing when carrying out LCS extraction using the variational theory.
- In the right plot of Figure 5.7 it can be seen that the strainlines seem unfinished. This has to do with the fact that a pre-defined maximum length for the strainlines was used in [18].

In our software, no pre-set length is used as input, and the strainlines are integrated until they reach the boundary of the domain, or integration stops naturally by encountering degenerate points.

- In [18] no use is made of an interpolation routine to increase resolution of the strainline. This may, however, not have been necessary as MATLAB's ODE solver (used in [18]) might return more values by default. It is not mentioned what the resolution of the strainlines is, and differences might be attributed to this difference in strainline resolution and therefore final filtering on condition (D).
- Similar to the strainline resolution, it is unclear what value is used in [18] for δ. This is an arbitrary parameter defining the neighbourhood of a strainline, and is expected to have a significant effect on filtering on condition (D).
- The final comparison with the reference work [7] shown in Figure 5.6 shows a close but not a perfect match. Also, the authors of the paper mention that they found the single strainline that classifies as LCS, which was not the case using the software developed in this work. Interestingly, the *longest* LCS that is found using the software does match well with the results in [7].

It can be concluded that while differences in result are present, the overall shape of the LCS seems similar. Differences may be attributed to numerical noise, and differences in critical parameter settings. It is therefore recommended that in future work, values for these critical parameters are documented allowing for more robust comparisons.
The full algorithm for finding LCS based on the variational theory described in [7] is given in Algorithm 2.

Algorithm 2: Algorithm for extracting LCS based on variational theory

$\mathscr{G}_0$ is the grid of initial conditions;
$\mathscr{U}_0$ is the subset of $\mathscr{G}_0$ satisfying condition (B);
$\mathscr{L}_0$ is the subset of $\mathscr{U}_0$ intersecting with eight straight lines;
$\mathscr{H}_i$ is the subset of $\mathscr{L}_0$ handled by Eudoxos core i;
t_0 and $t_0 + T$ are the initial and final integration time, respectively;
ode is an ode solver which returns the next point $\mathbf{x}_j$;
for $x_0 \in \mathscr{H}_i$ **do**
    while $L < \ell_f$ **do**
        Compute Φ by solving (5.1) on domain $[t_0, t_0 + T]$;
        Compute Cauchy Green Strain Tensor: $\Delta = \Phi^T \Phi$;
        Compute eigenvalues λ_1, λ_2 and eigenvectors ξ_1, ξ_2 of Δ ;
        $\mathbf{x}_{j+1} = \mathbf{ode}(\text{sign}\langle \xi_1(\mathbf{r}(s)), \mathbf{r}'(s-\Delta)\rangle \, \alpha(\mathbf{r}(s))\xi_1(\mathbf{r}(s)))$;
        if x_{j+1} *satisfies* B **then**
            $L = 0$;
        else
            $L = L + \left\| \mathbf{x}_{j+1} - \mathbf{x}_j \right\|$;
        end
    end
    if $L > \ell_f$ **then**
        Too many failures, segment is not LCS;
    else
        if $L < \ell_{min}$ **then**
            Too short, segment is not LCS;
        else
            Interpolate segment with factor $\mathscr{F}$;
            $\gamma^+ := \{\mathbf{x}_0^+, \cdots, \mathbf{x}_{\text{final}}^+\}$, where $\mathbf{x}_i^+ = \mathbf{x}_i + \delta\boldsymbol{\xi}_2$
            $\gamma^- := \{\mathbf{x}_0^-, \cdots, \mathbf{x}_{\text{final}}^-\}$, where $\mathbf{x}_i^- = \mathbf{x}_i - \delta\boldsymbol{\xi}_2$;
            $\bar{\lambda_2}(\gamma) := \text{int}\left(\lambda_2\left(\gamma\left(t_0\right)\right) / \text{length}\left(\gamma\left(t_0\right)\right)\right.$
            $\bar{\lambda_2}(\gamma)^+ := \text{int}\left(\lambda_2\left(\gamma^+\left(t_0\right)\right) / \text{length}\left(\gamma^+\left(t_0\right)\right)\right.$;
            $\bar{\lambda_2}(\gamma)^- := \text{int}\left(\lambda_2\left(\gamma^-\left(t_0\right)\right) / \text{length}\left(\gamma^-\left(t_0\right)\right)\right.$
            if $\bar{\lambda_2}(\gamma) > \bar{\lambda_2}(\gamma)^+$ *and* $\bar{\lambda_2}(\gamma) > \bar{\lambda_2}(\gamma)^-$ **then**
                Segment is an LCS;
            else
                Segment does not satisfy (D), and is not an LCS;
            end
        end
    end
end

6 | Application of LCS software to ERTBP

In the previous chapter two methods for developing the software to extract LCS from a dynamical system were explained. Furthermore, validation results were provided along the way to ensure that the software functions correctly. In this chapter, the developed software will be applied to the Elliptic Restricted Three Body Problem (ERTBP) in order to answer the main questions that preceded this research:

- Without using a priori knowledge of the WSB, do LCS in the 2D search space around a planet yield WSB?
- How does the Weak Stability Boundary react to a change in integration time, corresponding to the time needed for a particle according to the stability criterion?
- How do the computed LCS for the system relate to WSB corresponding to stable points defined for different number of revolutions n?
- Can the application of LCS to the computation of Weak Stability Boundaries yield more efficient computation compared to the traditional method of stable set manipulation?

These questions will be answered mainly by application of the variational theory to the ERTBP, since it has been shown that this is a more reliable method of extracting LCS. However, for completeness sake, and to get an initial idea of how LCS in the ERTBP might manifest, some results on FTLE application are given first.

6.1 Finite Time Lyapunov Exponent application to ERTBP

In this section the FTLE algorithm (Algorithm 1) developed in the previous section is applied to the ERTBP. The ERTBP configurations used are that of the Sun–Mars system with the following parameters:

Table 6.1: ERTBP configuration settings used for the Sun–Mars case

Variable	Symbol	Value
Sun mass	m_1	$1.989 \cdot 10^{30}$ kg
Mars mass	m_2	$6.417 \cdot 10^{23}$ kg
Sun–Mars system eccentricity	e_p	0.093418
P_3 orbit eccentricity	e	0.90
Initial true anomaly	f_0	0

The stable set $\mathcal{W}_1$ for the corresponding problem is shown in Figure 6.1. Note that this stable set is generated outside this work, and is obtained from [11].

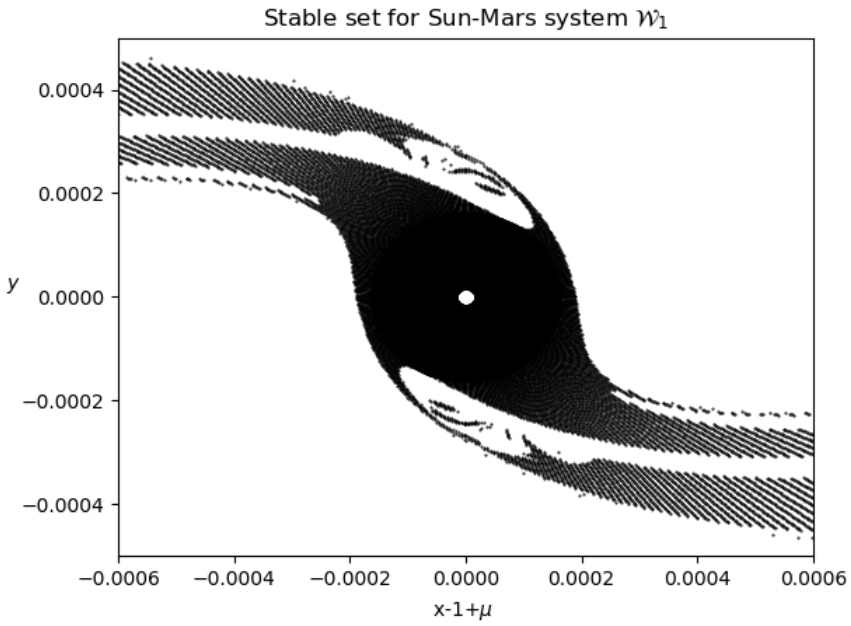

Figure 6.1: Region $\mathcal{W}_1$ for Sun–Mars system with parameters shown in Tabel 6.3

FTLE results for the problem using six values of f_{final} are displyayed in Figure 6.2. Note that in the procedure, the value of f_{final} is used as T.

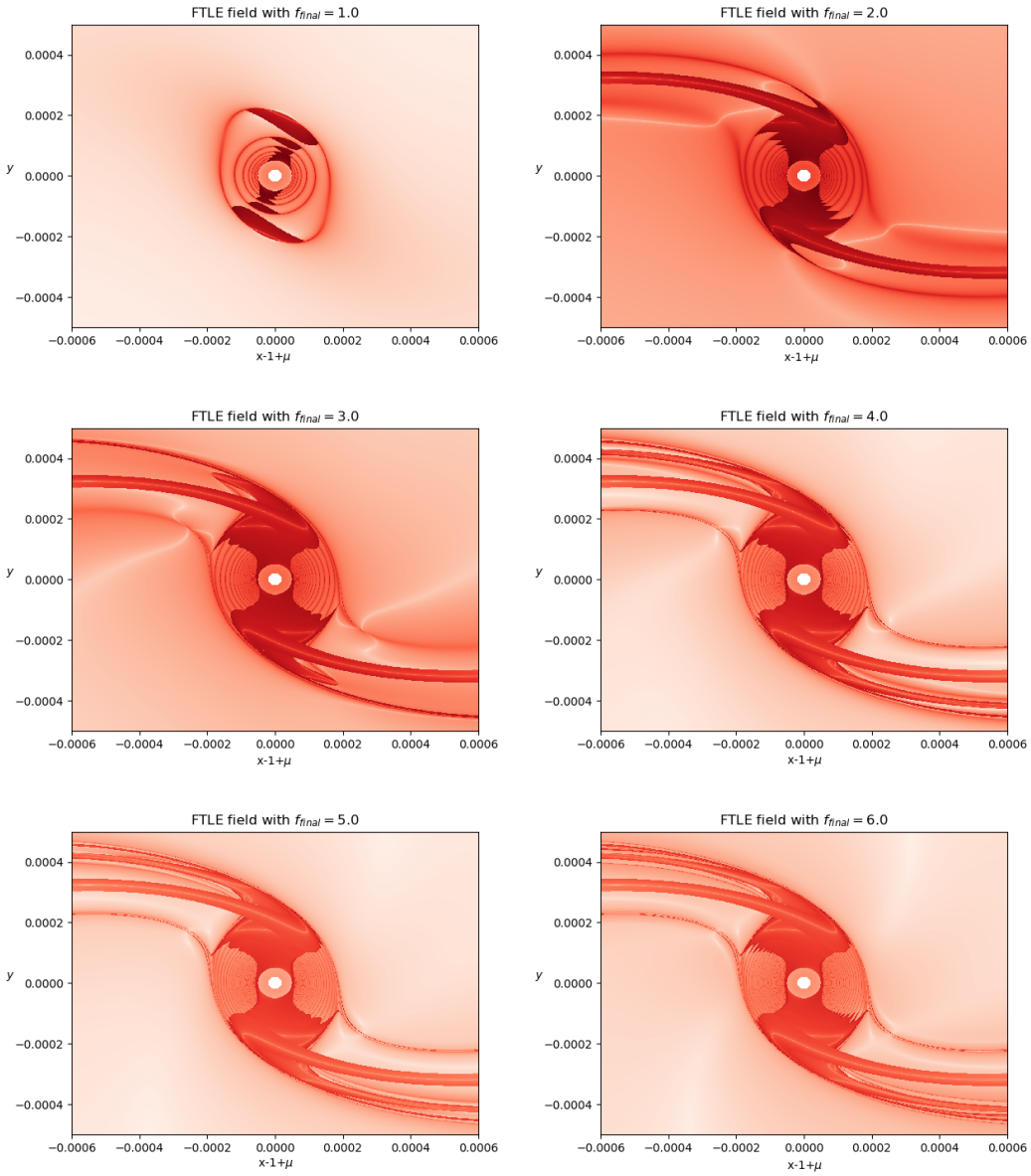

Figure 6.2: FTLE field for ERTBP, using six values of f_{final} on a (1000 × 1000) grid

From Figure 6.2 it immediately becomes clear how similar the FTLE field looks to the stable set $\mathcal{W}_1$. This is particularly the case for large f_{final} values. The largest change occurs between values of 1.0 and 2.0, after which only small details are changed. It can also be noted that while the general shape of the field resembles that of $\mathcal{W}_1$, small details inside the black region are not displayed.

Computation of each FTLE field using parallel processing on 14 cores takes around 2 hours. We may conclude that computing FTLE fields proves to be an efficient and reliable way of getting an idea of the shape of $\mathcal{W}_1$, but is not able to capture details inside the WSB. For this, the variational

theory might be more suitable. This will be explored in the next section.

6.2 Variational Theory application to ERTBP

As was explained earlier, existing work on applying variational theory of LCS to the ERTBP, and comparing it with the WSB from stable sets was done in [18]. In this section, those ideas are explored further and an attempt is made to answer the research question posed for this work.

6.2.1 Adaptation to ERTBP

Due to the more complex nature of the ERTBP compared to the Double Gyre, a number of adaptations had to be made to the variational LCS extracting software. Two main adaptations are summarized below:

- **Usage of different integrator:** As was mentioned in Section 4.5, the procedure of integrating the ERTBP equations of motion consists of a number of sequential coordinate transformations. These coordinate transformations, combined with the (by nature) more non-linear behaviour of the ERTBP compared to the Double Gyre, make the problem at hand more difficult to solve for numerically. To ensure that this is done in a robust way, the inner ODE (which solves the variational equations) makes use of the LSODA integrator [17]. This integrator switches automatically between the nonstiff Adams method and the stiff BDF method [5]. It is considered more robust for problems such as the ERTBP with the characteristics described above.

- **Usage of events to stop integration:** In the double-gyre example, strainlines were integrated until they either reach the boundary of the domain, or reach degenerate points (and the integration stops naturally). In the ERTBP problem an extra stopping criterion has to be included. Because values of r are naturally small (order 10^{-4}), while stepping over the ODE solver or computing the Hessian, computations may be required at r values which are too small to handle. For example, terms like r^{-5} in the variational equations might lead to overflow errors. To handle this, the ODE solvers (both for the inner and outer ODE) are stopped when r values to evaluated are less than 10^{-5}. In future work, it may be desirable to switch to regularized equations of motion to continue evaluations in the ODE solving process, for example by making use of Levi Civita regularization [14].

6.2.2 Validation

As a form of validation, before answering the research questions stated above, an effort was made to reproduce the results obtained by [18] using the developed software. Results of this comparison are given in Figure 6.3. For these results, use was made of the stable sets computed by the authors of [11]. The reference dataset used is that of the Sun–Mars system with the following parameters:

Furthermore, the values for the initial conditions for the comparison figure are given by the following:

Table 6.2: Initial conditions used for verification with stable set and [18]. IC1 and IC2 refer to the right and left initial conditions, respectively.

Variable	Symbol	Value
Initial distance IC1-P2	r_1	1.882295326
Initial angle IC1	θ_1	0
Final integration time IC1	f_{final1}	2.9332364420
Initial distance IC2-P2	r_2	1.882295326
Initial angle IC2	θ_2	π
Final integration time IC2	f_{final2}	2.4847866565

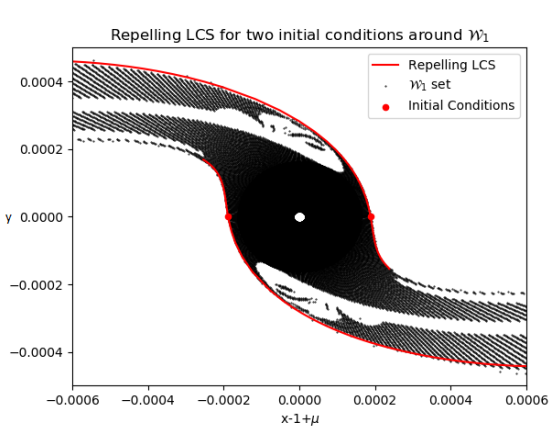

(a) Repelling LCS from software

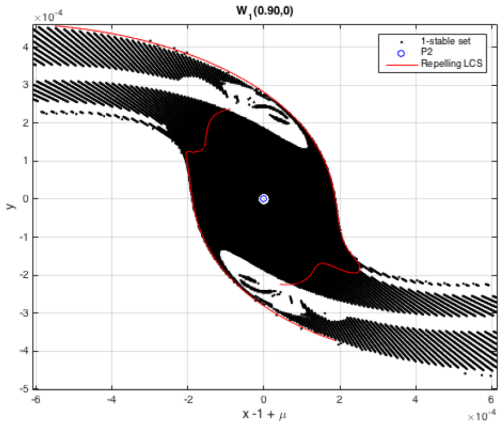

(b) Repelling LCS from [18]

Figure 6.3: Comparison of software and [18] for $\mathcal{W}_1$ stable set.

From Figure 6.3 it can be seen that the software-generated repelling LCS is able to follow the edge of the WSB, but seems to not be able to trace it fully. One thing to note is that in [18] two 'blobs' were found on the repelling LCS which did not follow the WSB and were considered malfunctions of the software. In our software, the integration seems to terminate when encountering this region, thus not giving erroneous results. This may be attributed to the fact that in our software a stopping criterion of Δt_{min} is specified, which is the minimum step size allowed for the outer strainline integration to take. When the next step is taken to be smaller than this, it means that the integrator reaches an area that is highly sensitive and most likely would lead to errors when continuing the integration. In [18] such controls were not present, which may explain the difference in results.

6.2.3 Determination of $\mathscr{F}$ for ERTBP

Because the strainlines shown in Figure 6.3 both seem to span different parts of the search space, both of these strainlines are used to compute the $\mathscr{F}$ parameter. This is done in a similar fashion as was done for the Double Gyre. Because of the more sensitive nature of the λ_2 field for the ERTBP, both mean and median values are computed for the consecutive percentage difference in λ_2 value along the strainlines. This is done for both the regular (interpolated) strainline, and the interpolated strainline with outliers removed. Results for this analysis are shown in Figure 6.4.

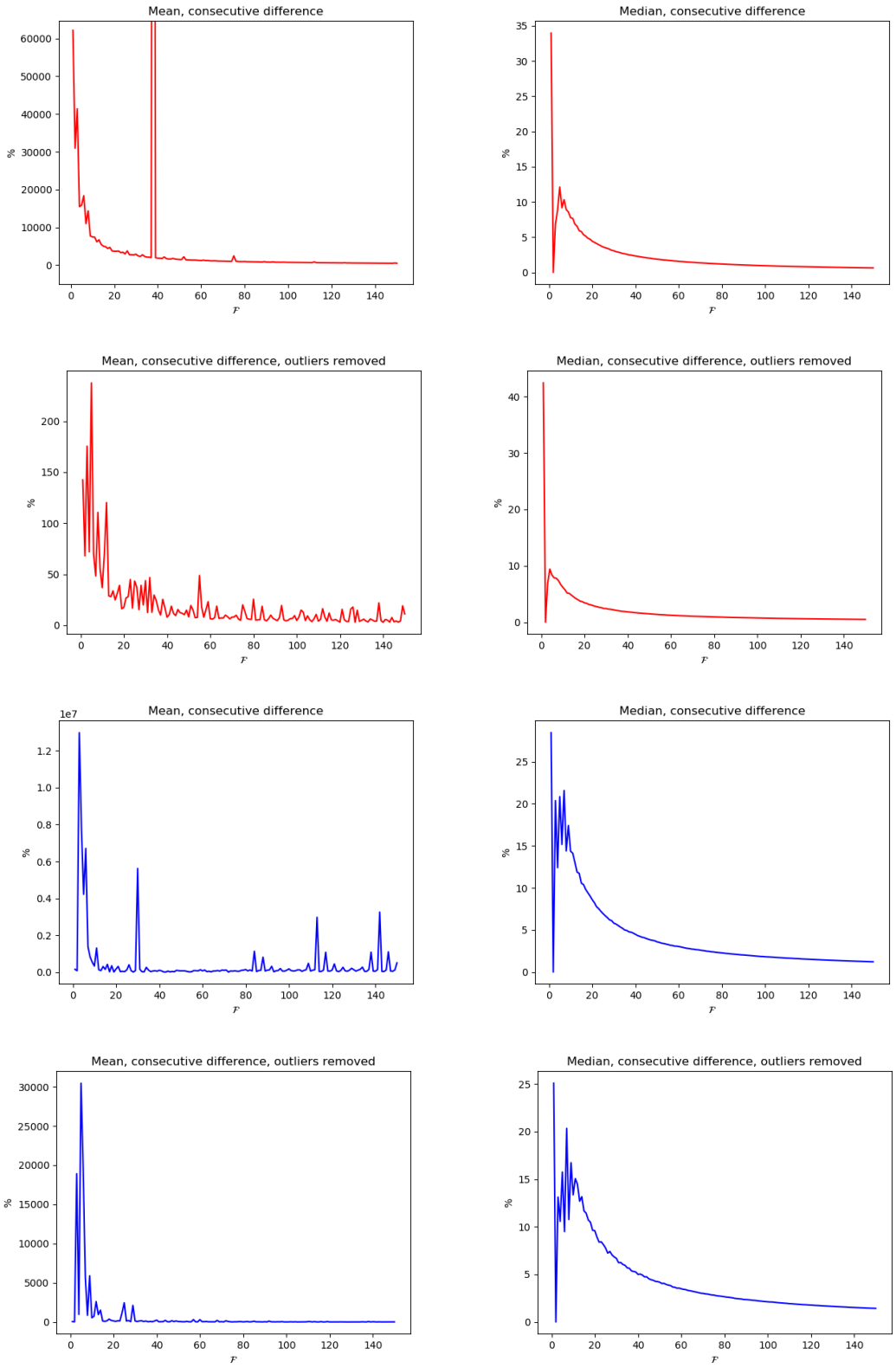

Figure 6.4: Determination of $\mathcal{F}$ parameter for ERTBP. Red and blue correspond to strainlines from IC_1 and IC_2, respectively.

A number of things can be noted from Figure 6.4. Firstly, the λ_2 field for the problem is extremely sensitive. If outliers on the strainlines are not removed, mean consecutive difference values for extremely high $\mathscr{F}$ values such as 150, are still 40% and 200% for strainlines from IC_1 and IC_2, respectively. Furthermore, the sensitivity can be seen by the spiky nature of the statistics. When outliers on the strainlines are removed, the plots still seem to contain some spikes, but it is certainly less than for the regular strainlines. Increasing the value of $\mathscr{F}$ also seems to make the lines more smooth. The following can be concluded:

- The ERTBP λ_2 field is extremely sensitive. Especially when comparing to the Double Gyre example shown earlier.
- By looking at the figures, one might argue that including an outlier removal strategy for this problem might be desirable. That is, by removing points with outlying λ_2 values on a strainline, we may get accurate λ_2 comparisons. This is not possible because the outlier removal (using a modified Z-score with threshold 2.0) removes around 40% of the points on the line. It is deemed that this would leave too little information on a strainline to be of use. In future work, it may be desirable to tweak the threshold value of the outlier removing strategy and balance the number of outliers with accuracy. For this work, no outlier strategy is employed.
- Similar to the case for the Double Gyre, the median and mean differences decrease as $\mathscr{F}$ is increased. This is particularly the case for the outlier removed cases. Because the strainlines are close together, the areas which provide large outliers might be present for both the original strainline and its neighbours. Because we are not interested in the value of λ_2 per se, but rather the sign of the difference between the average λ_2 values on the lines, it may not be necessary to perform interpolation. A further analysis will be done later in this work to explore this idea. To balance computational time with accuracy, a value of $\mathscr{F} = 50$ will be chosen for this analysis.

6.2.4 Effect of variation in integration time on repelling LCS

One of the aims of this research was to gain insight into the effect of the integration time parameter on the repelling LCS of the system. For clarity purposes, this analysis is done for the same problem used in the comparison in Figure 6.3.

Varying integration time for entire system

The effect of variation in the integration time parameter on the strainlines originating from the two initial conditions IC_1 (red line) and IC_2 (blue line) is shown in Figure 6.5.

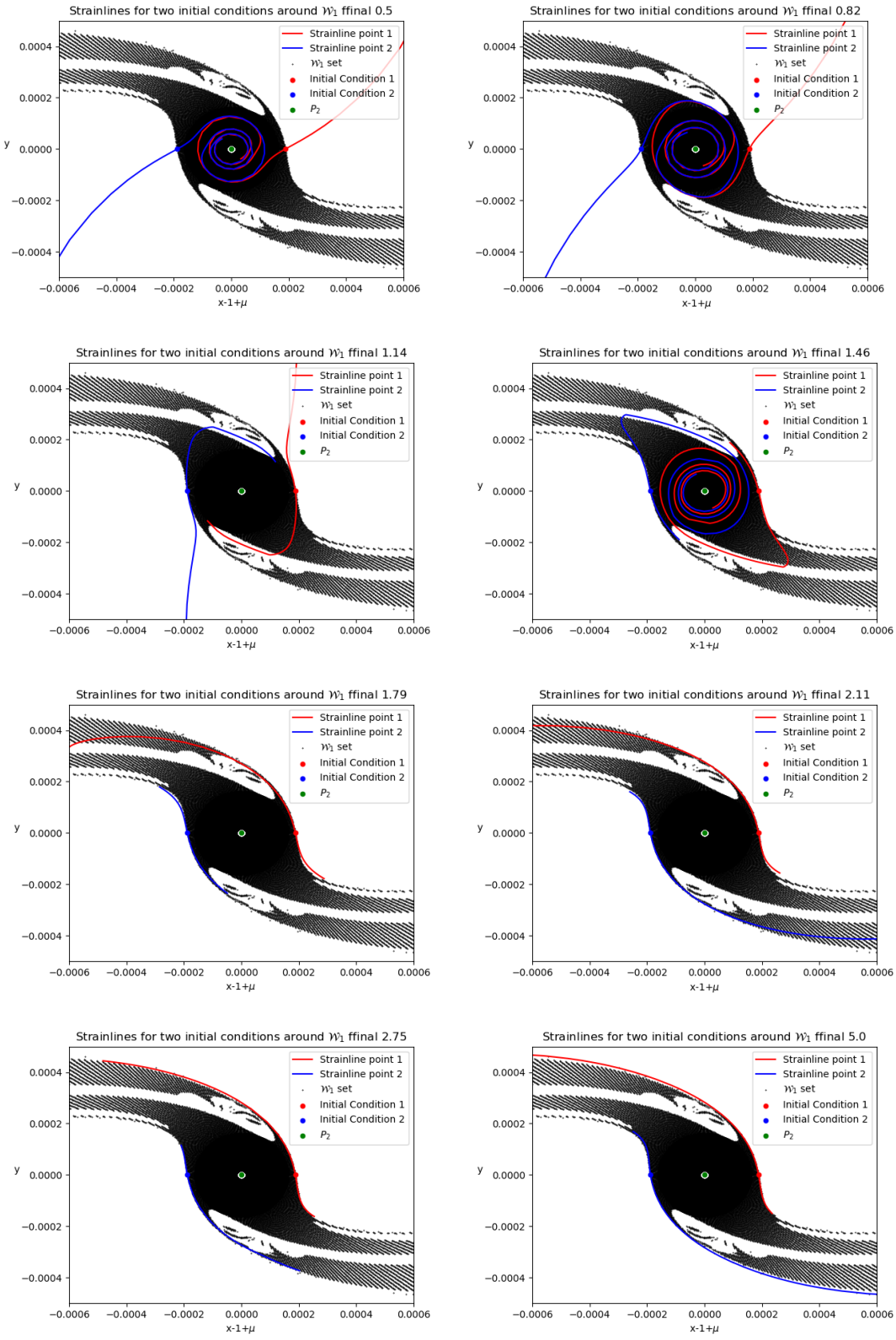

Figure 6.5: Effect of varying integration time on strainlines

From Figure 6.5 it becomes evident that small integration times lead to no match with the WSB, and increasing the integration time generally seems to yield a better match. This is, however, not true for all cases. It can be seen that until an integration time of 2.43, the matching is better as the value of the integration time is increased. For a value of 2.75, however, integration of both strainlines is terminated too quickly, leading to a worse match. For the final value of 5.0, the strainline matches again with the WSB. This indicates that while in general increasing integration time is a viable choice, it does not guarantee better matching. Errors arising from numerical solving of the ODE's may still lead to too quick termination of the strainline integration procedure. When no stable set is available to verify the results, this may lead to loss of information causing us to miss part of the WSB.

This issue may be easy to combat by simply including a sufficient number of initial conditions when searching for LCS around a planet. While a single initial condition might give a strainline that is too short, having multiple initial conditions very close to one another might act as a form of redundancy, allowing some to fail but others to give the qualitative results desired. The assumption here is that initial conditions sufficiently close to each other give qualitatively the same strainline.

To illustrate this, two "clouds" are formed around the initial conditions IC_1 and IC_2, each consisting of 25 points. The cloud corresponding to the leftmost initial condition (IC_2) is shown in Figure 6.6. In Figure 6.7 the resulting strainlines for varying integration time are shown, using the points in these clouds as initial conditions.

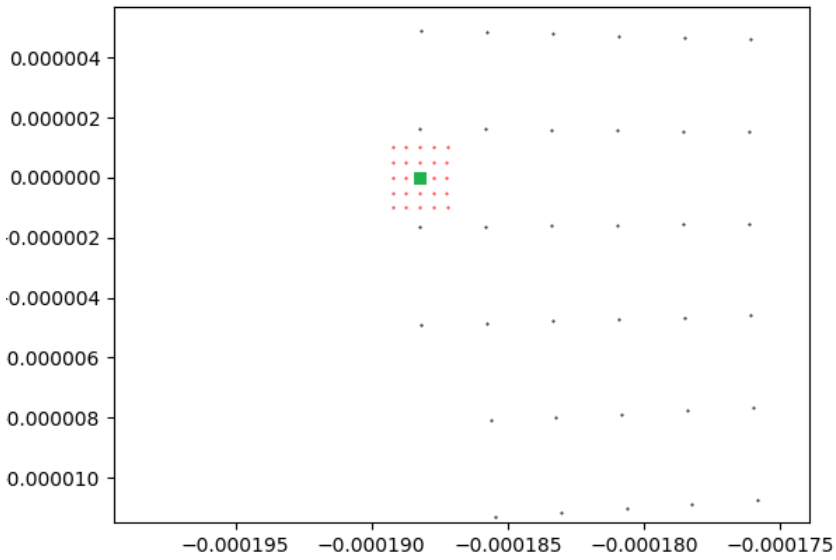

Figure 6.6: Cloud of initial conditions around IC_2 (green square)

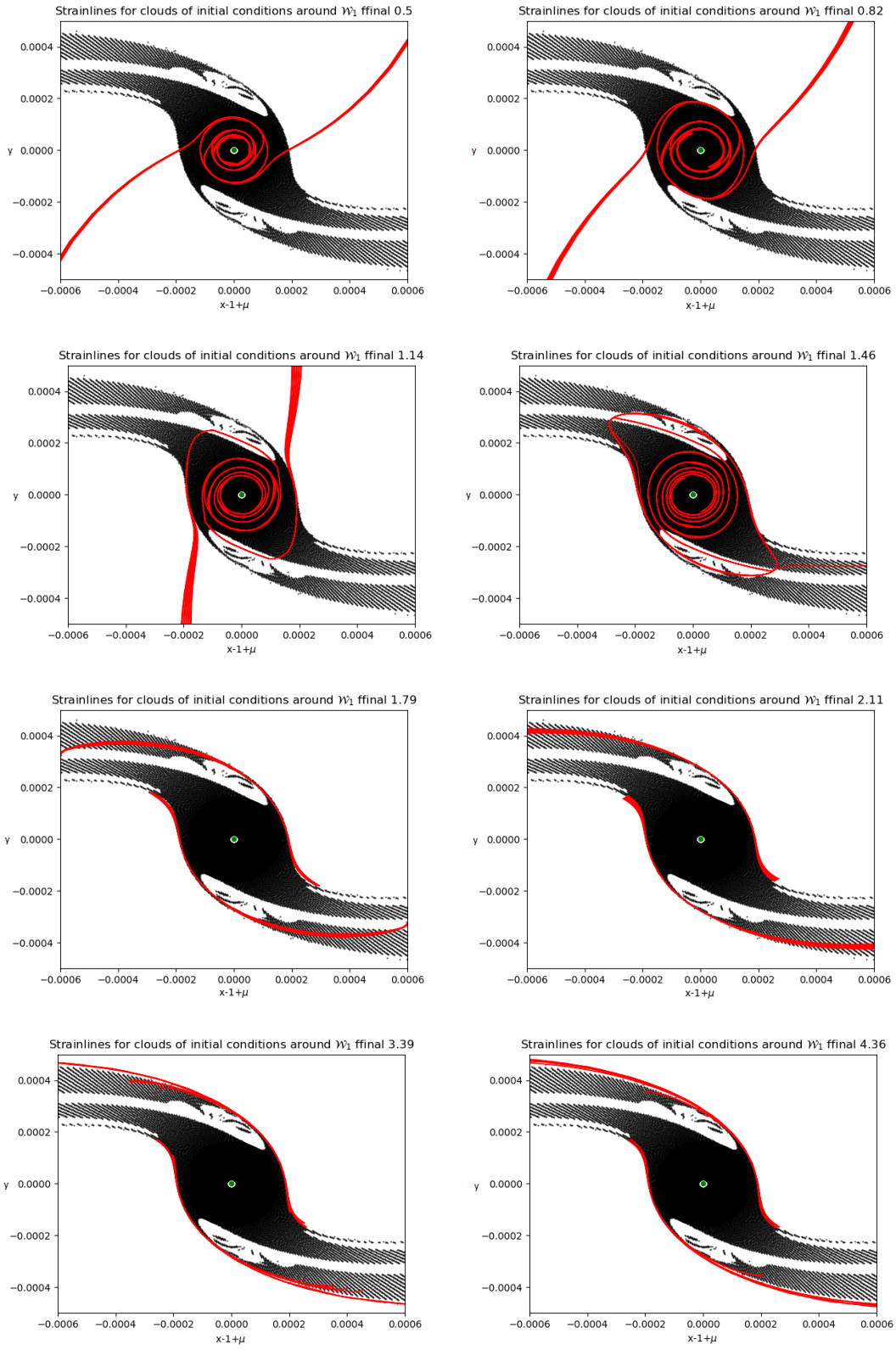

Figure 6.7: Strainlines for clouds of 25 initial conditions around IC_1 and IC_2

The results in Figure 6.7 confirm the hypothesis. While some inidividual strainlines show early termination due to failure in the numerical process, using a sufficient number of initial conditions close together can aid as a counter for this, and ensure that while numerical errors may arise no information on the shape of the WSB is lost.
Having computed sufficiently large strainlines with clouds as initial conditions for various values of f_{final}, a further analysis on the selection of $\mathscr{F}$ for the ERTBP can be performed. The procedure is as follows:

1. Choose two cases from Figure 6.7. For this analysis one case is chosen for which strainlines do not match with the WSB ($f_{final} = 0.82$), and one case is chosen for which the strainlines do match with the WSB ($f_{final} = 4.36$).

2. For all lines within these sets (i.e: 50 lines per set), the remaining procedure of converting to LCS is carried out. This is done for $\mathscr{F} = 1$ and $\mathscr{F} = 50$.

3. Parameters resulting from LCS extraction are saved for each line in each set. More specifically: average values along the strainlines and the corresponding neighbours (λ_2, λ_2^+, and λ_2^-) are stored.

4. Ratios of λ_2^+ and λ_2^- to λ_2 are computed and plotted for each strainline in the set. The results for both sets are shown in Figures 6.8 and 6.9

Figure 6.8: Analysis to determine importance of $\mathcal{F}$ selection for $f_{final} = 4.36$

Figure 6.8 shows the ratios of average λ_2 values between neighbours and the original strainline for two values of $\mathcal{F}$. The red line represents a ratio value of 1. Figure 6.8 gives a valuable insight regarding the role of $\mathcal{F}$. In most cases, the red and orange square lie on the same side of the red line. That means that for both $\mathcal{F}$ settings, the result in decision on wether or not a strainline is classified as LCS is the same. This indicates that while differences in $\mathcal{F}$ may yield substantial differences in the *values* of λ_2 (which was evident from Figure 6.4 and can be noted from the usage of the log scale on the y axis in Figure 6.8), the ratio of the average λ_2 values for the lines usually lies on the same side of the red line. It may therefore be concluded that while increasing the value of $\mathcal{F}$ may yield more accurate values of λ_2, the ultimate decision is not affected to a great degree. If we consider computational effort, this decision on what value of $\mathcal{F}$ to choose turns into a trivial one. Computing the λ_2 values for the 50 strainlines used in Figure 6.8 with $\mathcal{F} = 1$ took around 40

minutes. Using a value of $\mathscr{F} = 50$ this computation took 20 hours. It can be concluded that $\mathscr{F} = 1$ is a viable choice for the remainder of this work.

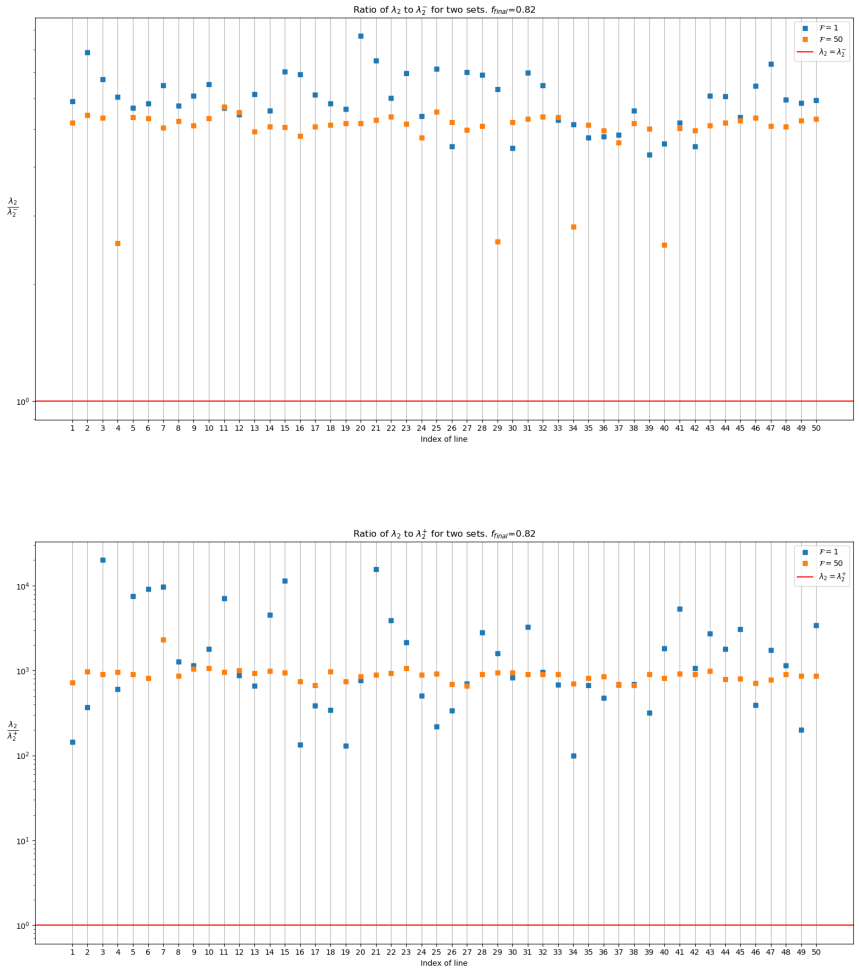

Figure 6.9: Analysis to determine importance of $\mathscr{F}$ selection for $f_{final} = 0.82$

Figure 6.9 shows that for all strainlines, values of the ratios always lie on the same side of the red line. Thus, in both cases ($\mathscr{F} = 1$ and $\mathscr{F} = 50$) all strainlines are classified as LCS. It is evident from Figure 6.7 that the LCS do not correspond to the WSB. It may therefore be concluded that proper care must be taken in determining values of f_{final}. The process of going from strainlines to LCS does not filter out these lines, and may give deceptive results for the WSB.

Varying integration time pointwise

The results shown in the previous subsection indicate that using a large, contant, integration time for the entire system may be more desirable than a small value. However, it was also mentioned

that this generally comes at a cost of computational effort. For this reason, it might be of interest to not increase the value of f_{final} for the entire system, but rather to use different values of f_{final} for each point on the grid. The question that needs to be answered is an obvious one: "How to determine this f_{final} value for each point?".

Recall that in Figure 6.3 values for f_{final} were taken from the WSB file used as validation data. The values chosen represented the final returning anomaly of the point in the $\mathcal{W}_1$ set. It was also found that these values gave nearly perfect results for the matching. This indicates that in an ideal case, an optimal value of f_{final} may be the value that we would find in the stable set for that point. The problem, however, is twofold:

- Given a stable set, not every point on the grid will have a matching point in the stable set from which a value of f_{final} can be taken.
- In a practical setting, making use of the stable set is not possible. In fact, the goal is to see if this theory on relating LCS to WSB may provide an interesting alternative to classical stable set manipulation. In an ideal case, we therefore find LCS as WSB without having used any information from the stable sets.

In order to continue, an assumption is made regarding the orbit that a point on the stable set might follow if it were located in the stable set. The assumption is that a particle originating from a stable point might follow something close to a Kepler orbit. Using this assumption we construct the osculating ellipse at (r,θ) with focal point P_2 and periapsis distance r. For this osculating ellipse, the (a-dimensional) orbital period is calculated as follows:

$$T = 2\pi\sqrt{\frac{a^3}{\mu}} \tag{6.1}$$

where a is the semi-major axis of the osculating ellipse with eccentricity e, computed with $r/(1-e)$ and μ is the mass parameter $m_2/(m_1+m_2)$.

The local value of f_{final} used for the procedure can now be related to the value of T of the osculating ellipse with the local point as its periapse. Resulting strainlines for various values of locally varying f_{final} are shown in Figure 6.10.

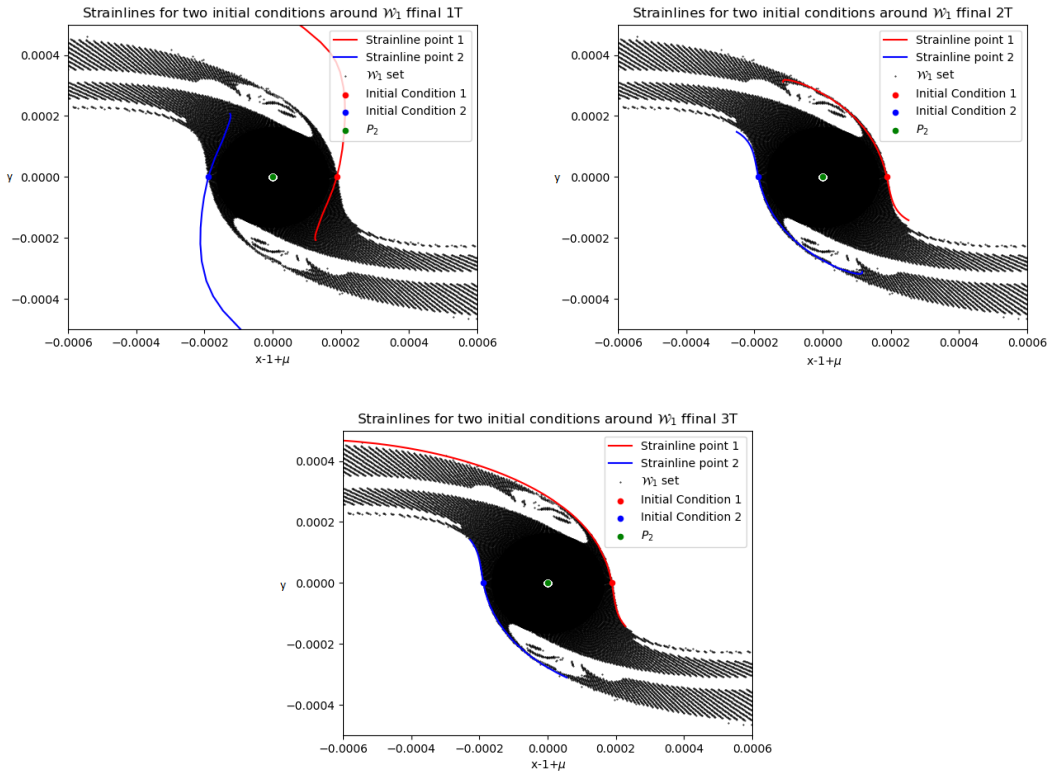

Figure 6.10: Effect of varying integration time locally on 2 strainlines for values of T, 2T, and 3T respectively

It can be noted from Figure 6.10 that using the orbital period of the osculating ellipse as the local f_{final} is not a viable strategy. This indicates that the points in the $\mathcal{W}_1$ stable set do not behave similar to what they would in a Kepler orbit. Instead, increasing the value to 3 times the orbital period seems to yield better results. In the next subsection results for the whole search space will be compared.

6.2.5 Search for LCS in 2D-space around planet

As was stated earlier, in the work done in [18] it was confirmed that WSB correspond to repelling LCS of the system. What remains to be seen is what LCS can be found around a planet without any a priori knowledge of the WSB. This idea will be explored in this section.

As has been shown earlier, many parameters influence the resulting strainlines and therefore the final LCS. One has to be aware of the computational effort required in computing LCS. Because of this constraint, not all parameters can be tweaked independently to each give resulting LCS. To make this process more efficient, in a first step the strainlines around the planet are calculated for different configurations. Based on the results of these strainlines, some configurations are chosen to further extract LCS from.

Computation of Region $\mathscr{U}_0$

The first step in computing strainlines around the planet is the computation of the region $\mathscr{U}_0$. This is done for similar reasons as for the Double Gyre validation problem. Because of the computational effort required in the process of obtaining LCS, reducing the amount of redundant computations done is desirable. Filtering the initial grid space is therefore an effective approach. Obtaining region $\mathscr{U}_0$ relies on the checking of condition (B). One of the steps involved in checking this condition is the computation of the Hessian of the λ_2 scalar field. As was mentioned earlier, the value of the perturbation parameter ϵ in the central differencing procedure must be chosen carefully. Too large values may miss nuances in the λ_2 field, whereas too small values are too local and fail to capture the λ_2 field all together. In the case of the Double Gyre, the region $\mathscr{U}_0$ was given in the reference paper [7], and a value of $\epsilon = 10^{-5}$ gave a proper match. For the ERTBP, no previously computed and verified region $\mathscr{U}_0$ exists, and as such a different approach for ϵ determination is developed. It is assumed that too small or too large values will give rise to many isolated points being classified as satisfying (B). Proper values of ϵ are expected to give rise to "cleaner" regions, similar to what is displayed in Figure 5.3. Computed regions $\mathscr{U}_0$ are therefore compared on the amount of isolated points, and the ϵ value corresponding to the least cluttered region is chosen. Results of this analysis are shown in Figure 6.11.

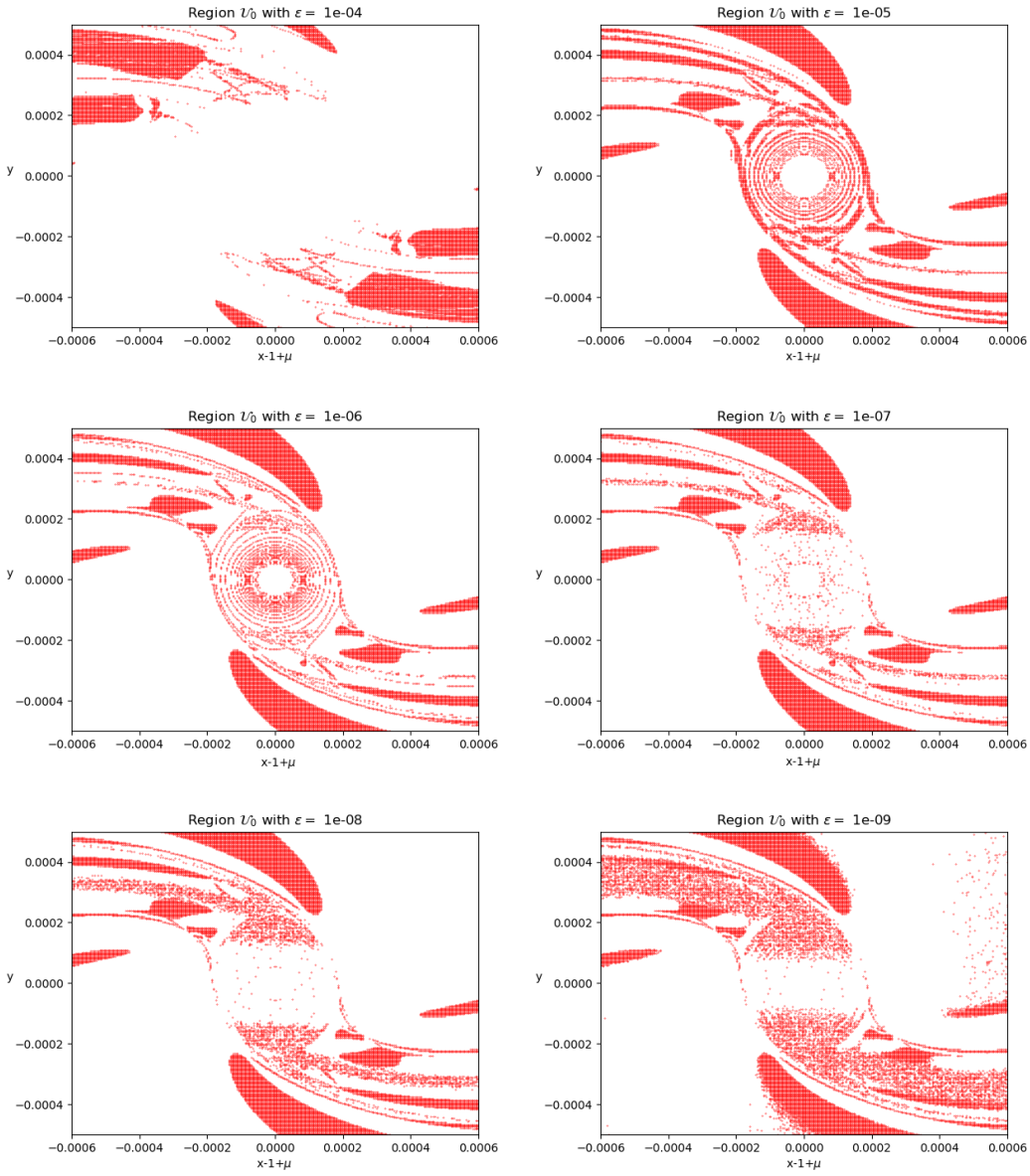

Figure 6.11: Region $\mathcal{U}_0$ for varying values of ϵ in central differencing. Computed on (300×300) grid.

From Figure 6.11 it can be noted that a too small value of ϵ leads to cluttered points, as was expected. One may also note that choosing values of ϵ that are too large, seems to also give wrong results, and a big part of what $\mathcal{U}_0$ is expected to be is missed. It has been verified that using values up to $\epsilon = 10^{-1}$ decrease region $\mathcal{U}_0$ even more and leads to more numerical noise.

It it concluded from Figure 6.11 that a value of $\epsilon = 10^{-5}$ is a viable choice. There are little to no isolated points, and the edge where the LCS is expected to be (based on comparison with the stable sets) is thicker (i.e: contains more points) than for $\epsilon = 10^{-4}$. This is desirable, as it has been shown in Section 6.2.4 that having many initial conditions close to each other acts as a form of

redundancy.
The standard approach would be to now integrate outer ODE (5.5) using all points in $\mathscr{U}_0$ as initial conditions. However, in the remainder of this subsection many configurations for the integration time are checked. For computational reasons, it is not feasable to do this exercise using all points in $\mathscr{U}_0$ as initial conditions. For that reason, less initial conditions around P_2 are constructed which will serve as starting points for the integration for the remainder of this subsection. These are shown in Figure 6.12. Note that after having done this exercise and having determined guidelines for configuration settings, the software will be used for computing LCS in the Earth–Moon system in Section 6.3. Because only one set of configuration settings will be used for that procedure, the proper method involving propagation from $\mathscr{U}_0$ is used there.

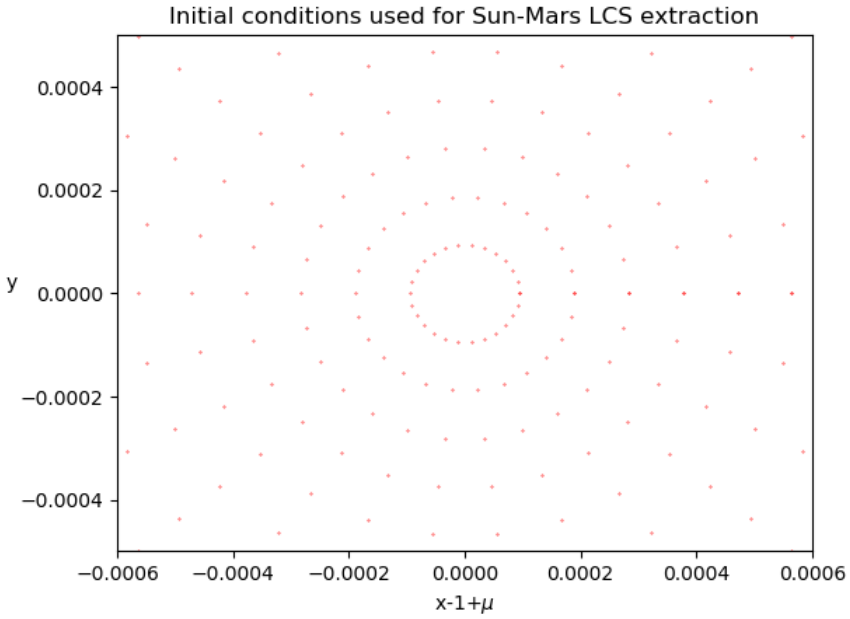

Figure 6.12: Initial conditions used for LCS extraction

Search for strainlines in 2D-space around planet

Firstly, the strainlines around Mars are computed for varying values of f_{final}. The results are shown in Figure 6.13.

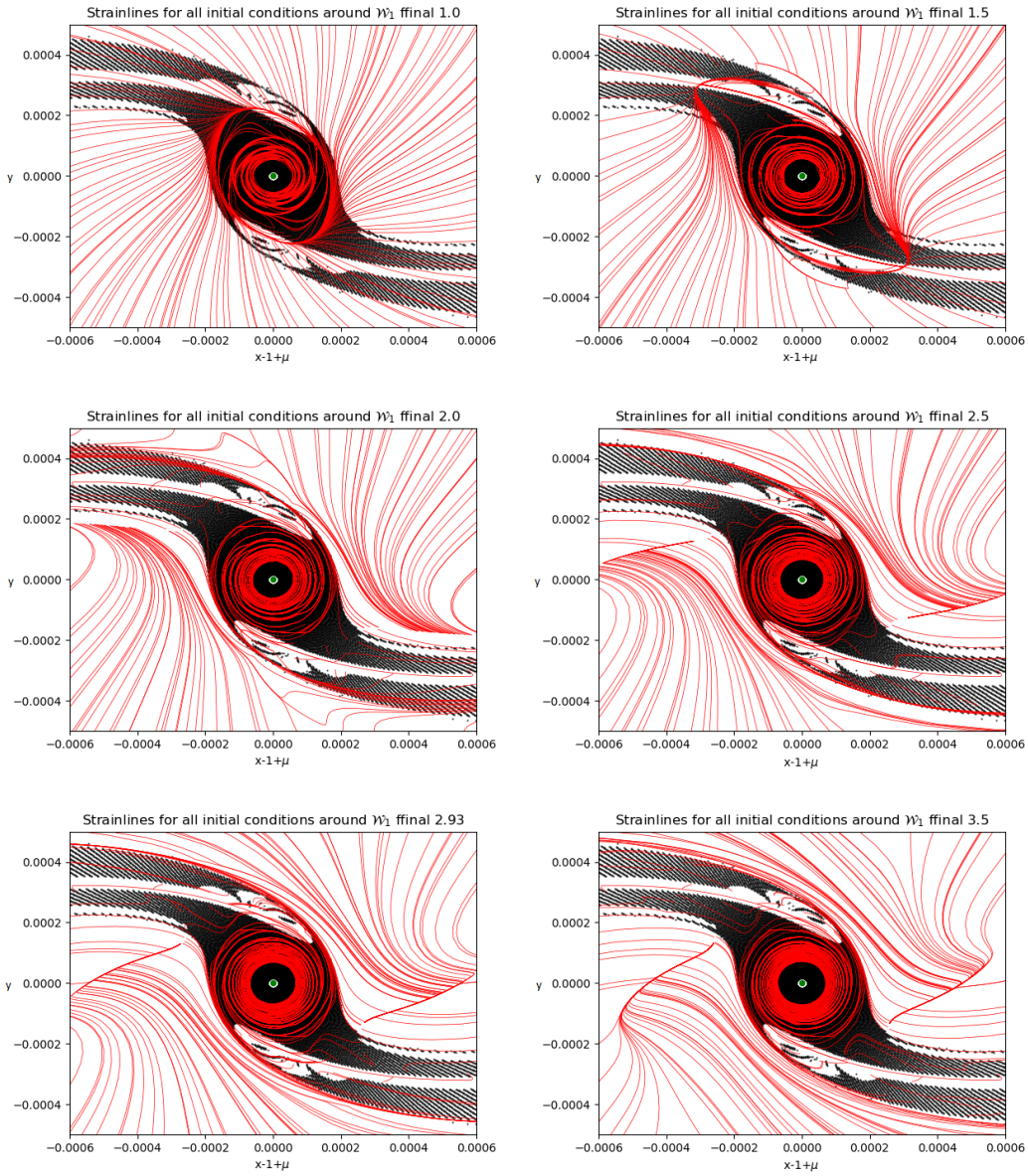

Figure 6.13: Effect of varying integration time on strainlines

Figure 6.13 indicates that, following the idea gained from the previous section, too small integration times fail to capture the shape of the WSB. As the integration time is increased, the strainlines seem to trace the WSB better. Some strainlines do cross into the black area, but the majority of strainlines seem to curve around the $\mathcal{W}_1$ stable set. Note that crossing into the black area might not be a weakness per se, as it the lines might correspond to WSB of other sets $\mathcal{W}_n$. This will be explored later in this chapter.

In Figure 6.14 the strainlines are shown if values of t_{final} are varied locally. Results are shown for

local f_{final} values of T, $2T$, and $3T$ respectively.

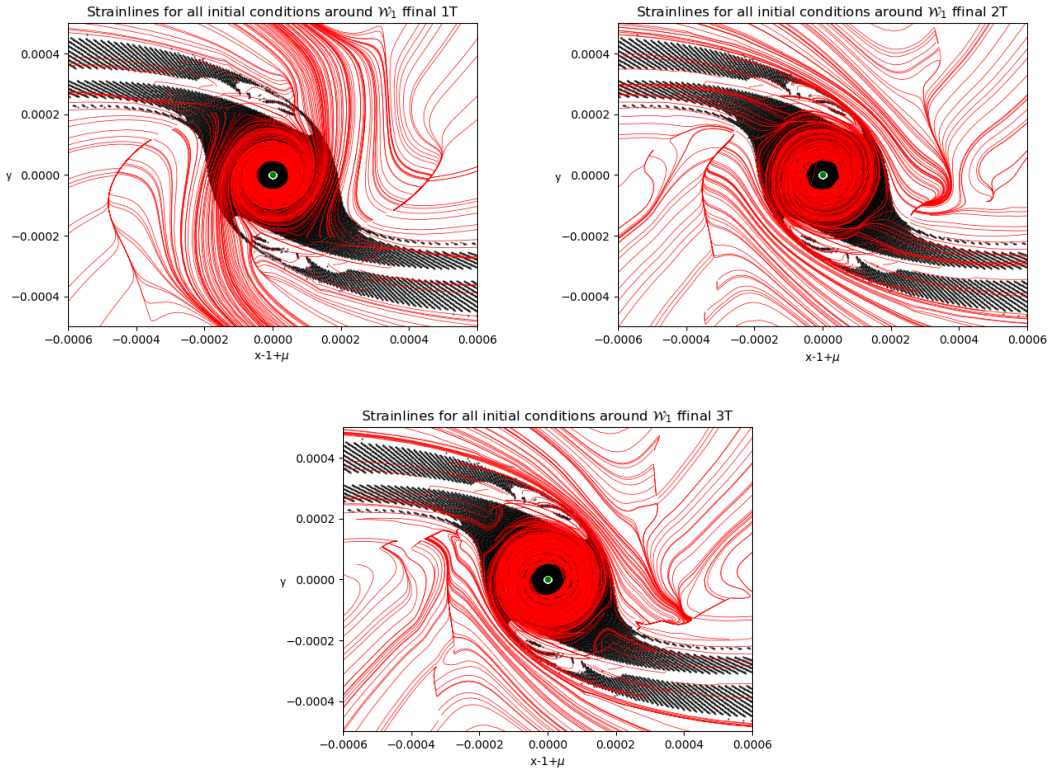

Figure 6.14: Effect of varying pointwise integration time on strainlines

Figure 6.14 confirms what has been shown earlier: larger integration times give more accurate representations of the WSB. One might also conclude that using varying f_{final} values is not by definition better. This is hard to assess merely by looking at the strainlines. Conclusions regarding the choice between constant or variable integration time are given when converting to LCS in the next section.

Strainlines to LCS in 2D-space around planet

Having computed the strainlines for the system for some configuration settings, the following are chosen to extract LCS from:

- For constant integration time settings, values of 1.0 and 3.5 are chosen. Judging by the strainlines, an f_{final} value of 3.5 seems to trace the WSB the best, and it is to be seen if this holds true for the LCS as well. The value of 1.0 is chosen for the opposite reason. The strainlines do not seem to trace the $\mathcal{W}_1$ set at all, and it remains to be seen if the process of converting strainlines to LCS filters out these lines or not.

- For variable integration time settings all cases (values of T, $2T$, and $3T$) are selected. Case T is chosen for similar reasons as the constant value of $f_{final} = 1.0$. The other cases seem to both trace the boundary to a similar degree and neither one seems more promising than the other by looking at the strainlines. Filtering to LCS may give more information regarding the effect of changing this integration time from $2T$ to $3T$. Furthermore, comparing these results to the LCS results obtained with $f_{final} = 3.5$ will give a strong idea on using fixed versus variable integration times.

Results for constant, and varying integration times are shown in Figures 6.15 and 6.16 respectively.

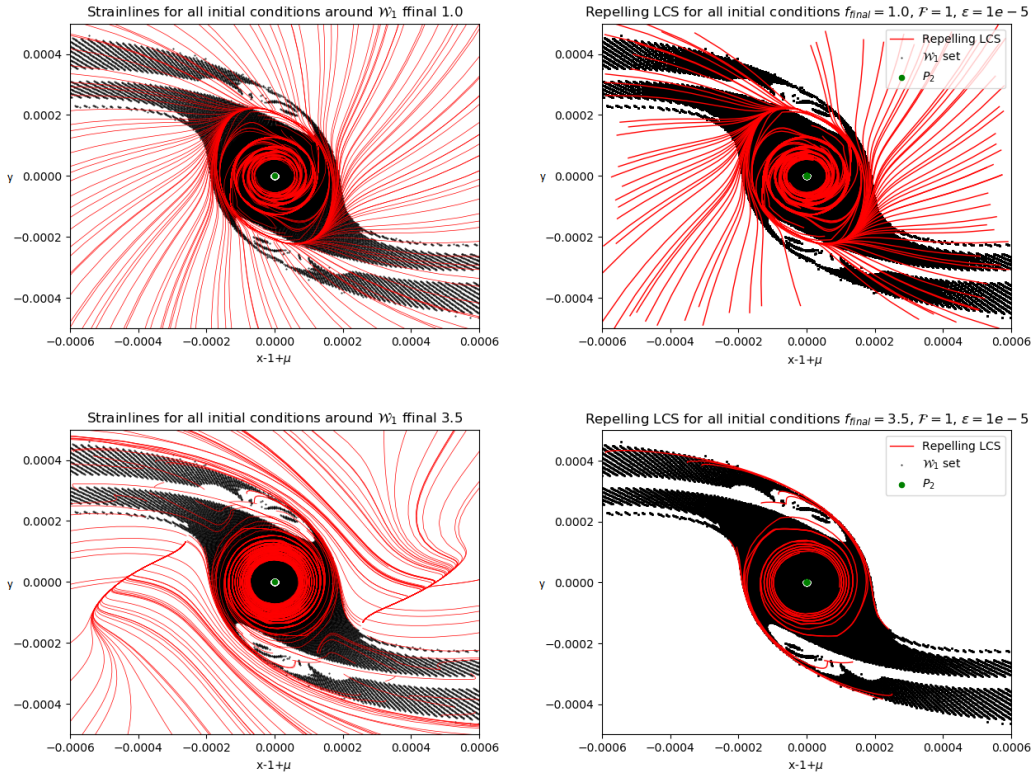

Figure 6.15: Strainlines (left) to LCS (right) for fixed integration time for full system

Figure 6.15 shows how strainlines are filtered to LCS for the two cases. It can be seen that in the case of $f_{final} = 1.0$ a considerable number of lines are conserved as LCS. This can indicate two things:

- The procedure to compute LCS is susceptible to errors made in choice of integration time. Values that are too small lead to wrongly identified LCS which do not trace the WSB.
- The fact that lines are conserved indicates that some other dynamical structure is present in the problem. This may indicate the boundary of a set other than $\mathcal{W}_1$. This will be further explored in the next section.

From the bottom row of Figure 6.15 it can be concluded that many of the strainlines in the white regime are correctly filtered out when converting to LCS. In fact, the remaining lines trace the boundary well as expected. Note that there does seem to be a "core" of lines crossing the black region. This may be attributed to numerical errors, or it may indicate a structure of sets other than $\mathcal{W}_1$. This will be further examined in the next section.

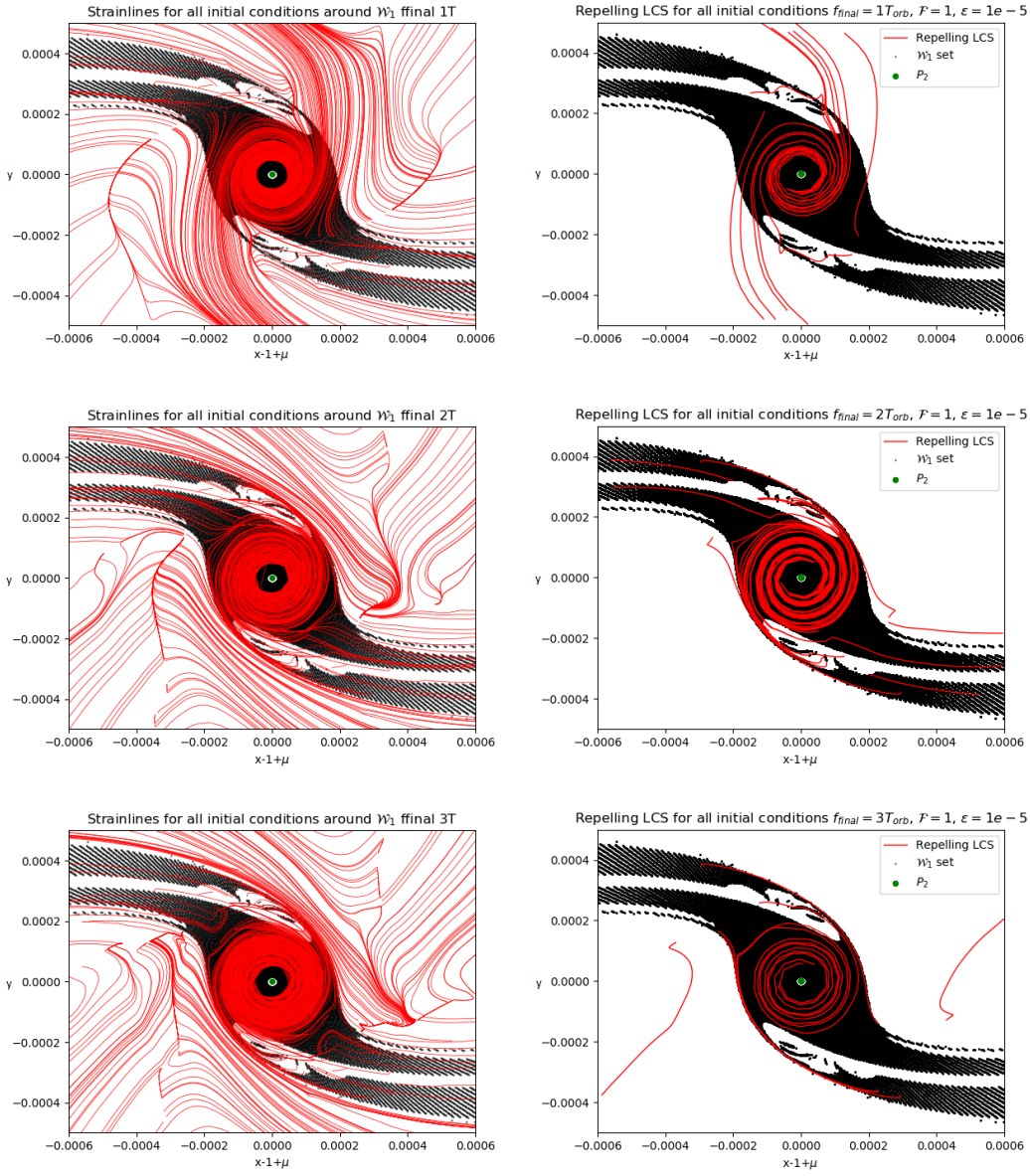

Figure 6.16: Strainlines (left) to LCS (right) for varying integration time for full system

The results from Figure 6.16 show that for integration times of $2T$ and $3T$ all but two of the strainlines in the white region are preserved as LCS. Noticing the shape of these lines this can most

likely be attributed to noise in the numerical procedure. Comparing Figure 6.16 to Figure 6.15 also shows that using varying integration times is not necessarily better than simply using a fixed final value. It is also computationally more efficient to use constant integration times, as orbital periods of initial conditions far from P_2 tend to become large, causing f_{final} to be large and thus making the computation take unnecessarily longer.

6.2.6 LCS comparison with WSB for n revolutions

From the results shown in the previous section it can be concluded that LCS extracted for the whole system, without making use of a priori knowledge of the stable sets, seem to trace the WSB of the $\mathcal{W}_1$ quite well. However, some extra structures seem to be present in all results. In this section the earlier extracted LCS are compared with other stable sets for the same system. For this problem, a total of six sets are avaiable ($\mathcal{W}_n$ with $n = 1,2,\ldots,6$). The sets are displayed in Figure 6.17.

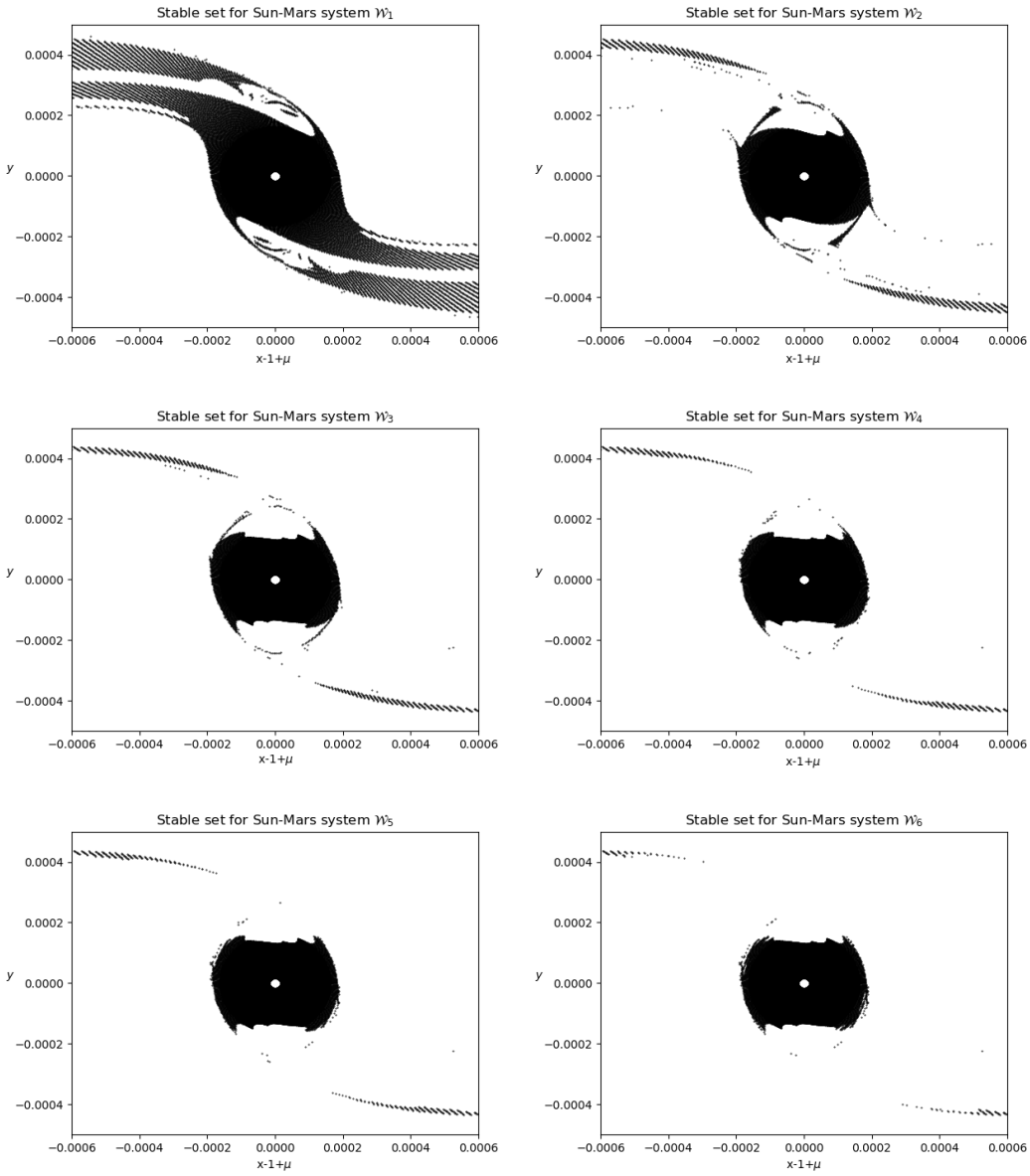

Figure 6.17: Sets $\mathcal{W}_1 \ldots \mathcal{W}_6$ for the Sun–Mars system

From Figure 6.17 it can be concluded that for this marticular system, the largest difference occurs between $\mathcal{W}_1$ (used earlier) and $\mathcal{W}_2$. The difference in other sets seem to be small when compared to $\mathcal{W}_2$. For that reason, LCS in this section are computed for $\mathcal{W}_2$ only. The earlier computed LCS laid on top of $\mathcal{W}_2$ are shown in Figure 6.18.

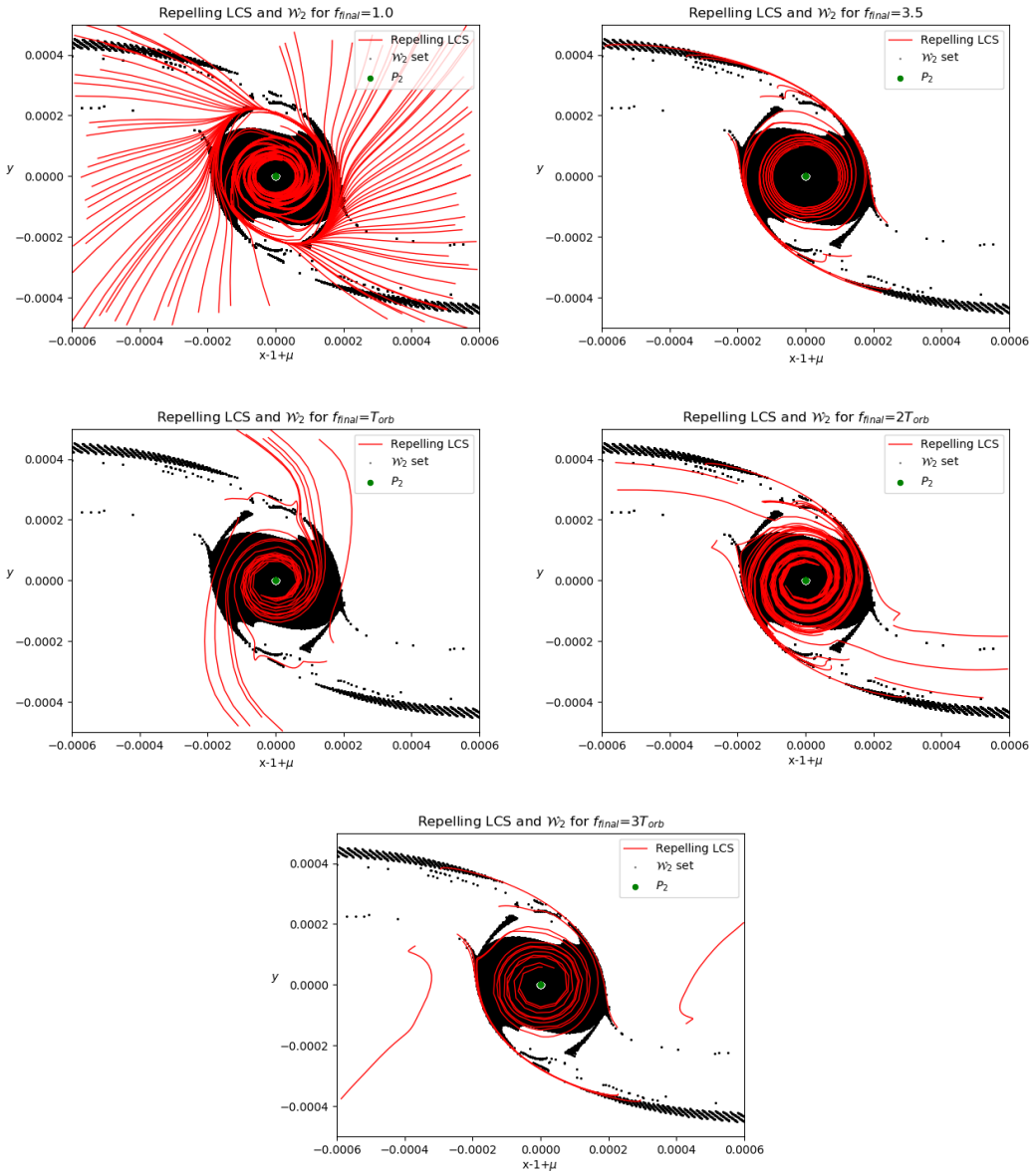

Figure 6.18: Repelling LCS for 5 f_{final} settings around $\mathcal{W}_2$

From Figure 6.18 the following can be concluded:

- When integration times are too short ($f_{final} = 1.0$, $f_{final} = T_{orb}$, and $f_{final} = 2T_{orb}$), resulting LCS do not correspond to LCS of W_n no matter what value of n is chosen. This allows us to conclude that proper choice of f_{final} is crucial to ensure results are trustworthy.
- Points where integration of the strainlines stops naturally are not arbitrary. From the results on the $\mathcal{W}_1$ set it seemed that the outer line tracing the stable set was not followed fully due to numerical errors. When looking at Figure 6.18 it is clear from the results of $f_{final} = 3.5$

and $f_{final} = 3T_{orb}$ that this point where integration stops corresponds to the point where continuity of the boundary of $\mathcal{W}_2$ also stops. This region is highlighted in blue in Figure 6.19.

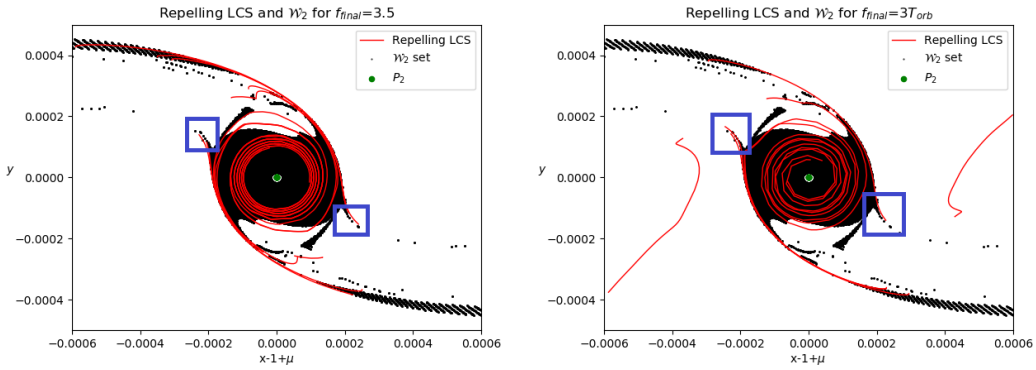

Figure 6.19: Integration naturally stops in blue area when boundary of $\mathcal{W}_2$ stops

- Similar to the results found for $\mathcal{W}_1$, choice of f_{final} between constant or varying values in the domain seems to not yield a difference in accuracy for the majority of the search space. In fact, it can be concluded that constant integration times might perform slightly better, because as the strainline resulting from solving the outer ODE goes closer to P_2, the value of the local orbital period of the points on the strainline decreases. As a consequence, the value of f_{final} for the inner ODE also decreases. As was shown earlier, small f_{final} values tend to be a bad choice overall, and as such results in this regime close to P_2 will by definition be inaccurate.
- Comparing results of LCS and $\mathcal{W}_1$ to those of $\mathcal{W}_2$, it seems that the results for $\mathcal{W}_2$ give a better match. This is explained by the fact that the LCS can be seen as an average result describing the dynamics of the system (for all $\mathcal{W}_n$). It was shown in Figure 6.17 that main differences between sets were seen between $\mathcal{W}_1$ and $\mathcal{W}_2$. Sets $\mathcal{W}_3$ and onwards seem to not give many differences with $\mathcal{W}_2$, indicating that the average shape of $\mathcal{W}_n$ around P_2 is most closely resembled by $\mathcal{W}_2$. This hypothesis remains to be tested for other planets.

6.3 Test case: Earth–Moon system

In the previous sections the developed software for both the FTLE algorithm and Variational Theory was applied to the Sun–Mars system. For this system, the stable sets from other works were used as comparison data. The aim of this section is to apply both LCS extraction algorithms to the Earth–Moon system. For this sytem, no stable sets have been computed. As such, this will be an exercise in the practical utility of applying LCS algorithms as an alternative to traditional stable set manipulation.
An overview of all settings is given below:

Table 6.3: ERTBP configuration settings used for the Earth–Moon case

Variable	Symbol	Value
Earth mass	m_1	$5.972 \cdot 10^{24}$ kg
Moon mass	m_2	$7.346 \cdot 10^{22}$ kg
Earth–Moon system eccentricity	e_p	0.0549
P_3 orbit eccentricity	e	0
Initial true anomaly	f_0	0

6.3.1 FTLE application to Earth–Moon system

The resulting FTLE field for the Earth–Moon system is shown in Figure 6.20. Use is made of a final integration time of $f_{final} = 3.0$, following results shown in previous sections. Larger values of f_{final} show no increase in result accuracy while increasing computational time.

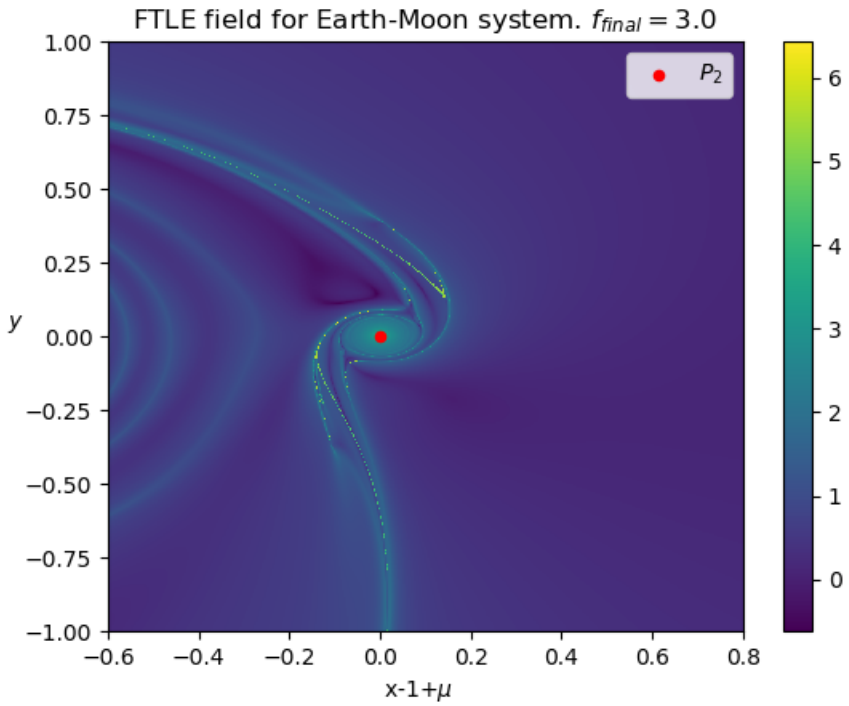

Figure 6.20: FTLE field for Earth–Moon system computed on 1000 × 1000 grid

Figure 6.20 indicates the shape of the repelling LCS quite well (light colors). One can note the presence of three curves between $x - 1 + \mu$ values of -0.6 and -0.2 approximately. Intuitively, we do not expect these lines to correspond to the repelling LCS of the system, or the WSB of the stable sets $\mathcal{W}$ of the Earth–Moon system. This can be tested by simulating the orbits of points on either side of the curves, and comparing the results. This is shown in Figure 6.21. Note that the

generated orbits go outside the domain for which the FTLE field was generated, which explains the blank background.

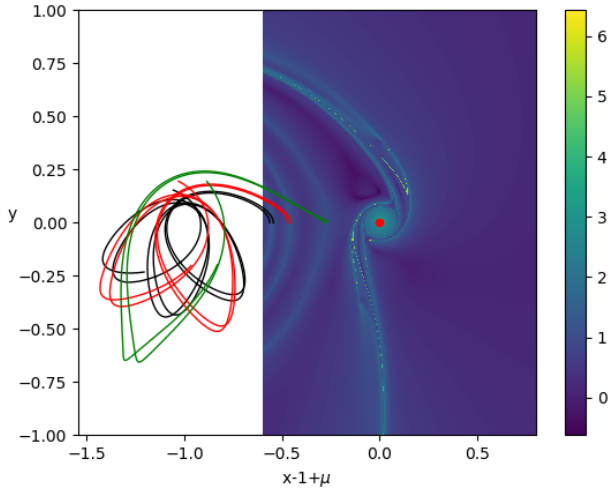

Figure 6.21: 3 pairs of orbits generated on top of FTLE field

From Figure 6.21 it is evident that each pair of orbits with initial conditions on either side of the three leftmost FTLE ridges stays together and does not diverge. This indicates that these ridges are the result of numerical noise, and do not correspond to repelling LCS (or WSB) of the system. It can also be seen that lines corresponding to the highest FTLE field values can be distinguished. In fact, these regions tend to run through the area we may intuitively expect to correspond to the WSB. Resulting orbits with initial conditions around these points are shown in Figure 6.22.

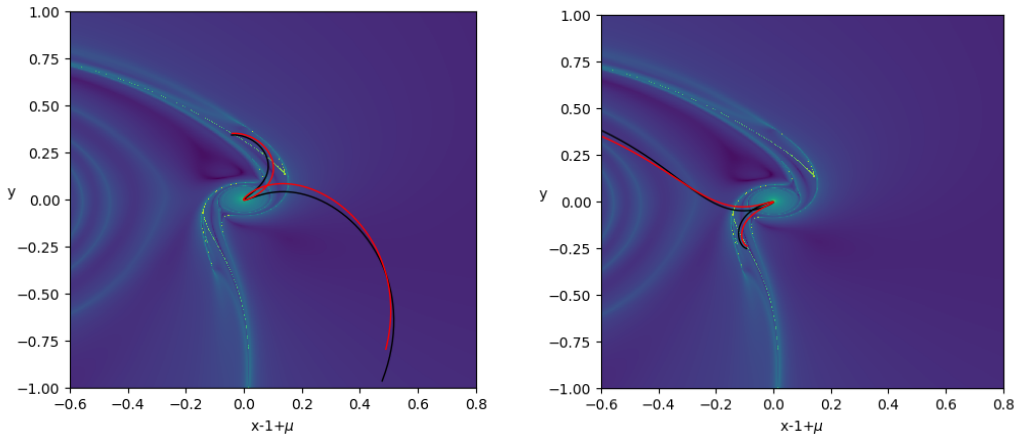

Figure 6.22: Orbits generated with initial conditions around highest FTLE regime

From Figure 6.22 it is clear that while the distinct lines correspond to the highest FTLE values in the field, the generated orbits do not diverge. These lines do not seem to be repelling LCS of the system revealing an important conclusion: one cannot simply say that large FTLE field values have a higher probability of revealing "correct" repelling LCS. Since the lines cross through the area that intuitively makes up the WSB, it might be the case that only outer edges of the regimes can be considered potential WSB. This can not be assessed based on the experiments done in this work, and further study is required.

Orbits with initial conditions around the "outer edge" of the expected WSB are generated to verify this hypothesis. Results are shown in Figure 6.23.

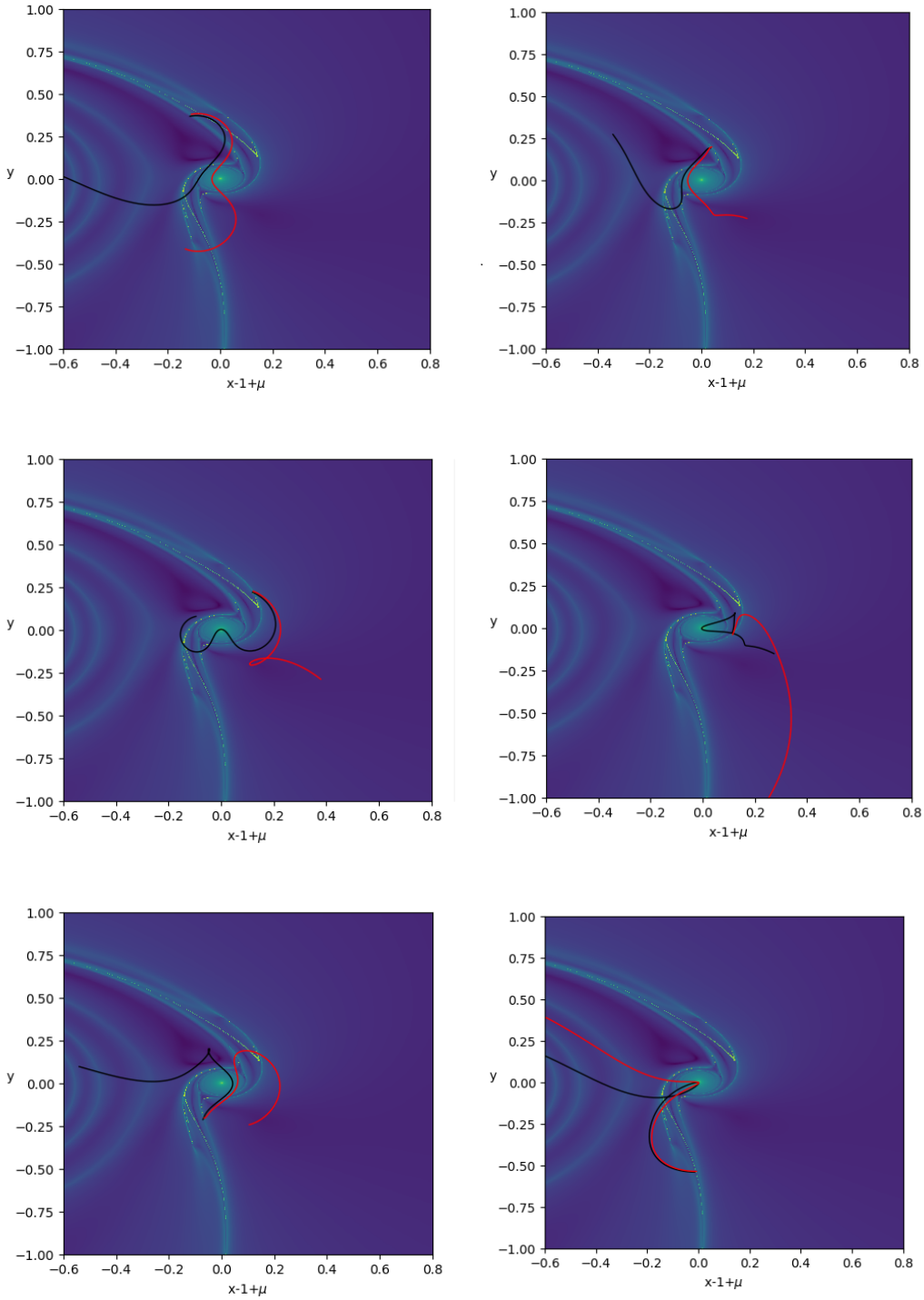

Figure 6.23: Orbits generated with initial conditions around expected WSB

It can be concluded from Figure 6.23 that the outer edge of the light region does indeed corre-

spond to the repelling LCS and WSB of the system. All generated orbits tend to diverge fairly quickly.

It can be concluded from the FTLE application to the Earth–Moon system that the FTLE field gives a good insight into the overall shape of the stable set, but can not be used as a replacement directly. It has been shown that some parts of the FTLE field which correspond to ridges, do not function as repelling LCS (i.e: separatrices of dynamics). Also, it is shown that highest values of the FTLE field (largest ridges) are not more likely to be LCS. In fact, the highest distinctive regions in the Earth–Moon case turn out to not be LCS at all.
It is concluded that FTLE field application to the ERTBP might serve as a good initial experiment to approximate the stable set, especially considering that the computation time for generating FTLE fields is relatively low (grid of 1 million points on 14 cores takes around 3 hours). However it does not guarantee perfect resemblance and has to be used merely as an approximation.

6.3.2 Variational Theory application to Earth–Moon system

For application of the Variational Theory to the Earth–Moon system, firstly the region $\mathscr{U}_0$ must be computed. This is done for varying values of central differencing perturbation parameter ϵ. The best region $\mathscr{U}_0$ is chosen and serves as the initial condition grid for the remainder of the process. Furthermore, the associated value of ϵ is chosen for the remainder of the process involving computation of the Hessian. Following the results from the Sun–Mars case, a fixed value of integration time of $f_{final} = 3.0$ is used for this analysis. Results are shown in Figure 6.24.

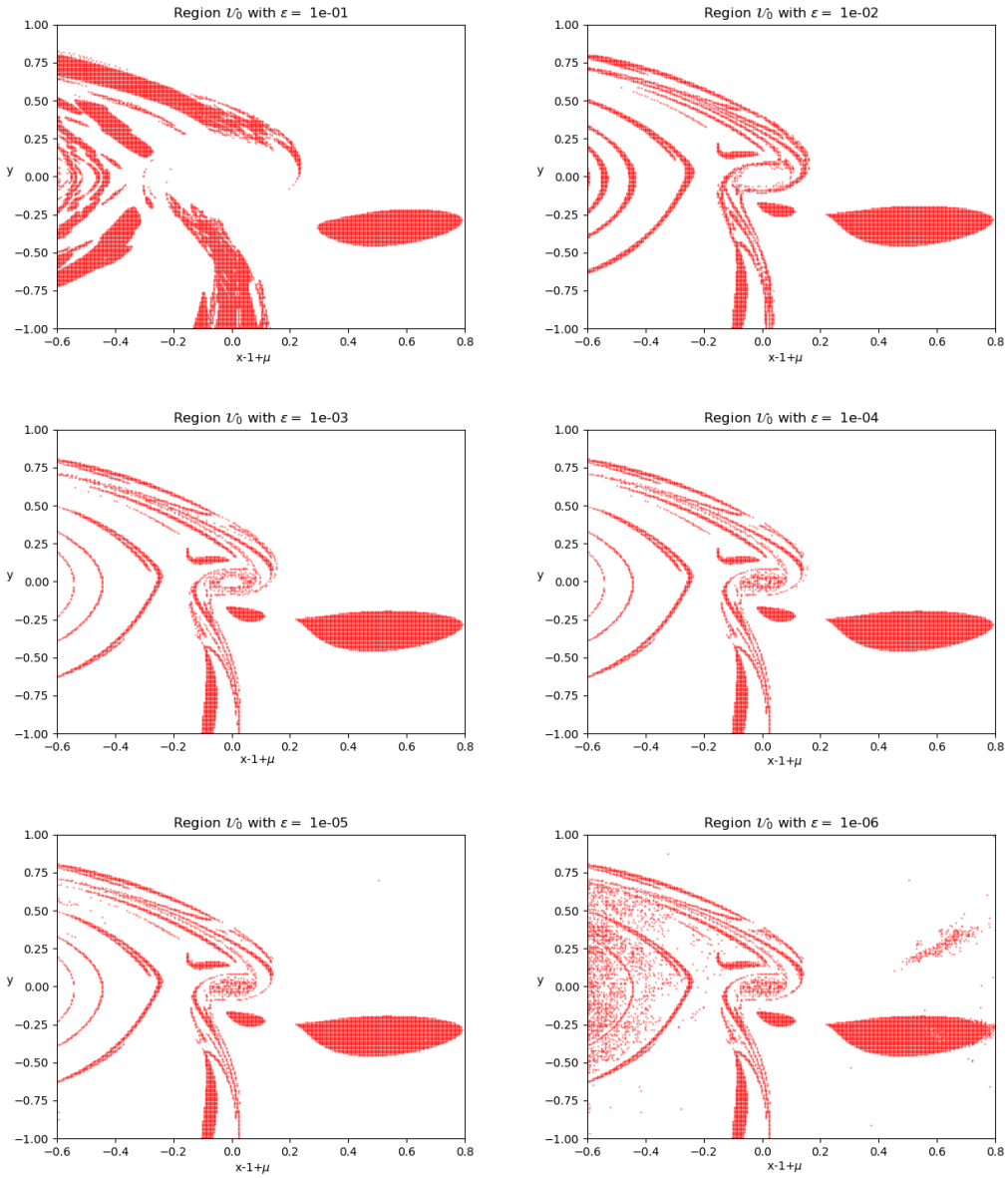

Figure 6.24: $\mathcal{U}_0$ for varying values of ϵ

From Figure 6.24 it can be concluded that a viable choice for ϵ is 10^{-2}. It gives the least amount of isolated points arising from numerical errors, and has the highest point density in the region which is expected to contain the LCS, as indicated by the FTLE results from Figure 6.20.
Strainlines computed with initial conditions in $\mathcal{U}_0$ corresponding to the $\epsilon = 10^{-2}$ setting, and resulting Repelling LCS computed with filtering parameter $\ell_{min} = 0.8$ and neighbourhood definition parameter $\delta = 3 \cdot 10^{-5}$ are given in Figure 6.25.

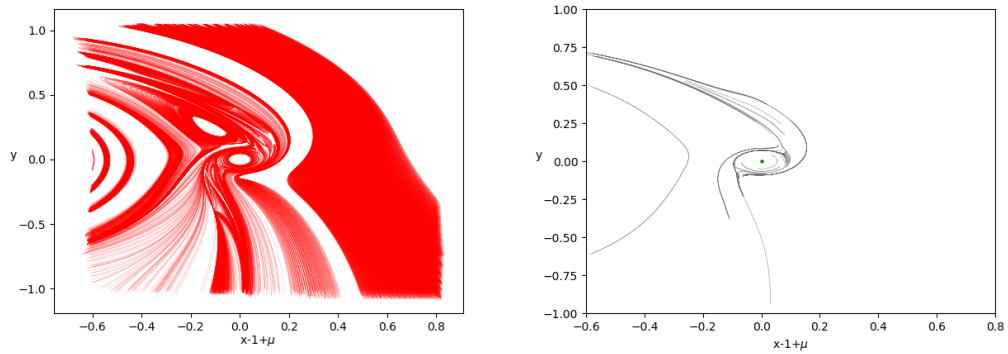

Figure 6.25: Variational theory application to Earth–Moon system. Left: Strainlines. Right: Repelling LCS

It can be noted that the leftmost line which intuitively would not be part of the WSB is also present. In the FTLE example, three of these lines were present. This indicates that the variational theory application has a lower false positive rate, but is not robust enough to fully filter out these random lines. Two pairs orbits are generated to verify that these lines are no seperatrices of dynamics. This is shown in Figure 6.26.

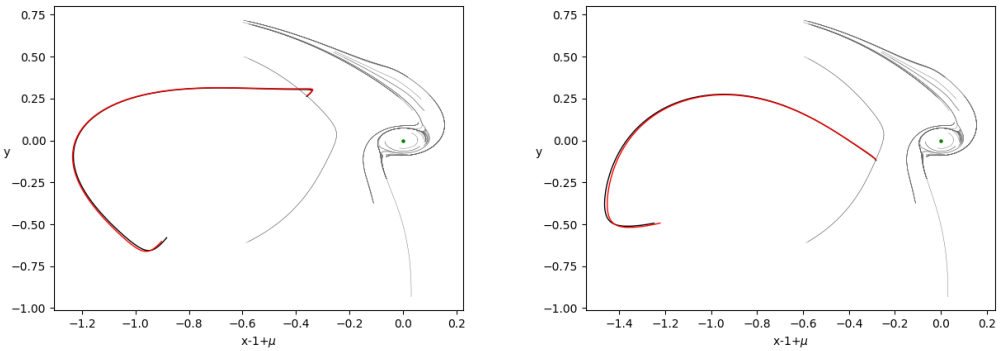

Figure 6.26: Two pairs of orbits generated from false positive line

From the LCS results of Figure 6.25 it can also be noted that many lines are generated close together in the top half of the domain. To check if these are the result of numerical noise and the outer region is the real LCS, or if these lines truly seperate the dynamics in some way, 5 sets of orbits are generated. Results are shown in Figure 6.27.

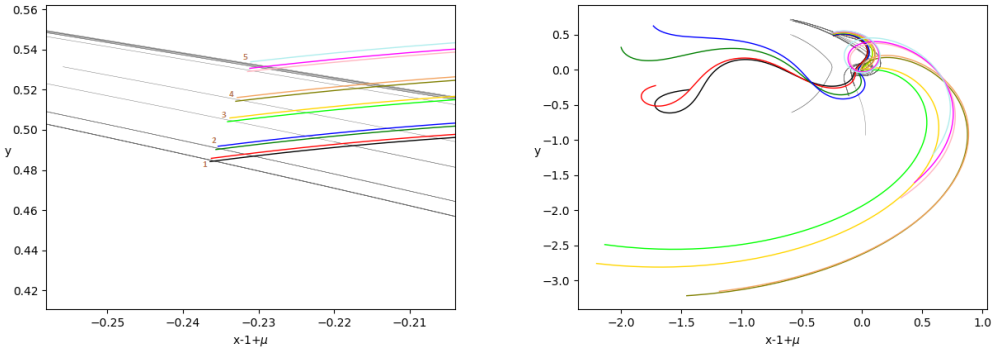

Figure 6.27: Left: Initial conditions for 5 sets of orbits used for analysis. Right: resulting orbits.

From Figure 6.27 it can be concluded that every set of orbits except for set 4 diverges. This is an indication that the line around which set 4 is generated is the result of numerical noise (similar to the leftmost line checked in Figure 6.26).

In Figure 6.28 the repelling LCS results from the variational theory are plotted on top of the previously generated FTLE results.

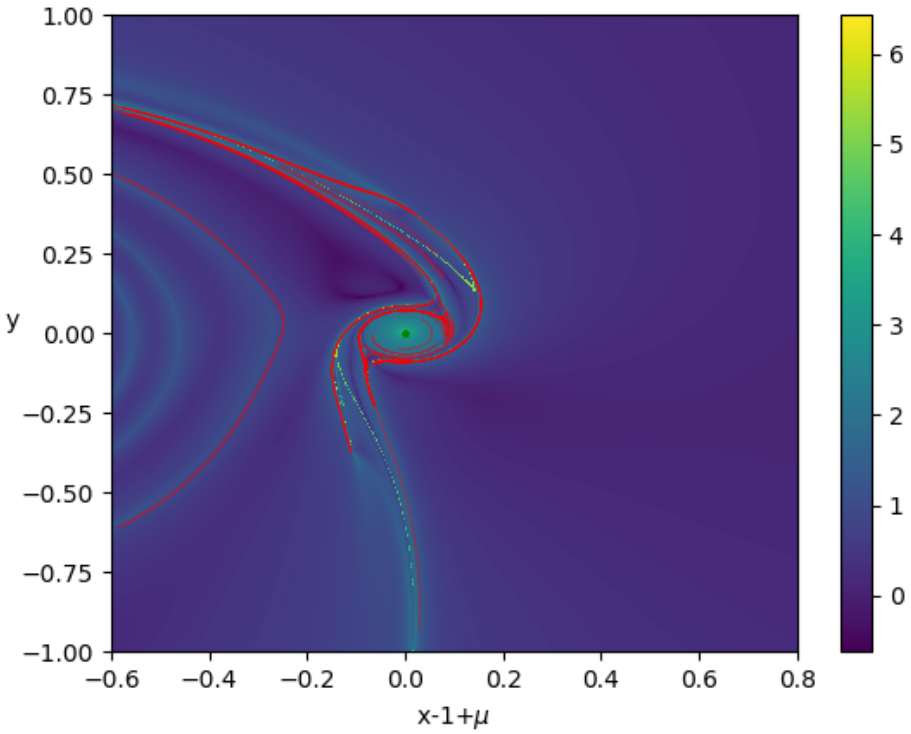

Figure 6.28: Variational theory LCS results (red) plotted on top of FTLE field

It can be seen that the regions that were expected to correspond to the WSB in the FTLE case, are exactly the same as the lines that are obtained from the variational theory. This indicates that the generated orbits would be the same as Figure 6.23, and no further orbits need to be generated to verify that the repelling LCS from the variational theory are in fact the WSB. Also note that the results from the variational theory trace the outer edge of the FTLE field results, which were intuitively expected to correspond to the WSB. This is a strong result, as it indicates that the variational theory is more robust than the FTLE method.

It can be concluded that while the FTLE field computation is faster than the variational theory (3 hours versus 20 hours), the results from the variational theory are more robust. It is shown that the results are not perfect (i.e: false positives still exist) but in future work this could be combated by making use of interpolation to further refine LCS extraction, or by lowering tolerances used in integrating the ODE's.

7 | Conclusions & Recommendations

7.1 Conclusions

In the beginning of this literature study the following main research questions for the thesis were proposed:

- Without using a priori knowledge of the WSB, do LCS in the 2D search space around a planet yield WSB?
- How does the Weak Stability Boundary react to a change in integration time, corresponding to the time needed for a particle according to the stability criterion?
- How do the computed LCS for the system relate to WSB corresponding to stable points defined for different number of revolutions n?
- Can the application of LCS to the computation of Weak Stability Boundaries yield more efficient computation compared to the traditional method of stable set manipulation?

Without using a priori knowledge of the WSB, do LCS in the 2D search space around a planet yield WSB?
Two algorithms for finding LCS in the 2D search space around a planet were developed. The first of these, making use of the Finite Time Lyapunov Exponent theory, was validated using the Double Gyre example often used in LCS literature. After a succesful match with the literature, the algorithm was applied to the Sun-Mars system within the framework of the ERTBP. It was shown that the resulting FTLE field proves to yield a strong match with the 1-stable set $\mathcal{W}_1$. In particular, the general shape of the stable set is preserved to a great degree. It was also found that this matching improves as the value of the integration time f_{final} is increased. While the shape of the resulting field matches well with $\mathcal{W}_1$, it was also shown that details present in $\mathcal{W}_1$ are not captured quite as well.
The second algorithm that was developed is based on the variational theory. Compared to the FTLE algorithm, it contains much more parameter tuning and numerical approximations than the FTLE algorithm. It was found that including a natural stopping condition in the integration

of strainlines gives rise to better results than the state-of-the-art results from [18]. Furthermore, it was found that interpolation on strainlines to give more accurate results of average λ_2 values on strainlines is not required, as computational time for this procedure becomes a major constraint. Strainlines around the planet were computed, and it was shown that filtering these strainlines to LCS removes the vast majority of strainlines not corresponding to the stable set. it was found that, when one uses sufficiently large values of f_{final}, the resulting LCS without using a priori knowledge of the WSB, are able to trace the boundary of $\mathcal{W}_1$.
Finally, it can be concluded that LCS can be used to get an idea of the WSB around the planet. In particular, the FTLE method shows to be a very efficient, low-cost method for getting initial results. While the method based on variational theory give good results without a-priori usage of the stable set, the computation takes considerably longer and more critical parameter tuning for numerical approximations needs to be done.

How does the Weak Stability Boundary react to a change in integration time, corresponding to the time needed for a particle according to the stability criterion?
It was found that the time needed for the particle according to the stability criterion is often unknown, and an assumption was made that the particle follows close to a Kepler trajectory. Using the period of the osculating ellipse (T) with the initial location of the particle as periapse, the integration time was defined. It was found that using the value T for the integration time does not yield a match with the WSB. However, increasing this value to $2T$ and $3T$ provided better results. This is in line with the results that were found by increasing the integration time for the full system as a whole, where larger integration times gave rise to better matches.
It was concluded that constant integration times for the full system are a better choice than local variations. While regions far away from the planet naturally give rise to larger values of T (and differences with large, constant values are negligible), regions close to P_2 will yield integration times that are too small. This goes against the general principle of wanting large values in general, and thus gives inaccurate results in the region close to P_2.

How do the computed LCS for the system relate to WSB corresponding to stable points defined for different number of revolutions n
It was found that for $\mathcal{W}_2 \ldots \mathcal{W}_6$ the matching was better than for $\mathcal{W}_1$. This was the case because the edge of $\mathcal{W}_1$ is longer than $\mathcal{W}_2$, and the repelling LCS seems to stop where the edge of $\mathcal{W}_2$ stops. For the problem at hand, it was shown that sets $\mathcal{W}_2 \ldots \mathcal{W}_6$ are very similar. The fact that matching with $\mathcal{W}_2$ was better, may be attributed to the fact that LCS form an average result for all $\mathcal{W}_n$, and for this particular problem $\mathcal{W}_2$ provides a closer approximation to that average than $\mathcal{W}_1$.

Can the application of LCS to the computation of Weak Stability Boundaries yield more efficient computation compared to the traditional method of stable set manipulation?

In this work it is shown that for both algorithms making use of parallel processing is vital. The problem is inherently parallelizable, and should be exploited as such. It is shown that using the FTLE field as an approximation for the stable sets is computationally efficient. The variational theory algorithm is much less computationally efficient than the FTLE algorithm, particularly when interpolations are done. The software is written in a way to maximize efficiency, by storing partial results that can be reused later. This improves the competitiveness of the method, but in terms of efficiency it still falls behind the FTLE algorithm.

7.2 Recommendations

While this work has shown that LCS can be found around the planet in an efficient way, and trace the WSB to a certain degree, a number of recommendations are given to further extend the body of knowledge on this topic:

- It was shown that since the process of computing strainlines is a numerically sensitive process, in some cases strainline integration is terminated too quickly. It was also shown that this can be countered by including a sufficient amount of initial conditions close to each other. When no a priori knowledge of the WSB is used, the only way to combat this numerical problem is to initialize a sufficiently fine grid. Because a large area of the space around P_2 does not yield any LCS, using a fine grid for the full space is inefficient.
  It is recommended that an iterative process for generating LCS is developed. In this method, the full procedure for finding LCS using a relatively coarse grid is employed. When LCS are extracted using this coarse grid, it is recommended to re-run the procedure using initial conditions around the obtained LCS as the new grid. The resulting LCS can then be stacked on top of the previous LCS, thus effectively having created a finer grid around the promising regions. It is expected that this might allow more details of the $\mathscr{W}_n$ sets to be captured by the LCS, rather than just the boundary.

- For this thesis, values of f_0 have been fixed as f_{final} has been varied. It it interesting to study how the found LCS (for both FTLE and Variational theory) change as this window of time (using a fixed Δf) is varied. Changes in LCS might indicate specific times when certain regions around the planet are more easily accessible and aid in trajectory design.

- In this work some analysis has been done on making use of an interpolation factor $\mathscr{F}$ to further strengthen the filter from strainlines to LCS. One of the parameters, namely the neighbour definition δ has not been study to that degree. It was found in some experiments that using a too small value of δ causes neighbours to no longer be seen as the local regime. Rather, any results on LCS filters are just the result of numerical noise. Using too large values for δ is also undersirable, as neighbouring strainlines would no longer be considered to

be in the local regime. It would be interesting to see how this parameter affects the final LCS extraction for the ERTBP.

Appendix A: Variational Equations Double Gyre

If this work is reproduced, use will be made of the variational equations. This appendix contains the Python code for the variational equations of the Double Gyre.

```
from math import *
import numpy as np

def doubleGyreVar(t,x):
    w = 2*pi/10
    A = 0.1
    eps = 0.1

    wt = w*t
    swt = sin(wt)
    a = eps*swt
    b = 1-(2*a)
    f = a*x[0]**2 + b*x[0]
    spx = sin(pi*f)
    cpx = cos(pi*f)
    spy = sin(pi*x[1])
    cpy = cos(pi*x[1])
    df = 2*a*x[0] + b
    d2f = 2*a

    AA = -pi*cpx*df*cpy
    B  =  pi*spx*spy
    C  =  spy*(-spx*(df**2)*pi+cpx*d2f)
    D  =  pi*cpx*df*cpy

    dx = pi*A*np.array([-spx*cpy ,
                        cpx*spy*df,
                        AA*x[2]+B*x[3],
                        C*x[2]+D*x[3],
                        AA*x[4]+B*x[5],
                        C*x[4]+D*x[5]])
    return dx
```

Appendix B: Variational Equations and Mappings ERTBP

In this appendix the Python code for the variational equations, coordinate mappings, inverse coordinate mappings, and Jacobians of coordinate mappings is given. These are used to define the ERTBP when executing both the FTLE and Variational Theory LCS extraction algorithms.

```
def M(r, ep, e, f0, mu):
    r2 = r[0]
    theta2 = r[1]

    r2prime = (r[0]*ep*np.sin(f0))/(1+ep*np.cos(f0))
    theta2prime = np.sqrt( ((mu*(1+e))/(r[0]**3*(1+ep*np.cos(f0)))) - 1
    return([r2, theta2, r2prime, theta2prime])

def P2C(r, mu):
    x2 = 1-mu + r[0] * np.cos(r[1])
    y2 = r[0] * np.sin(r[1])
    x2prime = r[2]*np.cos(r[1]) - r[0]*r[3]*np.sin(r[1])
    y2prime = r[2]*np.sin(r[1]) + r[0]*r[3]*np.cos(r[1])
    return([x2,y2,x2prime,y2prime])

def Minv(r):
    return([r[0],r[1]])

def C2P(x,mu):
    oldX = x[0]
    x[0] = x[0]-(1-mu)
    r = np.sqrt(x[0]**2+x[1]**2)
    theta = np.arctan2(x[1],x[0]) + 2*pi
    rdot = x[2]*np.cos(x[1]) + x[3]*np.sin(x[1])
    thetadot = (-1*x[2]*np.sin(x[1]) + x[3]*np.cos(x[1]))/r

    x[0] = oldX
    return([r, theta, rdot, thetadot])


def ERTBPvar(f, x, ep, mu):
    xx = x[0]
    yy = x[1]
    vx = x[2]
    vy = x[3]
```

```
    fr = 1 / (1+ep*np.cos(f))
    r1 = np.sqrt( (xx+mu)**2 + yy**2 )
    r2 = np.sqrt( (xx+mu-1)**2 + yy**2 )

    doxdx = fr * (1-(1-mu)*(1/r1**3 + (xx+mu) * (-3/r1**5) *
    (xx+mu) ) - mu*((1/r2**3) + ((xx+mu-1)*(-3/r2**5)*(xx+mu-1))))

    doydy = fr * (1-(1-mu)*(1/r1**3 + yy * (-3/r1**5) * yy) - mu*((1/r2**3) +
    (yy *(-3/r2**5)*yy)))

    doydx = fr * (-1*(1-mu)*yy*(-3/r1**5)*(xx+mu) - mu*yy*(-3/r2**5)*(xx+mu-1))
    doxdy = fr * (-1*(1-mu)*(xx+mu)*(-3/r1**5)*yy - mu*(xx+mu-1)*(-3/r2**5)*yy)

    dx = [vx,
        vy,
        2*vy + fr * (xx - (1-mu)*(xx+mu)* 1/(r1**3) - mu * (xx+mu-1) * 1/(r2**3) ),
        -2*vx + fr * (yy - (1-mu)* yy * 1/(r1**3) - mu * yy * 1/(r2**3)),
        x[6],
        x[7],
        x[4]*doxdx + x[5]*doxdy + 2*x[7],
        x[4]*doydx + x[5]*doydy - 2*x[6],
        x[10],
        x[11],
        x[8]*doxdx + x[9]*doxdy + 2*x[11],
        x[8]*doydx + x[9]*doydy - 2*x[10],
        x[14],
        x[15],
        x[12]*doxdx + x[13]*doxdy + 2*x[15],
        x[12]*doydx + x[13]*doydy - 2*x[14],
        x[18],
        x[19],
        x[16]*doxdx + x[17]*doxdy + 2*x[19],
        x[16]*doydx + x[17]*doydy - 2*x[18],
        ]
    return(dx)

def JacMinv(r):
    return([[1,0,0,0],
            [0,1,0,0]])


def jacP2C(rr):
    r0 = rr[0]
    th0 = rr[1]
    rd0 = rr[2]
    thd0 = rr[3]
    return([[cos(th0), -1*r0*sin(th0), 0, 0],
           [sin(th0), r0*cos(th0), 0, 0    ],
           [-1*thd0*sin(th0), -rd0*sin(th0)-r0*thd0*cos(th0), cos(th0), -r0*sin(th0)],
           [thd0 * cos(th0), rd0*cos(th0)-r0*thd0*sin(th0), sin(th0), r0*cos(th0)]])


def jacC2P(rrr):
    x = rrr[0]-(1-mu)
    y = rrr[1]
    xd = rrr[2]
```

```
    yd = rrr[3]
    r = np.sqrt(x**2+y**2)
    return([[x/r, y/r, 0, 0       ],
            [-y/r**2, x/r**2, 0, 0],
            [(r*xd - (x*xd + y*yd) * x/r)/r**2 , (r*yd - (x*xd + y*yd)*y/r)/r**2,
            x/r, y/r],
            [(r**2 * yd - (x*yd - xd*y)*2*x)/r**4 , (r**2*(-1*xd) -
            (x*yd - xd*y) * 2*y)/r**4, -1*y/r**2, x/r**2 ]])


def jacM(r,ep, f0, e, mu):
    A = np.sqrt((mu*(1+e)) / (1+ep*cos(f0)))
    return([[1, 0],
            [0, 1],
            [(ep*sin(f0)) / (1+ep*cos(f0)) , 0],
            [-3/2 * A * r[0]**(-5/2), 0]])
```

Bibliography

[1] E. Belbruno. *Capture Dynamics and Chaotic Motions in Celestial Mechanics*. Princeton University Press, 2004.

[2] E. Belbruno. *Fly me to the moon: an insider's guide to the new science of space travel*. Princeton University Press, 2007.

[3] Edward A Belbruno and James K Miller. Sun-perturbed earth-to-moon transfers with ballistic capture. *Journal of Guidance, Control, and Dynamics*, 16(4):770–775, 1993.

[4] C. Circi and P. Teofilatto. Effect of planetary eccentricity on ballistic capture in the solar system. *Celestial Mechanics and Dynamical Astronomy*, 2005. doi: 10.1007/s10569-005-3640-9.

[5] P.J. Davis and P. Rabinowitz. *Methods of Numerical Integration*. Elsevier, 1984.

[6] M. Gidea E. Bebruno, F. Topputo. Resonance transitions associated to weak capture in the restricted three-body problem. *Advances in Space Research*, 2008. doi: 10.1016/j.asr.2008.01.018.

[7] M. Farazmand and G. Haller. Computing lagrangian coherent structures from their variational theory. *Chaos: An Interdisciplinary Journal of Nonlinear Science*, 22, 2012. doi: 10.1063/1.3690153.

[8] F. García and G. Gómez. A note on weak stability boundaries. *Celestial Mechanics and Dynamical Astronomy*, 2007. doi: 10.1007/s10569-006-9053-6.

[9] G. Haller. A variational theory of hyperbolic lagrangian coherent structures. *Physica D*, 2011. doi: 10.1016/j.physd.2010.11.010.

[10] G. Haller and G. Yuan. Lagrangian coherent structures and mixing in two-dimensional turbulence. *Physica D*, 2000. doi: 10.1016/S0167-2789(00)00142-1.

[11] N. Hyeraci and F. Topputo. Method to design ballistic capture in the elliptic restricted three-body problem. *Journal of Guidance, Control, and Dynamics*, 33(6), 2010. doi: 10.2514/1.49263.

[12] N. Hyeraci and F. Topputo. The role of true anomaly in ballistic capture. *Celestial Mechanics and Dynamical Astronomy*, 2013. doi: 10.1007/s10569-013-9481-z.

[13] D. Kelley, M. Allshouse, and N. Ouellette. Lagrangian coherent structures separate dynamically distinct regions in fluid flows. *Physical Review*, 88(1), 2013. doi: 10.1103/PhysRevE.88.013017.

[14] E Lega, M Guzzo, and Cl Froeschlé. Detection of close encounters and resonances in three-body problems through levi-civita regularization. *Monthly Notices of the Royal Astronomical Society*, 418(1):107–113, 2011.

[15] M. Schub M.W. Hirsch, C.C. Pugh. *Invariant Manifolds*. 2016.

[16] A.S. Parkash. *Literature Review: Application of Lagrangian Coherent Structures to Ballistic Capture Trajectories*. Delft University of Technology, 2018.

[17] Linda Petzold. Automatic selection of methods for solving stiff and nonstiff systems of ordinary differential equations. *SIAM journal on scientific and statistical computing*, 4(1):136–148, 1983.

[18] X. Ros Roca. *Computation of Lagrangian Coherent Structures with Application to Weak Stability Boundaries*. Dipartamento di Scienze e Tecnologie Aerospaziali, Politecnico di Milano, 2015.

[19] D. Romagnoli and C. Circi. Earth–moon weak stability boundaries in the restricted three and four body problem. *Celestial Mechanics and Dynamical Astronomy*, 2009. doi: 10.1007/s10569-008-9169-y.

[20] Shawn C Shadden, Francois Lekien, and Jerrold E Marsden. Definition and properties of lagrangian coherent structures from finite-time lyapunov exponents in two-dimensional aperiodic flows. *Physica D: Nonlinear Phenomena*, 212(3-4):271–304, 2005. doi: 10.1.1.120.439.

[21] P. Sousa Silva and M. Terra. Applicability and dynamical characterization of the associated sets of the algorithmic weak stability boundary in the lunar sphere of influence. *Celestial Mechanics and Dynamical Astronomy*, 2012. doi: 10.1007/s10569-012-9418-y.

[22] V. Szehebely. *Theory of Orbits: The Restricted Problem of Three Bodies*. Academic Press Inc, New York, 1967.

[23] F. Topputo. On optimal two-impulse earth–moon transfers in a four-body model. *Celestial Mechanics and Dynamical Astronomy*, 2014. doi: 10.1007/s10569-013-9513-8.

[24] F. Topputo and E. Belbruno. Computation of weak stability boundaries: Sun–Jupiter system. *Celestial Mechanics and Dynamical Astronomy*, 2009. doi: 10.1007/s10569-009-9222-5.

[25] F. Topputo and E. Belbruno. Earth–Mars transfers with ballistic capture. *Celestial Mechanics and Dynamical Astronomy*, 2015. doi: 10.1007/s10569-015-9605-8.

[26] James R. Wertz. *Mission Geometry: Orbit and Constellation Design and Management*. Microcosm Press, Springer, 2009.

[27] Z.-F.Luo and F.Topputo. Analysis of ballistic capture in sun–planet models. *Advances in Space Research*, 2015. doi: 10.1016/j.asr.2015.05.042.

[28] Z.-F.Luo, F.Topputo, F.Bernelli-Zazzera, and G.-J.Tang. Constructing ballistic capture orbits in the real solar system model. *Celestial Mechanics and Dynamical Astronomy*, 2014. doi: 10.1007/s10569-014-9580-5.